Fluid-Driven Fractures in Elastic Hydrogels: Propagation and Coalescence

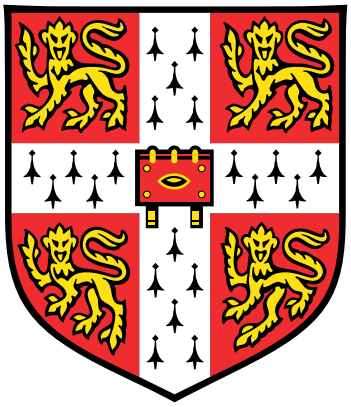

Niall John O'Keeffe

Department of Applied Mathematics and Theoretical Physics
University of Cambridge

This dissertation is submitted for the degree of
Doctor of Philosophy

Downing College May 2018

To David Gavin (1991-2017)

Declaration

I hereby declare that except where specific reference is made to the work of others, the contents of this dissertation are original and have not been submitted in whole or in part for consideration for any other degree or qualification in this, or any other university. This dissertation is my own work and contains nothing which is the outcome of work done in collaboration with others, except as specified in the text and Acknowledgements.

Niall John O'Keeffe
May 2018

Acknowledgements

First and foremost, I would like to thank my supervisor, Paul Linden, for giving me the opportunity to undertake a PhD in such great surroundings. He has always been encouraging and approachable, providing help whenever it was needed.

My work in the GKB Laboratory would not have been possible without the work of the technicians. David, Colin, Paul, Andy and John have all been exceptionally helpful in constructing any piece of equipment I have needed. In particular, I would like to thank David Page-Croft who interpreted my many vague descriptions, coming up with better solutions than I thought possible and dealt with frequent shopping lists. I would also like to thank Jamie Partridge who has always been very generous with his time in helping me learn the ins and outs of working in the lab, and imparting some of his extensive Digiflow knowledge to me.

For their many helpful insights and discussions on the coplanar fracture problem I would like to thank Zhong Zheng and Herbert Huppert, as well as the Scherman Lab in Chemistry for their help in choosing a suitable hydrogel.

To all the PhD students throughout my time here, particularly my office-mates Adrien and JP, thank you for the scientific and non-scientific discussions, for your friendship and the many great events that were held. You definitely made DAMTP an enjoyable and exciting place to work.

I would also like to thank my friends back home in Galway for their frequent messages and making sure there is always plenty of craic and not just cracks in my life.

A very special thank you to Nicole, for putting up with me, and who has made the past three and a half years some of the best of my life. Thanks also for proof-reading this entire thesis and listening to all my ramblings.

Finally, I would like to thank my family: my parents, John and Patricia, and my sisters, Hannah and Ciara. They have always supported me in every endeavour and have provided me with every opportunity throughout my life. I am very grateful for everything they have done for me.

Abstract

In this thesis we focus on a novel experimental exploration of fluid-driven fractures in a brittle hydrogel matrix. Fluid-driven fracturing is a procedure by which a fracture is initiated and propagates due to pressure applied by a fluid introduced inside the fracture.

We describe how to construct the experimental setup utilised in this research, including how to synthesize polyacrylamide hydrogels to study the processes linked with fluid-driven fracturing. These transparent, linearly elastic and brittle gels permit fracturing at low pressures and speeds allowing accurate measurements to be obtained. The broad range of modulus and fracture energy values attainable from this medium allow the exploration of particular regimes of importance. Fracturing within these hydrogels also creates beautiful spiral patterns on the plastically deformed surfaces. We analyse these patterns and discuss their formation, while also commenting on their fractal-like nature.

Initially, we study single fractures that are driven by an incompressible Newtonian fluid, injected at a constant rate into an elastic matrix. The injected fluid creates a radial fracture that propagates along a plane. We investigate this type of fracture theoretically and then verify the scaling predictions experimentally. We examine the rate of radial crack growth, fracture aperture, shape of the crack tip and internal fluid flow field. We exhibit the existence of two distinct fracturing regimes, and the transition between these, in which propagation is either dominated by viscous flow within the fracture or the material toughness. Particle image velocimetry measurements also strikingly show that the flow in the fracture can alter from an expected radial symmetry to circulation cells, dependent on the regime of propagation.

We then expand our research to the problem of two coplanar fluid-driven radial fractures. This was chosen to focus on the physical mechanisms that are key to fracture network formation, related to many geophysical and industrial practices. Initially, the two fractures propagate independently of each other. At a critical separation they begin to interact, with non-uniform growth occurring along the fracture edges due to

the evolving stress state in the gel matrix. When the radial extents of the fractures become sufficiently large, they coalesce and form a bridge between them. Following initial contact, a large increase in flow is seen into the newly created bridge and most of the growth is localised along this, perpendicular to the line connecting the injection sources. From experimental measurements, we observe a universal dynamic behaviour for the growth of this bridge. We model this universal behaviour theoretically and construct scalings related to the growth after coalescence, which again identifies both a viscous and toughness regime. The toughness regime is verified experimentally for the bridge growth and the universal shape of the thickness profile along the bridge. The coalesced fractures then transition into a single fracture at late times. Finally, we discuss a number of other interesting scenarios that may occur such as, non-coalescing fractures, asymmetric coalescence and ridge formation.

Table of contents

List of figures

List of tables

Chapter 1

Introduction

1.1 Motivation

A fluid-driven or hydraulic fracture is a tensile fracture that is initiated and propagates due to pressure of a fluid introduced inside a solid medium. This type of fracture is observed widely in both natural and industrial geophysical processes.

The technique of hydraulic fracturing is mainly used as a well stimulation technique in unconventional reservoirs, which have relatively low permeability and porosity, making it difficult to extract oil and gas (Economides & Nolte, 2000). These reservoirs are typically found in shale formations formed from deposits of mud, silt, clay and organic matter, deep in the Earth's crust (1-4 km). Unlike conventional reservoirs, where a vertical well is drilled to extract an oil or gas pocket, unconventional reservoirs involve drilling a horizontal wellbore into the stratum (Fig. 1.1). After the well is drilled, explosives are transported to the horizontal section and used to create perforations at spaced intervals. Fluid comprising typically of 99.5% water and sand, and 0.5% chemicals, including acid, friction reducers and corrosion inhibitors, is then injected at high pressure into the wellbore to create fractures at the perforations. The creation of fractures increases the surface area connected to the wellbore, allowing increased amounts of trapped hydrocarbons to be released. Once injection is stopped, the pressure is released and closure of the fractures takes place due to the overburden stress from the weight of the strata. The sand particles, known as proppants, are included to 'prop' open the fractures after injection so that hydrocarbons may continue to flow to the wellbore. Relaxation of the fractures also causes some fracturing fluid to be returned to the surface, which must be chemically treated due to its toxicity. Hydraulic fracturing operations have generated an intense environmental debate due to concerns

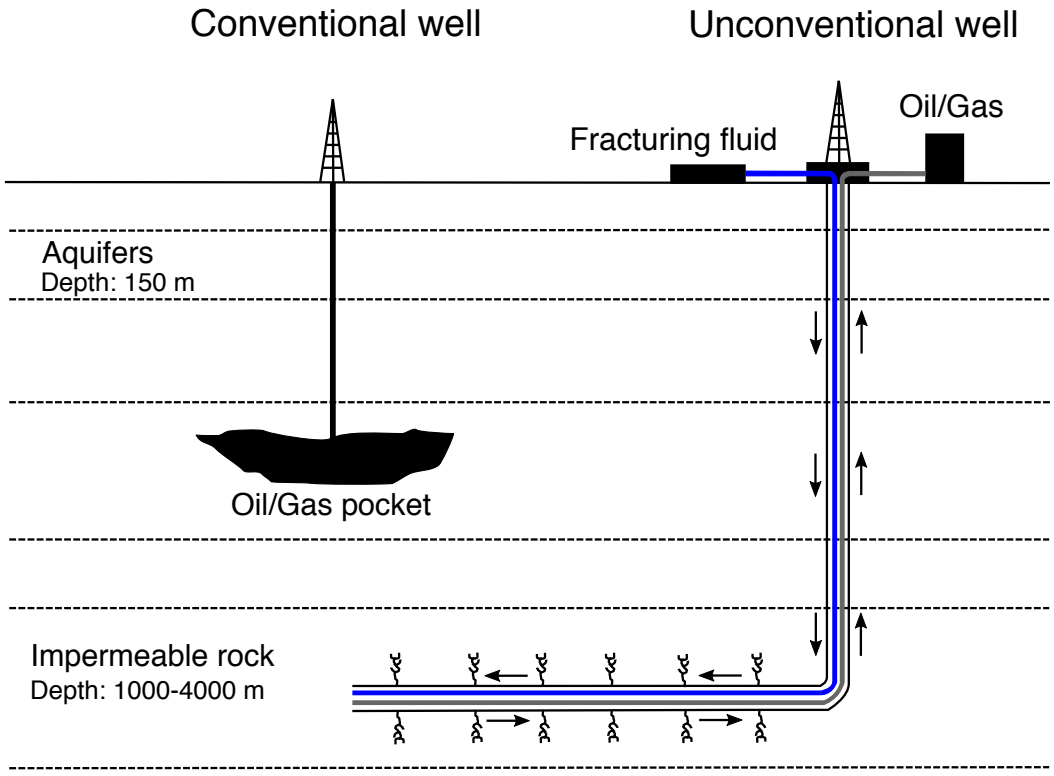

FIGURE 1.1: Schematic of a standard hydraulic fracturing operation extracting unconventional hydrocarbons trapped in a low permeability formation.

about induced seismicity, potential gas leakages, contamination of freshwater aquifers and disposal of waste water (Mair *et al.*, 2012).

The fluid injection process can normally be divided into separate stages. Initially, low viscosity fluid is injected to initiate propagation and reduce well friction. High density polymers and crosslinkers are then added to increase the viscosity of the fracturing fluid by up to 3 orders of magnitude once propagation is established. This causes a filter cake (insoluble material from polymers) to build up on the fracture surfaces that reduce fluid loss into the stratum. A slurry containing proppants is then injected. Finally, cleaning agents are added to break down the polymers. In order to maximise efficiency, the aim of an operation is to maximise fracture surface area and minimise injected fluid volume. Moreover, the fractures must be sufficiently wide so that proppants can be transported throughout the fracture network.

Apart from hydrocarbon extraction, other industrial applications of hydraulic fracturing include:

- **Measurement of existing (*in-situ*) stresses**: Stresses are estimated by measuring breakdown and shut-in pressures of a hydraulic fracturing treatment and

relating these to some components of the local stress tensor (Haimson & Fairhurst, 1969; Rutqvist *et al.*, 2000).

- **Carbon sequestration**: Supercritical CO_2 is injected into porous formations such as old oil reservoirs or saline aquifers with a low permeability cap rock (Huppert & Neufeld, 2014; Rudnicki, 2000). In this situation, fluid-driven fracturing of the cap rock must be mitigated to ensure reservoir integrity and prevent CO_2 leakage.

- **Geothermal energy reservoirs**: A well is drilled to a depth (3-10 km) where the rock temperature is sufficiently high (≈ 200 °C). Hydraulic fracturing is then used to create the necessary permeability and a second well is drilled to intersect the newly fractured region. Cold water is injected down the first well and hot water is then returned to the surface at the second well where the thermal energy is converted to electricity. Vapourisation is mitigated by maintaining a high circulating fluid pressure (Legarth *et al.*, 2005; Murphy *et al.*, 1981).

- **Compensation grouting**: During tunnelling in soft ground, compensation grouting can be used to control ground and building movements. Grout, consisting of water, cement and sand, is injected between the tunnel and the foundations to compensate for ground loss and stress relief. This technique was used to control the tilt of the Big Ben clock tower in Westminster during construction of the Jubilee Line Extension Project (Au *et al.*, 2003; Harris *et al.*, 1999; Mair & Hight, 1994).

Additionally, hydraulic fracturing is observed in many natural settings, including:

- **Magma transport**: Fluid-driven fractures are encountered when studying the formation of sills, dykes and laccoliths (Kavanagh *et al.*, 2018; Lister & Kerr, 1991). In this case, the mechanism for crack propagation of magma-driven dykes is the pressure caused by density differences between the fluid and the surrounding rock formation.

- **Cells and tissues**: Large amounts of fluid are trapped in hydrogels within bodies. Poroelastic pressure on cells causes flows that can fracture biological barriers such as the nuclear envelope, cellular cortex, and epithelial layers (Arroyo & Trepat, 2017; Casares *et al.*, 2015; Lucantonio *et al.*, 2015).

- **Glaciers**: Fluid-driven fracture propagation can occur at glacier beds. Once a supraglacial lake, formed from meltwater, is connected to a basal crack underneath

a glacier, rapid turbulent flow induces fracturing. This results in a speedy drainage of the lake and can accelerate the movement of the glacier (Christoffersen *et al.*, 2018; Tsai & Rice, 2010).

1.2 Fluid-driven fractures

Hydraulic fracturing in its most simple form, a single crack, is still very complicated to model, because it involves the coupling of at least three processes: (i) mechanical deformation of the solid by fluid pressure; (ii) fluid flow in the fracture; and (iii) fracture propagation (Detournay, 2016). These processes are usually modelled by: (i) the theory of linear elasticity; (ii) lubrication theory; and (iii) linear elastic fracture mechanics (LEFM), respectively. Linear elasticity produces a non-local integral relationship between fracture width and pressure. Lubrication theory relates fluid flow with fracture width and pressure through a nonlinear partial differential equation. Finally, LEFM provides a propagation criterion related to the material toughness and stress state caused by internal pressure of the fracture. Thus, the full formulation of the problem is represented by a set of nonlinear integro-differential equations with a moving boundary and a singularity at the fracture tip. This is a very complex system and in order to make significant progress, three idealised fracture geometries have been extensively used (Fig. 1.2): (i) the Khristianovic-Geertsma-de Klerk (KGD) geometry is height independent and plane strain assumptions hold on the horizontal sections (Geertsma & De Klerk, 1969; Khristianovic & Zheltov, 1955); (ii) the Perkins-Kern-Nordgren (PKN) geometry applies to elongated fractures of constant height and elliptical vertical cross-section (Nordgren, 1972; Perkins & Kern, 1961); and (iii) the radial or 'penny-shaped' fracture geometry applies to homogeneous formation conditions, where the injection region is modelled as a point source. This occurs when the wellbore from which fluid is injected is orientated perpendicular to the direction of maximum confining stress, or when fluid is injected radially into a medium that can be considered homogeneous and infinite, in comparison to the size of the fracture.

The KGD and PKN geometries are used to model fractures for which the height is larger than the length and the length is larger than the height, respectively. These geometries can provide accurate estimates for fracture extents, provided the height of a fracture can be reasonably estimated in a given situation. However, in the penny-shaped fracture geometry all dimensions are time-dependent and can be determined from the mathematical model.

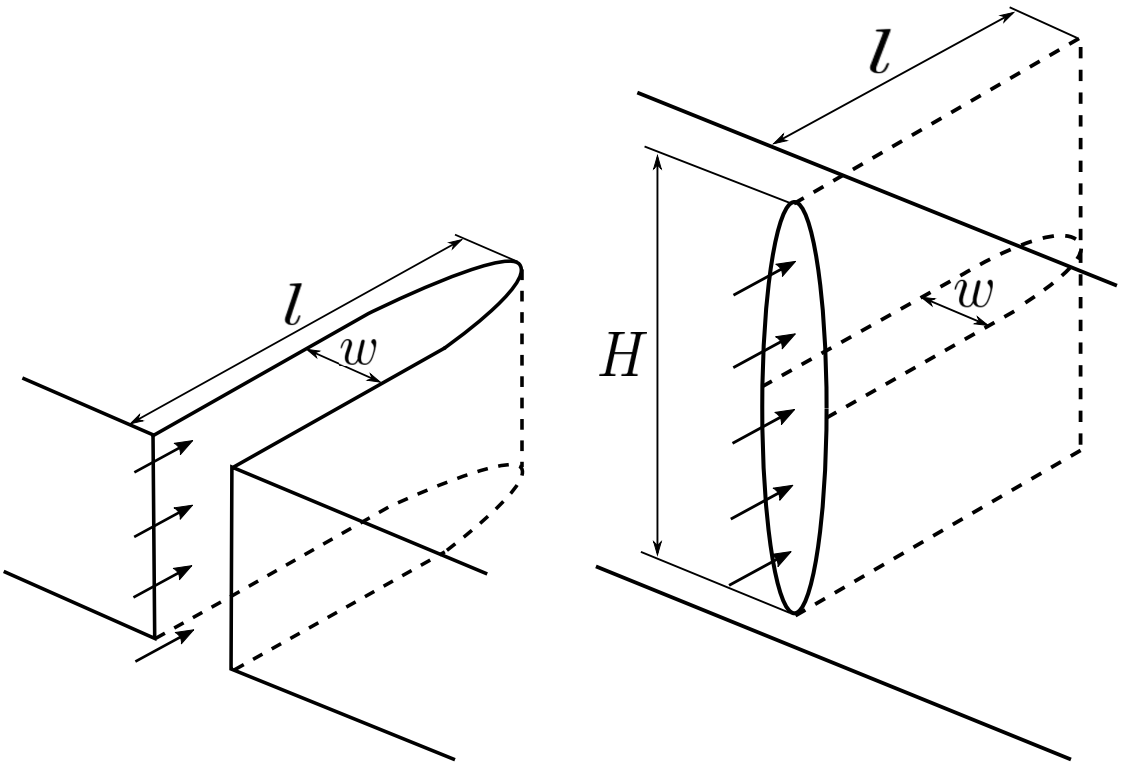

(a) KGD

(b) PKN

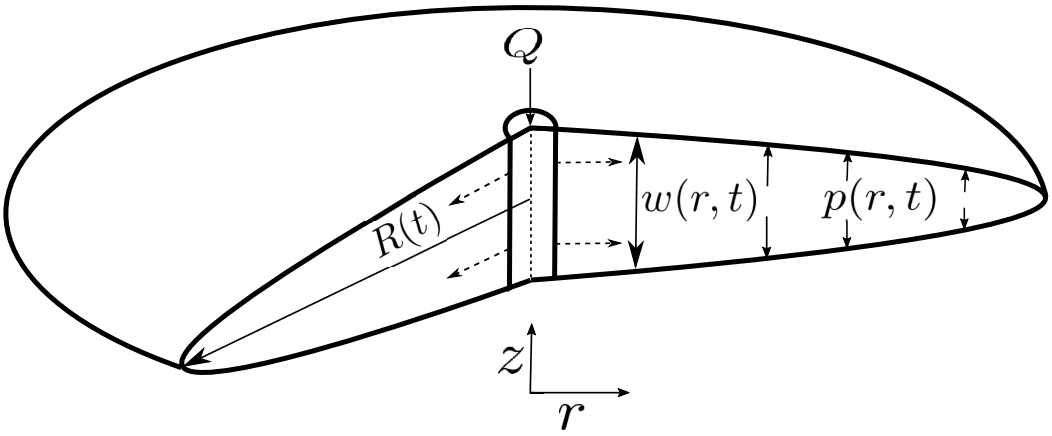

(c) Radial ('penny-shaped')

FIGURE 1.2: Schematic diagram of fracture geometries. (a) l and w denote the fracture length and aperture, respectively. (b) l, w and H denote the fracture length, aperture and height, respectively. (c) R, w and p denote the fracture radius, aperture and pressure, respectively, while Q represents the volumetric injection rate of fluid.

Initially, Barenblatt (1962) first applied fracture mechanics methods to the fluid-driven problem, where cohesion of the material was neglected to determine crack sizes and the existence of a fluid-lag, a gap between the fluid front and the crack front, was identified. In particular, the radially symmetric penny-shaped crack problem has been studied extensively since Sneddon (1946), where the stress distribution around a fracture was determined. The original fracture tip asymptote used in many studies was obtained from LEFM, which corresponds to a toughness-dominated regime (Rice, 1968). Spence & Sharp (1985) developed a theory for hydraulic fractures in an infinite medium assuming viscous dissipation within the fluid was the dominant mechanism for energy dissipation. This established a viscous-dissipation asymptote.

Since then, Garagash, Detournay and others have focused on the crack tip region (Garagash *et al.*, 2011; Garagash & Detournay, 2000). They have also showed that two dissipative processes, fracturing of the rock (toughness) and viscous flow in the fracture, along with two fluid balance mechanisms, leak-off and storage of fracturing fluid in the fracture, significantly affect the fracture propagation behaviour (Detournay, 2016; Detournay & Garagash, 2003; Savitski & Detournay, 2002).

Numerical simulations of hydraulic fractures is another area of extensive research that we will not focus on here, involving many different approaches such as finite difference, finite element and phase-field methods (Adachi *et al.*, 2007; Gordeliy & Peirce, 2013; Mikelić *et al.*, 2015). However, these computations can be very expensive due to the complex nature of the non-local and nonlinear governing equations with a singularity at the crack tip. Extensive use is made of asymptotic solutions, dependent on the energy dissipation and flow balance mechanisms, as moving boundary conditions. These studies have addressed many industrial specific scenarios, such as the interaction between fractures spaced along the wellbore and the effect of the spacing on fracture orientation (Lecampion & Desroches, 2015; Salimzadeh *et al.*, 2017).

Throughout the course of this research we will focus on the penny-shaped fracture geometry driven by an incompressible Newtonian fluid, injected at a constant rate into an isotropic impermeable gel matrix. We assume there is a negligible fluid lag, i.e. the fluid front coincides with the fracture front, which turns out to be a valid assumption from experimental measurements. This simple geometry is chosen primarily because it permits accurate experimental measurements and also displays the nonlinear physical mechanisms found in typical field hydraulic fractures.

First, we will use this to investigate the regimes of dynamic growth and previously unseen internal flow structure within the fractures as propagation occurs through a

hydrogel medium. This allows us to validate and highlight discrepancies associated with the long established existing theory. Subsequently, we will build upon this by exploring the interaction and coalescence or non-coalescence of two coplanar penny-shaped fractures. This type of interaction to our knowledge is undocumented and exhibits numerous interesting features including coalescence dynamics and fluid flow behaviour.

1.2.1 Experimental studies

Considering the difficulties involved using analytical and numerical techniques, an experimental approach is of vital importance for capturing and understanding the physical mechanisms involved, as well as verifying and improving theoretical models. Moreover, because of the extremely high pressures and stresses involved in hydraulic fracturing of rock, a suitable analogue is required to conduct experiments in a laboratory environment. Historically, experiments trying to capture fluid-driven fracture dynamics have involved materials such as gelatin and polymethyl methacrylate (PMMA). These have been widely used to model geological mechanics because they are transparent and exhibit elastic and brittle behaviour similar to that seen in rocks (Alpern *et al.*, 2012; Menand & Tait, 2002; Takada, 1990).

Hubbert & Willis (1957) first experimentally investigated the direction of hydraulically induced fractures due to the pre-existing stresses in a gelatin medium. A plaster-of-paris slurry was injected that solidified post-experiment so that the plane of fracture growth could be accurately identified. They verified that a fluid-driven fracture will form perpendicular to the direction of least principal stress. However, dynamic measurements of fracture extent and aperture were not undertaken in this study.

Numerous experimental studies involving gelatin have investigated dyke and sill formation involving buoyant fluid fractures (Kavanagh *et al.*, 2015, 2018, 2013, 2006; Menand *et al.*, 2010; Menand & Tait, 2002; Takada, 1990). These have mainly involved initiating fractures at the base of a soft, homogeneous or layered, gelatin reservoir by injecting fluid at a constant rate. Experiments have also been conducted in these studies where propagation is solely driven by the density differences between the fluid and gelatin.

To investigate the fracture tip behaviour of penny-shaped fluid-driven fractures, Bunger & Detournay (2008) developed an experiment to measure the aperture of a fluid region between two PMMA plates glued together with an adhesive. This validated

theoretical expectations for the crack tip region, when the dominant mechanism for energy dissipation was either toughness or viscous flow. Similar experiments by Bunger *et al.* (2005, 2013, 2004) examined the behaviour of near-surface fractures in a PMMA or borosilicate glass specimen, with an initial flaw at the end of the wellbore to ensure the fracture propagates in a particular direction. In these near-surface experiments it was observed that the fracture tips curve towards the free surface as the fracture grows due to the stress state in the elastic solid with the presence of a free surface. Lecampion *et al.* (2017) investigated the initiation and early stage growth of radial fractures from a notched wellbore in both PMMA and cement under compressive stresses. They found differences between initiation and breakdown (maximum) pressures due to viscous effects, and accounted for non-monotonic flux after initiation from wellbore pressurisation.

More recently, Lai *et al.* (2016, 2015) also investigated penny-shaped fractures using gelatin, which validated scaling laws of the time-dependence of crack growth and aperture in the viscous and toughness regimes in an impermeable medium. These experiments are similar to the work described in Chapter 5 in this thesis, however it was conducted concurrently with these studies and not inspired as a result of their work. Nonetheless, this provides an opportunity to compare results and describe in detail the similarities and differences. The experimental setups are quite similar apart from the medium and the results are in general agreement with each other within error bounds. This provides us with confidence regarding the results and highlights possible shortcomings of the existing theory.

In this thesis we will describe fluid-driven fracturing experiments in a polyacrylamide hydrogel. This is a gel widely used in biology as cell culture substrates. Additionally, it has been used to study the propagation of dry dynamic fractures and shown to fracture similarly to other brittle materials, such as PMMA and glass (Goldman *et al.*, 2012; Livne *et al.*, 2007, 2004, 2005). One advantage of using these hydrogels is that material toughness stays approximately constant with varying crack tip velocity for highly cross-linked gels (Tanaka *et al.*, 2000). In PMMA and gelatin toughness has been observed to vary with crack tip velocity, but this effect may be minimised by ensuring velocities are kept within a certain range (Baumberger *et al.*, 2006; Marshall *et al.*, 1974). Polyacrylamide gels are also completely transparent and may be treated as a linear elastic solid, which enables precise optical measurements and satisfies a main assumption of theoretical models (Storm *et al.*, 2005).

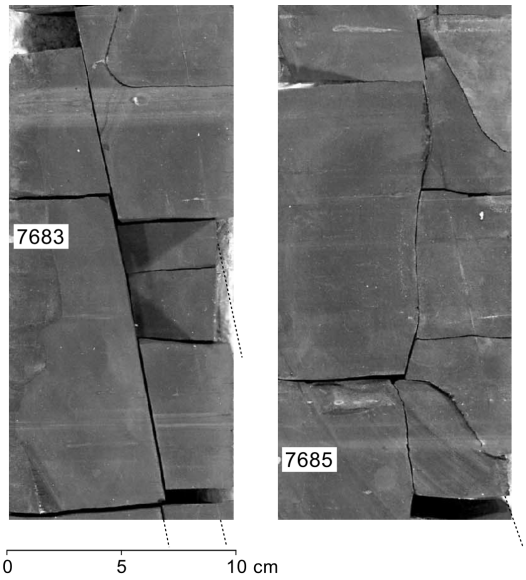

FIGURE 1.3: Natural fractures sealed with calcite in a Barnett shale (Gale *et al.*, 2007).

1.2.2 Fracture networks

In real-world scenarios involving fluid-driven fractures, it is expected that a fracture network will form due to branching of the fracture tip caused by local stress effects or heterogeneities present in the surrounding medium. In Chau *et al.* (2016) it is proposed that fractures within a hydraulic fracturing network generally form orthogonally to each other, similar to that observed in pre-existing natural fractures rather than a V-shaped branching structure (Gale *et al.*, 2014, 2007). This is explained by the fact that if a fracture is open and free of shear stresses, the only way for another fracture intersecting it to be free of shear stresses is to be inclined orthogonally to the original fracture in order to satisfy local equilibrium. Moreover, it is expected that fluid will follow any pre-existing natural fractures wherever possible due to the reduced fracture energy along these joints. An example of some natural fractures found in a Barnett shale drilling core is shown in Fig. 1.3.

The complex configuration of a fracture network means that when fluid-driven fracturing takes place, multiple fractures may interact with one another, altering their behaviour of growth and orientation. In this thesis we will describe simple experiments involving two penny-shaped fractures in an attempt to understand the physical mechanisms involved when fractures interact and, possibly, coalesce or overlap.

1.3 Thesis structure and objectives

We are interested in the experimental and theoretical exploration of fluid-driven fracturing processes, such as propagation and coalescence. This involves the construction of a novel experimental setup containing wellbores set in a transparent elastic and brittle hydrogel. We investigate three main areas: (i) hydrogel characterisation and surface patterns; (ii) a single radial hydraulic fracture; and (iii) two coplanar radial hydraulic fractures.

The main objectives of this thesis are to obtain experimental results that can be used to improve our understanding and verify the accuracy of existing theoretical models. In the relatively unstudied coplanar case, we aim to create a new model that can capture the physical mechanisms and explore the universality of the dynamics as well as numerous different scenarios that may arise from the interaction of two fractures. Moreover, measuring the velocity field of the internal fracturing fluid is a crucial component of this research that has often been ignored in other experimental studies.

In Chapter 2 we introduce the mathematical formulation of the penny-shaped fluid-driven fracture problem. We discuss the assumptions involved in modelling this process and identify two regimes of propagation in an impermeable medium. We deduce scaling relations and fracture tip asymptotes for each regime, which are based on the dominant energy dissipation mechanism, material toughness or viscous dissipation.

The experimental setup and techniques are presented in Chapter 3. Dye attenuation and particle image velocimetry (PIV) methods are described, which allow measurements of the fracture extent, aperture and internal velocity field to be gathered.

Chapter 4 characterises the polyacrylamide hydrogels used as the elastic matrix in our experiments. We explain how to synthesise these gels to obtain reproducible Young's modulus and fracture energy values. Furthermore, we examine the range of possible material values and how these can be measured. We also discuss the fracture surface patterns that appear on the hydrogels after a fracturing experiment.

Experimental results for a single radial fluid-driven fracture are contained in Chapter 5. The experimental measurements of radius and aperture are compared with theoretical time-dependent scalings for the viscosity and toughness-dominated regimes introduced in Chapter 2. Velocity fields of the fracturing fluid flow are illustrated for both regimes, and deviations from the expected flow structure are discussed.

In Chapter 6 we study the propagation and coalescence of two coplanar fluid-driven fractures. We analyse the complete evolution of two fractures initiated in the same plane that first propagate independently of each other and then begin to interact and coalesce, forming a narrow bridge between them. First, we investigate the propagation and interaction between fractures pre-coalescence, which is caused by the existing stress state. Then, we document the behaviour of the bridge, where growth is localised after coalescence, and construct a theoretical model to explain this growth. This model identifies two regimes of propagation and appropriate scaling relations, as well as a characteristic transition timescale. Experimental results are used to explore the accuracy of the scalings produced, and PIV measurements provide insights into the flow structure that evolves during coalescence dynamics. We also analyse the profile shapes around the point of coalescence and possible universality of the dynamics. Additionally, we discuss numerous variations of the coplanar problem involving asymmetric coalescence, non-coalescing fractures and ridge formation on the surface of the fractures in the hydrogel.

Finally, in Chapter 7 we summarise the main results of the thesis and provide suggestions for further work.

Chapter 2

Theory

2.1 Introduction

In this chapter we will review and discuss the mathematical models of a single fluid-driven radial fracture, or penny-shaped crack. This is in order to motivate our experimental approach and illustrate the important physical mechanisms involved. This theoretical framework was first introduced by Spence & Sharp (1985) and Savitski & Detournay (2002).

2.2 Fluid-driven radial fracture model

We consider a radial fracture propagating into an impermeable elastic solid (Fig. 1.2(c)), in which the leak-off of the fracturing fluid into the medium is considered to be negligible. The fracture is driven by a constant volumetric injection rate Q of an incompressible fluid with dynamic viscosity μ. The elastic medium is characterised by Young's modulus E, Poisson's ratio ν and toughness K_{IC}. The following assumptions are then used to simplify the problem: (i) there is no fluid lag (i.e. the fluid front coincides with the fracture front); (ii) LEFM and lubrication theory for the fluid flow are applicable; (iii) the wellbore (injection) radius is negligible compared to the radius of the fracture (i.e. it can be modelled as a point source); (iv) the fracture propagates continuously in mobile equilibrium (i.e. the fracture will grow when the stress intensity factor equals the material toughness).

Applying these assumptions we can formulate the problem to find the crack aperture width $w(r,t)$, the fracture radius $R(t)$, and the net pressure $p(r,t)$.

2.2.1 Linear elasticity

We consider a fracture propagating in an infinite elastic medium. Two uniform compressive stresses σ_o and σ_r act perpendicularly and parallel to the fracture plane, respectively. We define the net pressure $p(r,t) = p_f - \sigma_o$, where p_f is the internal fluid pressure. Based on linear elasticity the mechanical deformation of the elastic matrix is given by the integral relation, which relates the net pressure $p(r,t)$ and the crack aperture $w(r,t)$ (Sneddon, 1951; Spence & Sharp, 1985),

$$p(r,t) = -E' \int_0^{R(t)} \frac{\partial w(s,t)}{\partial s} M\left(\frac{r}{s}\right) \frac{\mathrm{d}s}{s} \tag{2.1}$$

where E' is the plane strain modulus, which can be expressed in terms of E and ν as $E' = E/(1-\nu^2)$, and $M(\cdot)$ is the elasticity kernel,

$$M\left(\frac{r}{s}\right) = \begin{cases} \frac{2s^2}{\pi(s^2-r^2)} E\left(\frac{r}{s}\right), & r < s \\ \frac{2rs}{\pi(s^2-r^2)} E\left(\frac{s}{r}\right) + \frac{s}{r} K\left(\frac{s}{r}\right), & s < r \end{cases} . \tag{2.2}$$

$K(\cdot)$ and $E(\cdot)$ are complete elliptic integrals of the first and second kind respectively, of the form (Abramowitz & Stegun, 1964)

$$\begin{aligned} K(k) &= \int_0^1 \left[(1-t^2)(1-k^2t^2)\right]^{-1/2} \mathrm{d}t, \\ E(k) &= \int_0^1 (1-t^2)^{-1/2}(1-k^2t^2)^{1/2} \mathrm{d}t. \end{aligned} \tag{2.3}$$

Inversion of (2.1) gives rise to the following double integral expression for the elastic response to pressure (Sneddon & Lowengrub, 1969),

$$w(r,t) = \frac{8R}{\pi E'} \int_{r/R}^1 \frac{\xi}{\sqrt{\xi^2 - (r/R)^2}} \int_0^1 \frac{xp(x\xi R, t)}{\sqrt{1-x^2}} \, \mathrm{d}x \, \mathrm{d}\xi. \tag{2.4}$$

2.2.2 Lubrication theory

The flow of fluid in the crack is modelled using lubrication theory under the assumption that

$$w(r,t) \ll R(t), \tag{2.5}$$

which is clearly evident in the experiments described in Chapters 5 and 6, except at the initiation of the crack. This means that pressure variations across the aperture are small and along the gap they are proportional to fluid viscosity. For this theory to be valid it is also required that

$$Re = \alpha \frac{\rho U w}{\mu} = \frac{w}{R} \frac{\rho U w}{\mu} = \frac{\rho Q w}{2\pi R^2 \mu} \ll 1, \tag{2.6}$$

where Re is the Reynolds number, α is the aspect ratio of the fracture and U is the velocity scale of the fluid of density ρ and dynamic viscosity μ, so that fluid inertial effects are negligible.

A fluid mass balance gives

$$\frac{\partial w(r,t)}{\partial t} + \frac{1}{r}\frac{\partial}{\partial r}\left(r q(r,t)\right) = 0, \tag{2.7}$$

where $q(r,t)$ is the radial flow rate, and using Poiseuille's law, we obtain

$$q(r,t) = -\frac{w^3}{12\mu}\frac{\partial p(r,t)}{\partial r}. \tag{2.8}$$

Combining (2.7) and (2.8), we obtain a second nonlinear differential equation (Batchelor, 1967), known as Reynolds equation, which relates the aperture width to the pressure,

$$\frac{\partial w(r,t)}{\partial t} = \frac{1}{12\mu}\frac{1}{r}\frac{\partial}{\partial r}\left(r w^3(r,t)\frac{\partial p}{\partial r}\right). \tag{2.9}$$

2.2.3 Linear elastic fracture mechanics (LEFM)

The fracture propagation criterion is based on LEFM (Griffith, 1921; Irwin, 1957). The main assumption of LEFM is that the region near the fracture tip, where the behaviour of the medium is not elastic but undergoes plastic deformation or micro-cracking, is small compared to the crack size. For a penny-shaped crack we assume that the mechanism of fracturing is only tensile (opening), known as a mode I fracture. The other two modes of fracture are in-plane (mode II) and out-of-plane shearing (mode III), as seen in Fig. 2.1. For a mode I fracture, LEFM implies that a fracture will propagate, if the stress intensity factor (SIF) K_I equals the material toughness K_{IC}. Therefore the fracture propagation criterion can be written as (Kanninen & Popelar, 1985)

$$K_{\mathrm{I}} = K_{\mathrm{IC}}, \tag{2.10}$$

where

$$K_{\mathrm{IC}} = \sqrt{2\gamma_s E'}. \tag{2.11}$$

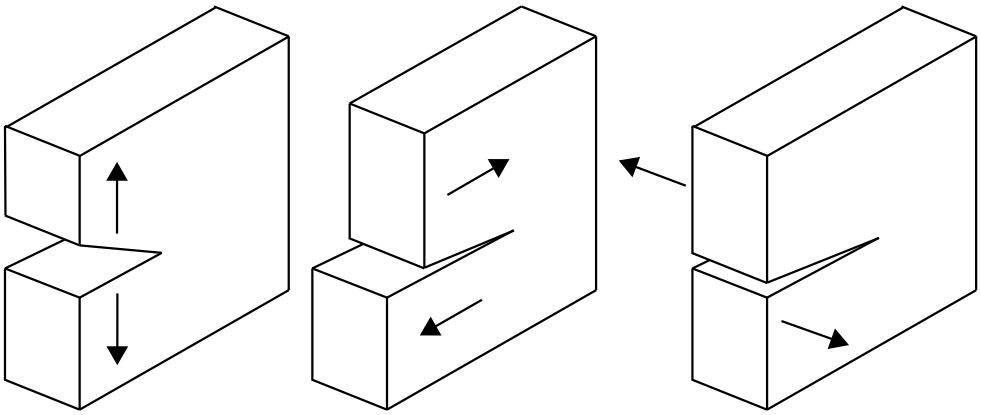

(a) I: Tensile (b) II: In-plane shear (c) III: Out-of-plane shear

FIGURE 2.1: The three modes of fracture.

Here, K_{IC} is a material property called the fracture toughness and γ_s is the fracture surface energy of the elastic medium, which can be defined as the energy required to create one unit of surface area.

The SIF K predicts the stress state near the tip of a crack. These stresses have the form (Irwin, 1957)

$$\sigma_{ij} = \frac{K}{\sqrt{2\pi x}} f_{ij}(\theta), \tag{2.12}$$

where x is the distance from the crack tip and f_{ij} is a function of θ, an angle to the plane of the crack. The function f_{ij} accounts for the specific geometry and loading conditions of the fracture.

For a penny-shaped fracture, where normal tractions $p(r,t)$ depend only on radial distance, this takes the form (Rice, 1968)

$$K_{\mathrm{I}} = \frac{2}{\sqrt{\pi R}} \int_0^{R(t)} \frac{p(r,t)}{\sqrt{R^2 - r^2}} r \mathrm{d}r. \tag{2.13}$$

2.2.4 Boundary conditions

The tip boundary conditions are set by a zero-fracture aperture at the tip,

$$w = 0, \quad r = R(t), \tag{2.14}$$

and a no flow condition $q = 0$. Then using Poiseuille's law (2.8), we derive

$$w^3(r,t)\frac{\partial p(r,t)}{\partial r} = 0, \quad r = R(t). \tag{2.15}$$

Using mass balance, we obtain the following relationship between the flow rate $q(r,t)$ and the injection constant rate Q

$$2\pi \lim_{r\to 0} rq(r,t) = Q. \tag{2.16}$$

Global mass balance is also used in the form

$$Qt = 2\pi \int_0^{R(t)} rw(r,t)\mathrm{d}r. \tag{2.17}$$

This set of equations, combining elasticity (2.4), lubrication theory (2.9), LEFM (2.10, 2.13), inlet conditions (2.16) or (2.17), and tip boundary conditions (2.14) or (2.15) forms a system that can be solved for $w(r,t)$, $p(r,t)$ and $R(t)$.

From this system of equations, we can construct two distinct regimes of fracture propagation through scaling arrangements from using elasticity (2.4), lubrication theory (2.9), LEFM (2.13) and global mass balance (2.17). The viscosity- and toughness-dominated regimes will arise from neglecting material toughness (LEFM) (2.13) and viscous fluid flow (2.9), respectively.

2.2.5 Scaling

We non-dimensionalise these equations using $R = R_0\hat{R}$, $t = t_0\hat{t}$, etc., where R_0, t_0 ,$\cdots$ are characteristic scales. The material parameters of viscosity μ' and toughness K' are defined in order to simplify the process (Savitski & Detournay, 2002), as

$$\mu' = 12\mu, \quad K' = 4\left(\frac{2}{\pi}\right)^{1/2} K_{\mathrm{Ic}}. \tag{2.18}$$

The system of equations is then transformed as follows:

- Linear elasticity, (2.4)

$$\hat{w} = \frac{8}{\pi}\frac{p_0 R_0 \hat{R}}{w_0 E'} \int_{\hat{r}/\hat{R}}^1 \frac{\xi}{\sqrt{\xi^2 - (\hat{r}/\hat{R})^2}} \int_0^1 \frac{x\hat{p}}{\sqrt{1-x^2}}\, \mathrm{d}x\, \mathrm{d}\xi. \tag{2.19}$$

- Lubrication theory, (2.9)

$$\frac{\partial \hat{w}}{\partial \hat{t}} = \frac{t_0 w_0^2 p_0}{\mu' R_0^2} \frac{1}{\hat{r}} \frac{\partial}{\partial \hat{r}} \left(\hat{r} \hat{w}^3 \frac{\partial \hat{p}}{\partial \hat{r}} \right). \tag{2.20}$$

- LEFM, (2.10) and (2.13)

$$\frac{K'}{p_0 R_0^{1/2}} = \frac{2^{7/2}}{\pi \sqrt{\hat{R}}} \int_0^{\hat{R}} \frac{\hat{p}}{\sqrt{\hat{R}^2 - \hat{r}^2}} \hat{r} \mathrm{d}\hat{r}. \tag{2.21}$$

- Global mass balance, (2.17)

$$\hat{Q}\hat{t} = 2\pi \frac{R_0^2 w_0}{Q t_0} \int_0^{\hat{R}} \hat{r} \hat{w} \mathrm{d}\hat{r}. \tag{2.22}$$

We then set the dimensionless groups in (2.19), (2.20), (2.21) and (2.22) to one respectively,

$$\frac{R_0 p_0}{w_0 E'} = 1, \tag{2.23}$$

$$\frac{t_0 w_0^2 p_0}{\mu' R_0^2} = 1, \tag{2.24}$$

$$\frac{K'}{p_0 R_0^{1/2}} = 1, \tag{2.25}$$

$$\frac{R_0^2 w_0}{Q t_0} = 1. \tag{2.26}$$

Using these dimensionless groups from our main equations, we introduce the viscosity and toughness-dominated scalings, denoting them with subscripts m and k, respectively.

2.2.5.1 Viscosity scaling

By combining groups from elasticity (2.23), lubrication theory (2.24) and mass balance (2.26), we arrive at the radial viscosity scaling, where

$$R_m = \left(\frac{Q^3 E' t^4}{\mu'} \right)^{1/9}, \tag{2.27}$$

upon dropping the non-dimensionalisation notation. From this scaling, we deduce the other viscosity-dominated scalings. For the fracture aperture it is

$$w_m = \left(\frac{Q^3 \mu'^2 t}{E'^2}\right)^{1/9}, \tag{2.28}$$

and for the net pressure it is

$$p_m = \left(\frac{\mu' E'^2}{t}\right)^{1/3}. \tag{2.29}$$

All of these are given in Table 2.1.

2.2.5.2 Toughness scaling

For the toughness scaling, we combine elasticity (2.23), LEFM (2.25) and mass balance (2.26) to obtain the radial scaling,

$$R_k = \left(\frac{QE't}{K'}\right)^{2/5}. \tag{2.30}$$

Once again, this enables us to deduce the other toughness scalings for the fracture aperture,

$$w_k = \left(\frac{K'^4 Qt}{E'^4}\right)^{1/5}, \tag{2.31}$$

and the net pressure,

$$p_k = \left(\frac{K'^6}{E'Qt}\right)^{1/5}, \tag{2.32}$$

as can be found in Table 2.1.

2.2.5.3 Transition

From the dimensionless groups (2.23)-(2.26), we can also identify the values of the scales,

$$R_0 = \frac{\mu' Q E'^3}{K'^4}, w_0 = \left(\frac{\mu' Q E'}{K'^2}\right)^{1/2}, p_0 = \left(\frac{K'^6}{\mu' Q E'^3}\right)^{1/2}, t_0 = \left(\frac{\mu'^5 Q^3 E'^{13}}{K'^{18}}\right)^{1/2}. \tag{2.33}$$

These scales represent the values at which viscous dissipation and material toughness have a comparable influence on the fracture dynamics. Therefore, at early and late times of propagation, viscosity and toughness-dominated limiting regimes describe

Physical parameter	Viscosity(m)	Toughness(k)
Fracture radius	$R_m(t) \approx \left(\frac{E'Q^3}{\mu'}\right)^{1/9} t^{4/9}$	$R_k(t) \approx \left(\frac{E'Q}{K'}\right)^{2/5} t^{2/5}$
Fracture aperture	$w_m(r,t) \approx \left(\frac{Q^3\mu'^2}{E'^2}\right)^{1/9} t^{1/9}$	$w_k(r,t) \approx \left(\frac{K'^4Q}{E'^4}\right)^{1/5} t^{1/5}$
Net pressure	$p_m(r,t) \approx \left(\mu' E'^2\right)^{1/3} t^{-1/3}$	$p_k(r,t) \approx \left(\frac{K'^6}{E'Q}\right)^{1/5} t^{-1/5}$

TABLE 2.1: Scaling expressions for time-dependence of viscosity and toughness-dominated regimes.

the propagation dynamics, respectively. Thus, these scales can be used to analyse experimental data and distinguish between regimes.

The scale t_0 can also be constructed by equating the viscous and toughness length scales, $R_m = R_k$. Solving for t, we can evaluate the characteristic time $t_{mk}(= t_0)$ it takes to transition from a viscous to toughness-dominated regime, where

$$t_{mk} = \left(\frac{\mu'^5 Q^3 E'^{13}}{K'^{18}}\right)^{1/2} \sim \left(\frac{\mu^5 Q^3 E'^{13}}{{K_{\mathrm{IC}}}^{18}}\right)^{1/2}. \tag{2.34}$$

Therefore, for $t \ll t_{mk}$, viscosity is the main source of energy dissipation, and for $t \gg t_{mk}$ material toughness dominates. Similarly, the same is true for scales involving radial extent (R_0), aperture (w_0) and net pressure (p_0).

2.3 Crack tip asymptotes

The solution near the crack tip is known to be characterised by a multiscale behaviour, which is related to the dominant energy dissipative processes that determine the length scales of the various tip asymptotes.

LEFM provides the asymptotic condition on the crack aperture w (Rice, 1968). This can be deduced from (2.4), by assuming that the pressure $p(r,t) = p_s(t)$ is only time-dependent in the toughness regime as the fluid flow within the crack is quasi-steady, which gives the profile of the crack shape,

$$w(r,t) = \frac{8R}{\pi E'} p_s(t) \sqrt{1 - \left(\frac{r}{R}\right)^2}. \tag{2.35}$$

Using the stress intensity factor (2.13), we can relate the pressure $p_s(t)$ to the material toughness,

$$K_{\mathrm{IC}} = \frac{2p_s(t)\sqrt{R}}{\sqrt{\pi}}. \tag{2.36}$$

By combining (2.35) and (2.36), we obtain

$$w_k \sim \frac{K'}{E'} x^{1/2}, \text{ as } r \to R, \tag{2.37}$$

where $x = R - r$ is the distance from the crack tip.

In a Newtonian fluid-driven fracture, the coupling between linear elasticity and lubrication theory can produce an intermediate asymptote (Spence & Sharp, 1985),

$$w_m \sim 2\,3^{7/6} \left(\frac{\mu}{E'}\right)^{1/3} V^{1/3} x^{2/3}, \quad \frac{x}{R} \ll 1, \tag{2.38}$$

where V is the mean fluid velocity at the tip, which is equal to the fracture tip velocity in a system with no fluid lag.

Thus, it needs to be determined at what length scale each asymptote dominates. Previous studies have found that the intermediate asymptote (2.38) emerges with the existence of a boundary layer of thickness $l = l_k^3/l_m^2$, where $l_k = (K_{\mathrm{IC}}/E')^2$ and $l_m = \mu V/E'$ are the length scales associated with LEFM and viscous dissipation, respectively (Garagash & Detournay, 2005). The boundary layer is characterised by the toughness asymptote (2.37) at the tip, and by the viscous dissipation asymptote (2.38) far away from the tip. The existence of the boundary layer signifies the dominance of an intermediate asymptote in the tip region on the scale of the fracture in the viscosity-dominated regime. This is the same as zero toughness where (2.38) can be considered as the tip asymptote.

2.4 Fluid lag

In this model, it is assumed that there is no lag between the fluid and the advancing crack tip. Garagash & Detournay (2000) found that the lag is negligible if

$$\kappa = \left(\frac{\sigma_0 K'^2}{\mu' V E'}\right)^{1/2} \gtrsim 1, \tag{2.39}$$

where σ_0 is the far-field compressive stress in the z-direction. In our experiments, the approximate value is $\sigma_0 \approx 100$ kPa, which comes from hydrostatic pressure. We consider the following typical parameters which match a viscosity-dominated

experiment: $\mu = 10$ Pa·s, $E = 367$ kPa, $\gamma_s = 3.6$ J m^{-2} and $V = 10^{-2}$ m s^{-1}. This produces a value of $\kappa \approx 3.6$, which corresponds to a predicted fluid lag of $\lambda \approx 8$ nm (Garagash & Detournay, 2000). This is negligible compared to the fracture extent of $\mathcal{O}(10^{-2}$ m). This value was calculated using the equation $\lambda = \Lambda L_\mu$, where $L_\mu = \mu' V E'^2/\sigma_0^3$ is a viscous dissipation length scale and Λ is a dimensionless lag length dependent on κ. The relationship between Λ and κ is obtained numerically in Garagash & Detournay (2000) by solving a full system of equations, from linear elasticity and lubrication theory in terms of κ, involving the net pressure, fracture opening and lag length.

2.5 Discussion

In this chapter, we have reviewed the mathematical formulation of a penny-shaped fracture, in particular establishing the existence of two regimes of propagation, where the dominant energy dissipation mechanism is either material toughness, or viscous flow (Savitski & Detournay, 2002; Spence & Sharp, 1985). Table 2.1 shows that the fracture radius power laws are very similar, with exponents of 4/9 and 2/5 for viscosity and toughness, respectively. Of course, these time-dependent power laws include a pre-factor on the right-hand side which will help to distinguish between regimes. The aperture scaling provides more clarity, with the time-dependent power laws for viscosity and toughness varying between exponents of 1/9 and 1/5, respectively. Perhaps the best method of distinguishing regimes is the crack tip behaviour introduced in § 2.3. Here, we have outlined how the crack tip shape should respond under corresponding limiting regimes. The toughness and viscous asymptotes vary with distance from the fracture propagation edge, with exponents of 1/2 and 2/3, respectively. We will explore these theoretical predictions in Chapter 5 through the use of laboratory experiments, which allow us to clearly identify fracture propagation regimes in both time-dependence and fracture shape.

Chapter 3

Experimental methods

3.1 Introduction

In this chapter the general experimental setup and implementation steps are described. We also detail the experimental techniques involved in the measurement of physical parameters, such as fracture extent, aperture and fluid velocity. Crucially, this enables us to create three dimensional images of the fractures and investigate the flow-fields within them.

3.2 Experimental setup

The experimental setup consisted of setting a hydrogel of dimensions $100 \times 100 \times 77$ mm around an injection needle of radius 0.81 mm, which was centred in the middle of a transparent acrylic chamber as depicted in Figs. 3.1 and 3.2(a). The gel matrix is sufficiently large so that the free surface has a negligible effect on the stress state near the injection point and thus, the induced stress field is symmetric (Bunger, 2005). A incompressible Newtonian fluid was pumped at a constant volumetric rate using a syringe pump (WPI AL6000, HA PhD Ultra).

A high speed camera (Dalsa Falcon 2 4MP), with a range of up to 120 frames per second (fps), was used to capture the fracture growth, as seen in Fig. 3.2(b). The fluids used include water, glycerin, silicone and golden syrup, with viscosities ranging from $\mu \sim 10^{-3} - 10^{1}$ Pa·s. All viscosity measurements were obtained using a variety of U-tube viscometers.

The propagation of these fluid fractures was clearly observed due to the transparent nature of the gels. The radial fracture profile was found by dyeing the fluid so that it

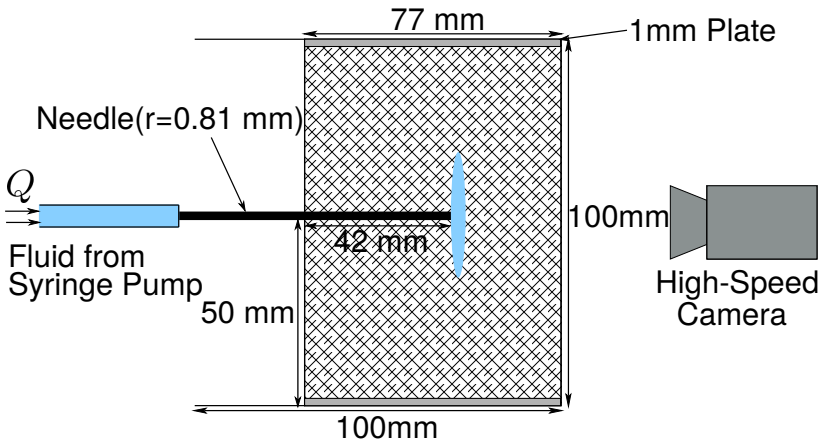

(a) Elevation view

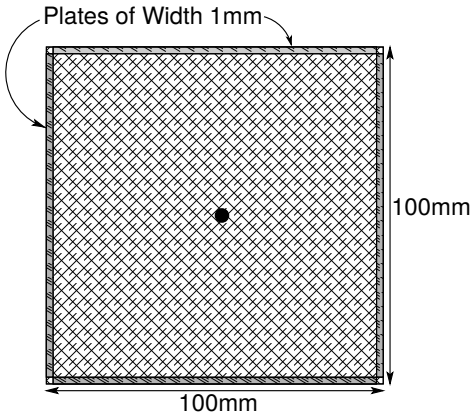

(b) Plan view

FIGURE 3.1: Schematic diagrams of the experimental setup.

could be easily distinguished from the surrounding medium. The radius measurements at each time step were then taken from light intensity values. We constructed 20 lines with equally spaced angles between 0 to 2π radians, that radiate from the injection source, with the average of these is chosen as the radius. The Digiflow software was used extensively in processing the videos and taking measurements (Dalziel, 2006). With these measurements we were able to achieve a spatial resolution of 0.04 mm/pixel.

The experimental errors were calculated by estimating uncertainties in the physical parameters of the hydrogels Young's modulus E ($\pm 10\%$) and fracture energy γ_s ($\pm 10\%$), and experimental uncertainties in the injection rate Q ($\pm 10\%$), the viscosity μ ($\pm 5\%$) of the injected fluid, and measurement errors, time t (± 0.2 s) and radius R (± 0.5 mm).

(a) Acrylic chamber

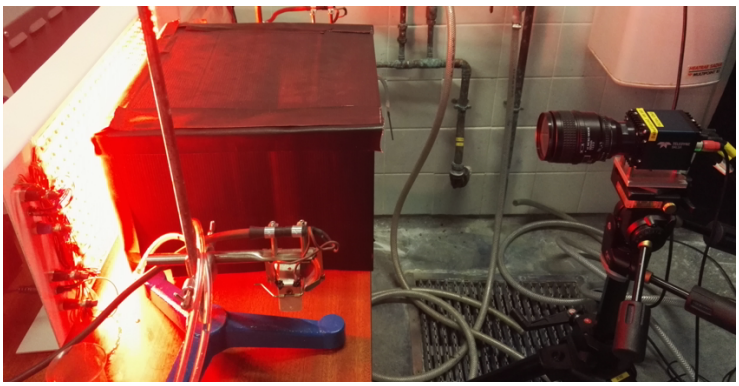

(b) Lab setup

FIGURE 3.2: Photos of (a) the acrylic chamber and (b) the laboratory view of the experimental apparatus.

3.2.1 Principal stresses

We consider our cube of gel as being acted upon by three principal stresses as in Fig. 3.3. If we wish the radial fracture to propagate radially and perpendicularly to the injection needle, for example in the x-y plane, we must orientate the needle parallel to the minimum confining stress in the z-direction. This is because the fracture will propagate perpendicular to this direction, due to the fact that the radial crack is a tensile fracture (mode I) and opens in the direction of least resistance. Therefore imposing small initial principal stresses σ_x and σ_y, where $\sigma_x = \sigma_y$, will achieve the desired fracture geometry. To implement this we inserted four rectangular plates of width 1 mm parallel to the needle, on each side of the gel, as seen in Fig. 3.1(b). These are made from polycarbonate plates, which were chosen due to their transparency, strength and re-usability. The stresses $\boldsymbol{\sigma}$ and strains $\boldsymbol{\varepsilon}$ can be linearly related using Hooke's Law. In Cartesian coordinates this has the form

$$\begin{aligned} \varepsilon_x &= \frac{1}{E}[\sigma_x - \nu(\sigma_y + \sigma_z)], \\ \varepsilon_y &= \frac{1}{E}[\sigma_y - \nu(\sigma_x + \sigma_z)], \\ \varepsilon_z &= \frac{1}{E}[\sigma_z - \nu(\sigma_x + \sigma_y)], \end{aligned} \tag{3.1}$$

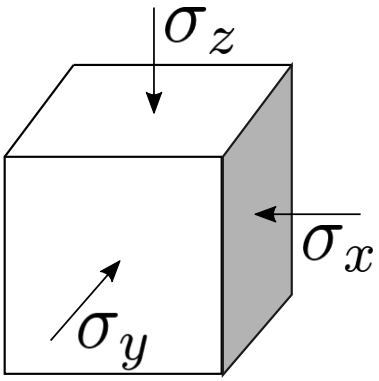

FIGURE 3.3: Schematic of *in-situ* principal stresses acting on the gel matrix.

where $\varepsilon = (l - L_0)/L_0$ is the strain on the deformed solid, L_0 is the original length and l is the final length after deformation. ε is positive for an increase and negative for a decrease in the original length L_0. Similarly, σ is negative for compressive stress and positive for tensile stress. Thus, when the plates of width 1 mm are inserted on each side of the 100 mm chamber $\varepsilon_x = \varepsilon_y = -1/50$ and using $\nu = 0.5$ (§ 4.3.1), it follows that

$$\varepsilon_z = \frac{1}{25}. \tag{3.2}$$

Thus, the value of the principal stresses can be expressed as

$$\sigma_x = \sigma_y = \sigma_z - \frac{E}{25}. \tag{3.3}$$

Therefore, $\sigma_z = \sigma_x + E/25$ is the minimum principal compressive stress and the tensile fracture opens in the z-direction. This means that the fracture propagates in the x-y plane.

3.2.2 Order of experimental steps

These experiments can be quite challenging to carry out, due to the delicate nature of the hydrogel and importance of setting the injection needle properly to stop any leakage of the fracturing fluid. Therefore, after much trial and error, it has been identified that when setting up an experiment it is crucial that certain steps are undertaken in a particular order to ensure a successful outcome:

(i) Initially the lighting and camera settings are configured depending on the specific measurements required, as described in detail in §§ 3.3 and 3.4.

(ii) The injection needle is clearly marked to a specified depth and placed in the chamber.

(iii) The gel is then synthesized around this needle, following the procedure detailed in § 4.2.1, and left for approximately two hours to ensure the chemical reaction is completed.

(iv) The injection needle is then removed from the gel by gently rotating and pulling it upwards. Any gel remaining within the needle is cleared out by using a smaller diameter needle and then flushed out with water. The outside of the needle is also wiped down, however gel does not normally attach to this surface.

(v) Following this four thin polycarbonate plates are placed between the sides of the gel and chamber. As there is no adhesion of the gel to the acrylic chamber, the introduction of the plates does not damage the gel matrix. The placement is done very slowly to ensure no fracturing occurs and the matrix is not deformed rapidly.

(vi) Previously prepared fracturing fluid of a known viscosity is then connected from a syringe to the needle using Nalgene plastic tubing and Luer fittings. All bubbles are then removed from the apparatus by pushing the syringe until fluid is present at the needle tip. This syringe is then connected to the pump.

(vii) The most important step then occurs when placing the needle back into the gel matrix. This is done by partially turning the screw that fixes the needle into place on the top of the chamber, so that it can only be moved at a slow speed, mitigating the chance of a large movement causing pre-fracture. The needle is pushed down until the tip is in contact with the gel at the base of the pre-cast borehole. This should match the marking initially placed on the needle. It is crucial that the whole tip is in contact with the gel so no fluid escapes along the sides of the needle, resulting in either no fracture or fracture at an unquantifiable reduced rate.

(viii) Fracturing can then proceed once the camera is primed for recording.

3.3 Aperture measurement

A dye attenuation method was used to measure fracture aperture. This is a process where the absorption of light is used to relate to aperture measurements (Bunger, 2006). A red LED light sheet with a diffuser was used as background lighting to provide a uniform monochromatic light source (Fig. 3.4(a)). A black container was also placed around the fracturing experiment to minimise the effects of external light interference, which can be seen in Fig. 3.2(b). The injected fluid was dyed with methylene blue, which strongly absorbs at the wavelength of the red light source, and the absorption of the background light is then directly related to the amount of fluid through which it passes.

3.3.1 Calibration

To correlate intensity values across the dyed fluid region with crack aperture, a calibration experiment had to be conducted. This experiment involved constructing a glass wedge with a linearly increasing thickness from $0 - 8$ mm. The wedge was filled with dyed fluid (Figs. 3.4(c) and 3.4(e)), which was the fracturing fluid used during the experiment. The wedge was then placed in our acrylic container (Fig. 3.2(a)) and a polyacrylamide gel formed around it, in order to take into account the absorption of light by the gel matrix itself. We denote the intensity of the uniform background light that has travelled through the polyacrylamide gel only by I_0, and the intensity distribution of light that passed through the fluid-filled region by I. Normalising the fluid-filled light intensity with the background intensity through the gel, the absorption of the light due to the matrix alone can be excluded. We plot this normalisation I/I_0 versus the aperture of the wedge in Figs. 3.4(b) and 3.4(d). A polynomial fit to the calibration data was then calculated and used to relate the light intensity data to aperture measurements for fluid-filled fractures, under the assumption that the fracture is symmetric about its mid-plane.

Particular concentrations of dye can be added to the fluid to obtain more accurate measurements of certain regions. For example, when focusing on small aperture near the crack tip a higher concentration is used, as in Figs. 3.4(b) and 3.4(c), where the calibration curve begins to flatten after 2 mm and is not accurate after this point. To get a more complete measurement of the whole fracture aperture, a less concentrated solution can be used (Figs. 3.4(d) and 3.4(e)).

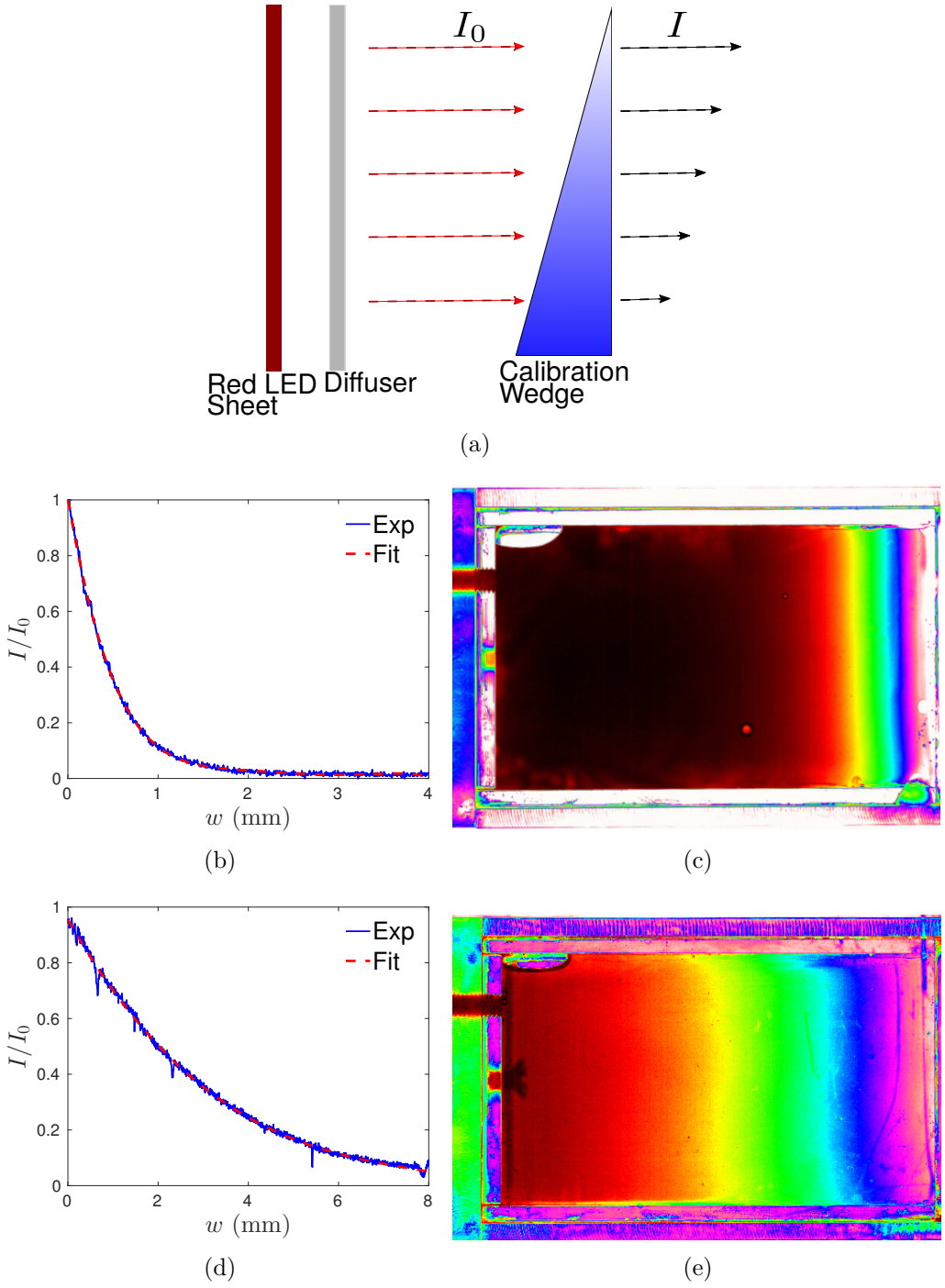

FIGURE 3.4: (a) A red monochromatic light of uniform intensity I_0 is obtained from an LED light sheet and diffuser. This light then passes through the hydrogel and calibration wedge or fluid fracture with blue dye, and emerges at a diminished intensity I depending on the path length through the fluid. (b),(d) The normalised light intensity I/I_0 versus the corresponding aperture of the fluid-filled region for given dye concentrations. (c),(e) Experimental images of a calibration.

3.4 Particle image velocimetry (PIV)

In order to capture and explore the fluid flow within the fracture, we used the optical method of PIV. This flow visualisation technique allows instantaneous velocity measurements to be obtained, by illuminating a particular section of flow with particles present and using the displacement of the particles in the flow to calculate velocity.

We created a 10 mm thick light sheet in the plane of fracture growth within the hydrogel, using two arc lamps that penetrate through slits on either side of the acrylic container. The rest of the container was covered to hinder any other sources of light entering the gel, as seen in Fig. 3.5. The fracturing fluid was then seeded with tracer particles (polyamid or orgasol) 40-50 μm in diameter and density $\rho_p = 1.02$ g cm^{-3} that are large enough to track within the fracture but have a negligible influence on the flow itself. Thus, the settling or terminal velocity v_t of the spheres can be calculated by (Batchelor, 1967)

$$v_t = \frac{2}{9}\frac{(\rho_p - \rho_f)}{\mu} g R_p^2, \tag{3.4}$$

where ρ_f is the velocity of the fluid, g is the acceleration due to gravity and R_p is the radius of the particle. For a typical experiment with $\rho_f \approx 1.24$ g cm^{-3} and $\mu \approx 1$ Pa·s, $v_t \approx 0.3$ μm s^{-1}. In our experiments the flow within the fracture is approximately $\mathcal{O}(1$ mm s$^{-1})$, so the buoyancy effect of the particles maybe be neglected relative to the flow speeds. Moreover, the particle Reynolds number $Re_p = \rho_f U 2R_p/\mu \approx 10^{-4}$, where U is the relative velocity, shows the particles have a negligible effect on the flow.

Before injecting the fluid, a drop of a surfactant, Finish Rinse Aid, was also added to the particles to inhibit the clustering of particles together. When the fracture begins to propagate, the fracturing fluid with entrained particles is illuminated so that particles are visible relative to the ambient. In some experiments a small amount of fluorescein was introduced to the fracturing fluid so that the edge of the fracture would be clearly distinct, while also not hindering the particle tracking by over powering the light intensity of the particles. This allowed a mask to be placed around the area where particles needed to be tracked, saving computational time and facilitating simultaneous measurements of fracture extent. The two dimensional velocity data of the fluid in the plane of fracture propagation was then determined by capturing images at 50-120 fps depending on the experiment. The algorithm used in processing the experimental images to produce the instantaneous velocity measurements is part of the Digiflow software pioneered by Prof. S. B. Dalziel (Dalziel, 2006).

Since the fracture width (≈ 5 mm) is smaller than the width of the light sheet, it is important to note which velocity is being measured from PIV. The flow within the fractures being considered here have a parabolic profile with a maximum along the centre line and no slip near the fracture surfaces. Most particles will therefore be located around the midpoint of the fracture width as this is where fluid velocity is largest. Thus, it is assumed that the velocity measured from PIV corresponds to the maximum fluid velocity.

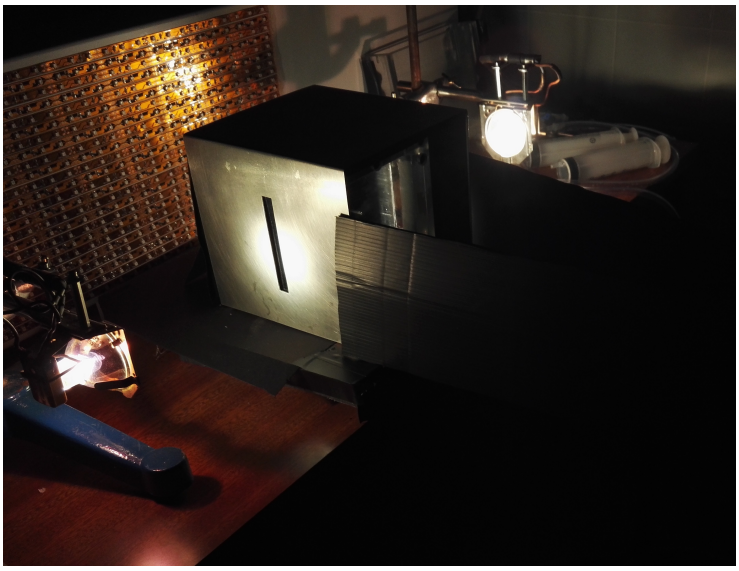

(a)

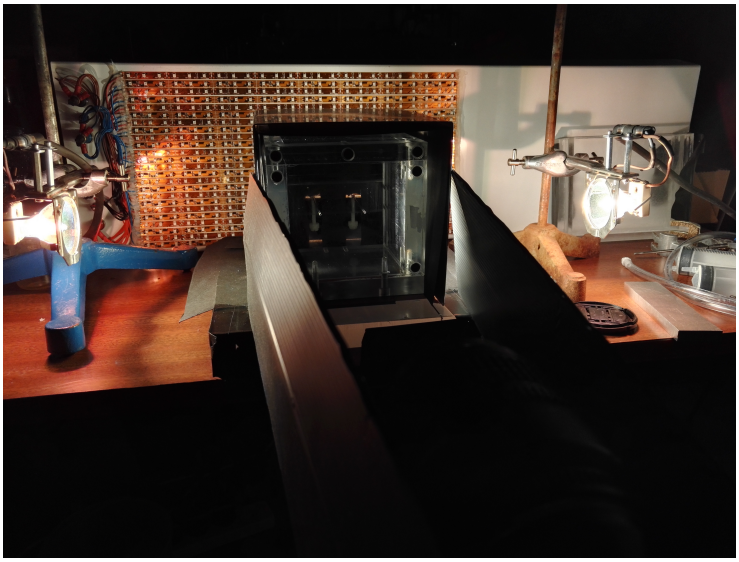

(b)

FIGURE 3.5: Laboratory view of the PIV experimental apparatus.

Chapter 4

Hydrogel properties and fracture surface patterns

4.1 Introduction

In this chapter, we describe how to construct polyacrylamide hydrogels to study the processes linked to fluid-driven fractures. These transparent, linearly elastic and brittle gels permit fracturing at low pressures and speeds, allowing accurate measurements to be obtained. In the context of hydraulic fracturing, the broad range of modulus and fracture energy values that are attainable, allow experimental exploration of particular regimes of importance. We also describe the measurements of material properties and how fracture energy may be deduced from hydraulic fracturing experiments. Lastly, we analyse the fracture surface patterns that emerge from fluid-driven cracks occurring within the medium. These patterns are similar to those that have been observed in other materials and we comment on their fractal-like nature. The majority of the content discussed in this chapter has been published during my PhD (O'Keeffe & Linden, 2017).

4.2 Hydrogel

Polyacrylamide hydrogels are widely used as materials in biology as cell culture substrates and for gel electrophoresis to separate proteins. The gel is a highly swollen network of cross-linked acrylamide polymer chains. The material constants, such as elasticity and stiffness, of this gel can be altered by varying the quantity of monomers

and cross-linker present. These hydrogels have been approximated as linear elastic materials as they retain a constant storage modulus while under a large range of strains (Storm *et al.*, 2005).

In the context of fracturing, these gels have been used to study the propagation of dynamic fractures and shown to fracture similarly to other brittle materials (e.g. PMMA and glass) (Livne *et al.*, 2004). This medium has been used extensively in the study of micro-branching and oscillation instabilities involved in the dynamics of two dimensional rapid fractures (Goldman *et al.*, 2012; Livne *et al.*, 2007, 2005).

Fracture dynamics are normally extremely hard to capture, due to difficulties in visualising the tip of a crack moving at velocities of the order of the Rayleigh wave speed. One of the main advantages of brittle polyacrylamide gels is that Rayleigh wave speeds are $\sim 5 - 20$ m/s and hence, are 2-3 orders of magnitude lower than in 'standard' brittle materials (glass ~ 3500 m/s, PMMA ~ 1600 m/s) (Livne *et al.*, 2004). This slows down the fracturing process, allowing accurate measurements to be obtained with the use of a high speed camera.

Recently however, Denisin & Pruitt (2016) have reviewed measurements of the mechanical properties of hydrogels, noting that 'reported elastic modulus for the same formulations differ widely' and depend on 'polyacrylamide formulation, ployacrylamide temperature, gelation time and storage duration'. In this chapter we will describe the production of hydrogels with consistent and predictable mechanical properties and a novel experimental setup involving brittle, heavily cross-linked polyacrylamide hydrogels used to investigate fluid-driven fracture. This setup will also allow simple measurements of fracture energy and stress intensity for these gels, with varying concentrations of monomers and cross-linking. Moreover, it provides a platform to examine step-line patterns present on the crack surfaces. Calculating the fractal dimension of these patterns can exhibit similarities with geological samples and other fracture surface phenomena.

4.2.1 Gelation of polyacrylamide hydrogels

The hydrogels were prepared by free radical polymerization of acrylamide (Sigma Aldrich) as the monomer and N,N′-methylenebis (acrylamide) (Sigma Aldrich) as the cross-linker in aqueous solution. This means any oxygen present in the solution will inhibit the polymerization. The initiator ammonium persulphate (APS) and accelerator N,N,N,N′-tetramethylethylenediamine (TEMED) (Sigma Aldrich) then catalyze the reaction.

The gels contain differing amounts of acrylamide produced from a 40% w/v (weight/volume) stock solution and bisacrylamide in solid form, which are added to a certain amount of demineralised water to give the desired % w/v of each chemical. The weight of bisacrylamide was measured using a scale with an accuracy of 0.01 g. The solution is mixed using a magnetic stirrer for a few minutes to ensure all the solid acrylamide has dissolved. The beaker containing the solution is then degassed for 10-15 minutes to counteract oxygen inhibition of the reaction, which is crucial for reproducibility of the gel. Degassing is done by placing the solution inside a vacuum chamber, which is connected to a pump. A low pressure environment is then created, causing air to be removed from the liquid. Next, 0.075% w/v of APS was added and finally 0.05% v/v of TEMED using a pipette. All volume percentages are of the final volume.

We constructed gels of dimensions $100 \times 100 \times 77$ mm, which is equivalent to 770 mL of volume. The total percentage of acrylamide monomer and bis-acrylamide cross-linker varied from $8 - 15\%$ w/v and $2.5 - 6\%$ wt. (cross-linker weight/monomer weight), respectively. Each gel was prepared at room temperature (20°C) and the solution was left for over 2 hours allowing gelation to occur fully. During this gelation period the chamber containing the solution is covered with parafilm tape, as an additional precaution against oxygen inhibiting the polymerization. We also tested fixing an acrylic plate to be in contact with the free surface of the solution during gelation. This was done to help the formation of a smooth free surface, absent from small ripples or micro-cracking. These defects were more often encountered in high percentage cross-linker gels and are thought to be caused by small amounts of evaporation. Pouring a small amount of isopropanol or butanol on top of the gel solution also produces a clear free surface and prevents oxygen inhibition.

4.2.2 Properties

Polyacrylamide gels are recognised as linearly elastic materials in the literature (Johnson & Harley, 2011; Reinhart-King *et al.*, 2003). These gels consist of cross-linked polymer chains. Their elastic properties are determined by the concentration of monomers, acrylamide, and cross-linking molecules, bis-acrylamide. An increase in the monomer % w/v will result in an increase in the Young's modulus and fracture energy, if the cross-linking % wt. is held constant. Furthermore, increasing the cross-linking % wt. will make the gel more brittle and decrease the fracture surface energy. This complicated relationship means that only a few measurements have been found in

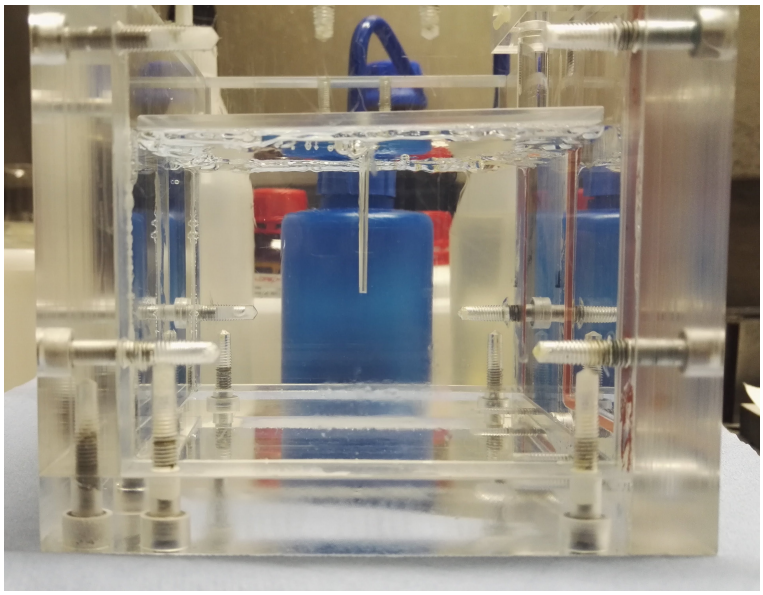

FIGURE 4.1: Photo of synthesized hydrogel with pre-cast wellbore. A blue bottle behind the gel exhibits the high level transparency.

the literature for fracture energies at particular gel percentages (Tanaka *et al.*, 2000; Zhang *et al.*, 2005). Normally these fracture energy values are obtained from peel tests. Here we approached the measurement of these values using a technique outlined in § 4.3.3. It has been shown that an increase in monomer will always lead to an increase in Young's modulus (Denisin & Pruitt, 2016). However, an increase in cross-linker will also increase the gel modulus up to around 7% wt. cross-linking. If the cross-linking is increased beyond this, the gels become heterogeneous and the value of the Young's modulus will plateau (Denisin & Pruitt, 2016).

These cross-linked polyacrylamide gels are extremely transparent, which is evident in Fig. 4.1. This level of transparency is a major advantage of the medium and permits high precision optical measurements.

Polyacrylamide gels are also elastic and brittle materials. Elasticity and brittleness are two different properties. However, they are not independent for elastic solids. Ideally fracture toughness K_{IC} follows the relation (2.11), which incorporates both elasticity and brittleness properties in the Young's modulus and fracture surface energy, respectively.

Rate-dependent fracture surface energies γ_s have been observed in several gel systems. Chemically cross-linked polyacrylamide hydrogels exhibit a rate dependence that decreases with increasing density of chemical cross-links (Tanaka *et al.*, 2000). Since we are using heavily cross-linked hydrogels we will assume the fracture energy

to be constant, which can be determined from the measurements obtained in § 4.3.3. This is an advantage over gelatin systems where the fracture energy varies linearly with crack velocity, and the rate sensitivity increases with the amount of physical cross-linking (Baumberger *et al.*, 2006).

The permeability of these gels can be low and comparable to that observed in unconventional hydrocarbon reservoirs. In shale gas formations the expected permeability is in the range of $10^{-6} - 10^{-8}$ Darcy, while in polyacrylamide hydrogels permeability values can range from $10^{-7} - 10^{-8}$ Darcy (White, 1960). Due to this range of values, we assume that leak-off into the gel from the fluid fracture is negligible for the duration of a typical experiment.

4.3 Results

4.3.1 Poisson's ratio

We have conducted a series of compression tests on sample rectangular cuboid gels, with dimensnions 5.1 cm × 4.2 cm × 3.6 cm, to obtain material properties such as the Poisson's ratio and observe the variability when concentrations are altered. This was done on an Instron 3345, which used parallel plates to measure compressive stress and strain (Fig. 4.2). A sample stress-strain graph can be seen in Fig. 4.4(c) for a 13 - 4 % gel (13 % w/v monomer and 4 % wt. cross-linker weight), which also allowed Young's moduli values to be determined using this method. Poisson's ratio values were determined by compressing the gel sample in the axial direction a certain small distance relative to the sample height. Poisson's ratio ν, was then calculated by measuring the growth in the transverse direction and using

$$\nu = -\frac{\varepsilon_{\text{trans}}}{\varepsilon_{\text{axial}}}, \tag{4.1}$$

where $\varepsilon_{\text{trans}}$ and $\varepsilon_{\text{axial}}$ are the transverse and axial strains, respectively. $\varepsilon_{\text{trans}}$ is positive and $\varepsilon_{\text{axial}}$ is negative for axial compression. The maximum value of ν is 0.5, which corresponds to a perfectly incompressible medium.

The results of these tests can be seen in Fig. 4.3. This produced an approximate Poisson's ratio $\nu \approx 0.48$, which agrees with the accepted view that the hydrogels can be treated as incompressible (Boudou *et al.*, 2006). For all the experimental analysis conducted during my PhD, ν was given the value 0.5. These compression tests were undertaken with the help of Dr. Finn Box (Oxford).

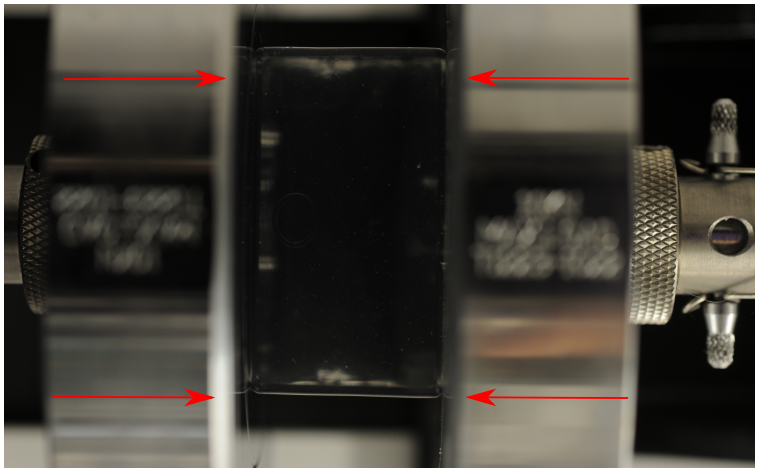

.

FIGURE 4.2: Photo of a hydrogel sample between parallel plates during compression tests, with the direction of compression shown by the red arrows

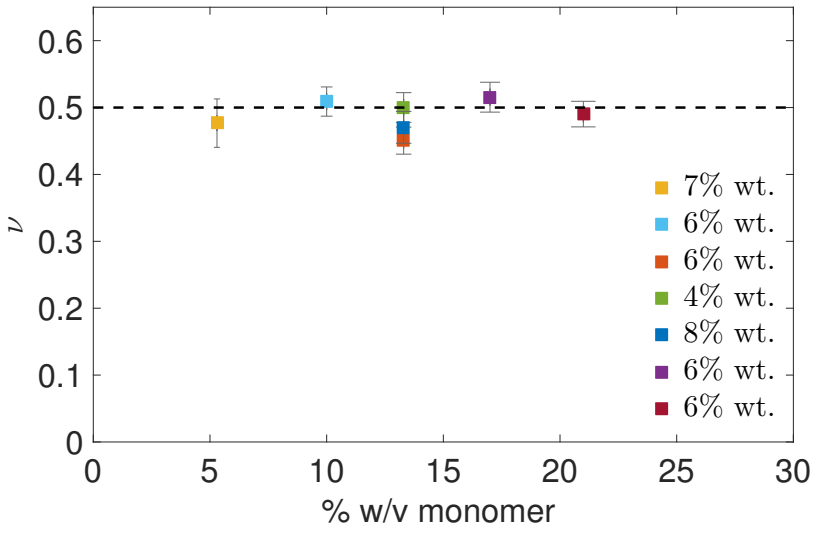

FIGURE 4.3: Plot of ν, the Poisson's ratio values, versus % w/v monomer for gels of various concentrations, with the legend showing the percentage of cross-linking.

4.3.2 Young's modulus

Using the principle of determination of Young's modulus by Hertzian contact, or indentation with a solid sphere (Hertz, 1881; MacKay & Kumar, 2013), we calculated a range of elastic moduli for different monomer to cross-linker ratios. This method was carried out using a TA.XT Texture Analyser (Stable Micro Systems). A sphere of radius $a = 0.63$ cm was indented a certain distance (≈ 2.7 mm) onto the surface of the hydrogel, as seen in Fig. 4.4(a), and the force measured. This indentation depth corresponded to 5-10 % of the height of the sample, which satisfies the assumption that the indentation is insignificant in comparison to the sample height. For a perfectly elastic solid, if the surface is displaced a distance δ under a force F, the plane strain modulus E' is given by the relation (MacKay & Kumar, 2013)

$$E' = \frac{E}{1-\nu^2} = \frac{3}{4a^{1/2}}\frac{F}{\delta^{3/2}}. \tag{4.2}$$

However, to exclude surface tension effects in the initial stages of indentation, the slope of the linear section of a $\delta^{3/2}$ versus F plot, $\Delta F/\Delta\delta^{3/2}$, is used to calculate the Young's modulus E,

$$E = \frac{3(1-\nu^2)}{4a^{1/2}}\frac{\Delta F}{\Delta\delta^{3/2}}. \tag{4.3}$$

An example of this can be seen in Fig. 4.4(b). Moreover, this expression models the indenter as a parabolic geometry. It is valid to use this expression for a spherical indenter provided the indentations are reasonably small so that $\delta/a < 1$. In these experiments $\delta/a \approx 0.4$, so the model is valid.

The results of these tests can be seen in Fig. 4.4 and Table 4.1. We conducted two indentation experiments at different places on the gel surface for each sample. The maximum deviation from the average value was always less than 2.5%. The error bars are estimated from measurement uncertainty on the slope calculation. From the figures we can clearly see that increases in the amount of monomer and cross-linker in the ranges shown, both contribute to an increase in Young's modulus. From Fig. 4.4 it is evident that monomer percentage has a larger effect on the elastic modulus than cross-linking. The linear fits seen in Figs. 4.4(d) to 4.4(f) have a slope m and intercept c. It has been shown that higher percentages of cross-linking can lead to a plateau in the elastic modulus values and that the relationship is more complex in this range with heterogeneity occurring (Denisin & Pruitt, 2016).

A surface may be fitted to the range of moduli values using a polynomial of the form

$$E(x, y) = c_0 + c_{10}x + c_{01}y + c_{11}xy + c_{02}y^2, \tag{4.4}$$

where $c_0 = 267.3 \pm 12.8, c_{10} = 62.9 \pm 10.3, c_{01} = 148.2 \pm 10.4, c_{11} = 39.07 \pm 12.7, c_{02} = 12.42 \pm 11.9$ and x, y correspond to the cross-linking and monomer percentages which are normalised by the means 4.8 and 13.77, respectively. This fit has an r^2 value of 0.98 and a plot of this surface polynomial can be seen in Fig. 4.5. This fit only corresponds to values in the range $8 - 21$ % w/v monomer and $2.5 - 6$ % wt. cross-linker. More experiments are likely to fine tune this fitting and fill out the parameter space, however it still provides a good current estimate for other moduli values dependent on gel concentrations in this range.

Experimentally we can obtain a wide range of values for the Young's modulus, with values varying from at least $50 - 700$ kPa. This was one of our main motivations for conducting experiments in this medium, as it allowed us considerable variation in the transition time (equation (2.34)) derived for hydraulic fractures.

4.3.3 Determination of stress intensity and fracture surface energy

We can use our measurements of fracture aperture, crack tip behaviour and radial extent to consider the stress intensity factor (Bunger, 2006). The fracture aperture is known from dye attenuation measurements of the internal fracturing fluid. This can be done in the toughness limiting regime, where the crack tip LEFM asymptote (2.37) relates the fracture aperture, distance from the tip and stress intensity. We consider only mode I opening where we can use the stress intensity factor K_I to estimate the fracture toughness K_{IC} of the hydrogel matrix, under the LEFM assumption that propagation occurs when (2.10) is satisfied.

Plotting the opening for 50% of the fracture normalised according to (2.37) produces Fig. 4.6, where the stress intensity factor K_I is the value averaged over the crack tip region. The aperture is plotted for 10 time steps with the black line representing the fit. This particular experiment corresponds to a gel concentration of 10% w/v monomer and 2.5% wt. cross-linker. From the propagation criterion we assume $K_I = K_{\mathrm{IC}}$ and we can deduce that $K_{\mathrm{IC}} = 1262 \pm 72$ Pa m$^{1/2}$. Thus we can use equation (2.11) to estimate the fracture surface energy of this particular gel configuration to be $\gamma_s \approx 5.6$

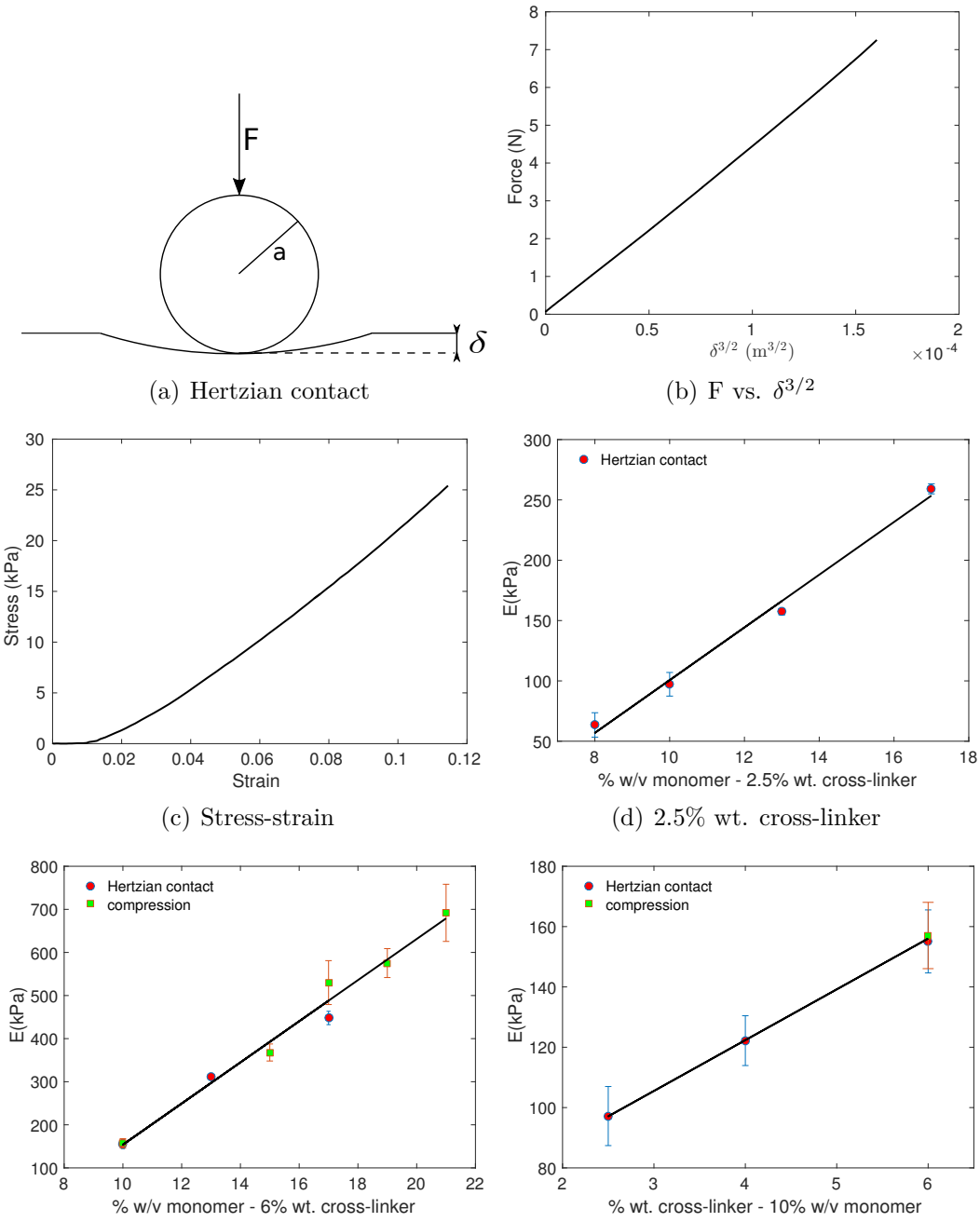

(a) Hertzian contact (b) F vs. $\delta^{3/2}$

(c) Stress-strain (d) 2.5% wt. cross-linker

(e) 6% wt. cross-linker (f) 10% w/v monomer

FIGURE 4.4: Characterisation of the gel Young's modulus. (a) Experimental technique of Hertzian contact using spherical indentation. (b) Force versus $\delta^{3/2}$ for a 13 - 6 % gel. (c) Sample stress-strain curve from a compression test of a 13 - 4 % gel. (d),(e) Young's modulus versus monomer % w/v for fixed cross-linking of 2.5% wt. ($m = 22.5, c = -121.5$) and 6% wt. ($m = 47.5, c = -316.7$), respectively. (f) Young's modulus versus cross-linking % wt. for fixed monomer concentration of 10% w/v ($m = 16.6, c = 59.1$).

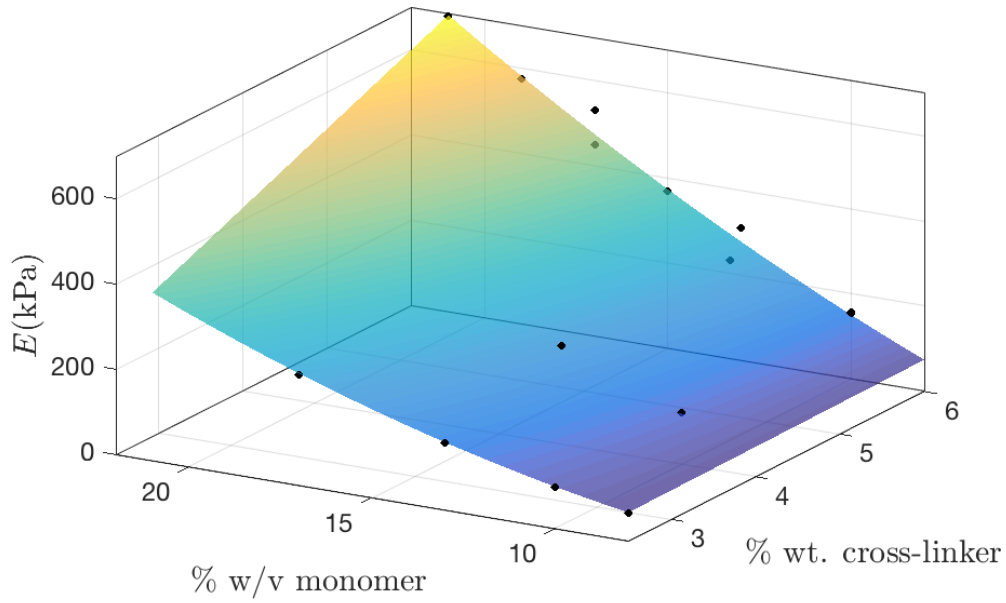

FIGURE 4.5: Three dimensional plot of the surface fit to Young's moduli values, which are dependent on both the monomer and cross-linking gel percentages. This was done using a linear least squares algorithm.

J/m^2. The noise close to $x/R = 0$ is due to the minuscule thickness near the crack tip. The dye attenuation value is extremely small in this area and is comparable to the noise in the experiment due to the limitations of our calibration. However, the data clearly follow a specific trend before the noise becomes significant. The constant stress intensity value observed all along the fracture tip, retrieved from using LEFM, suggests that the assumption of a homogeneous brittle material is valid.

This technique was then applied to a number of gel concentrations, the results of which can be seen in Table 4.1 and Fig. 4.7. In Fig. 4.7(a) we can see that the stress intensity value increases with monomer percentage, as expected. K_I is similar for both 2.5 and 6 % wt. cross-linking, with 2.5 % wt. having marginally higher values.

The similar behaviour in stress intensity values means that the fracture energies for the higher cross-linked gels, calculated using (2.11), will be lower due to larger moduli measurements. The values of fracture energy γ_s, which can be seen in Table 4.1, are similar to previous values reported from peel testing (Zhang *et al.*, 2005). In Fig. 4.7(b), the fracture energy γ_s for 2.5 % wt. cross-linking varies slightly with larger amounts of monomer. At 6 % wt. cross-linking the fracture energy settles to a cross-linking value of $\gamma_s \approx 3.6$ J m^{-2}. This is an extremely useful property of these gels for our hydraulic fracturing experiments, allowing us to change the Young's

Gel Concentration % w/v - % wt.	Young's Modulus E (kPa)	Stress Intensity K_I (Pa m$^{1/2}$)	Fracture Energy γ_s (J m^{-2})
8 - 2.5	64 ± 8	920 ± 54	4.8 ± 0.8
10 - 2.5	97 ± 9	1262 ± 72	5.6 ± 0.8
10 - 6	155 ± 10	1246 ± 34	3.6 ± 0.2
13 - 2.5	157 ± 3	1476 ± 112	5.2 ± 0.8
13 - 6	311 ± 7	1690 ± 154	3.4 ± 0.64
15 - 6	367 ± 20	1878 ± 130	3.6 ± 0.4

TABLE 4.1: Young's modulus, stress intensity and fracture energy measurements.

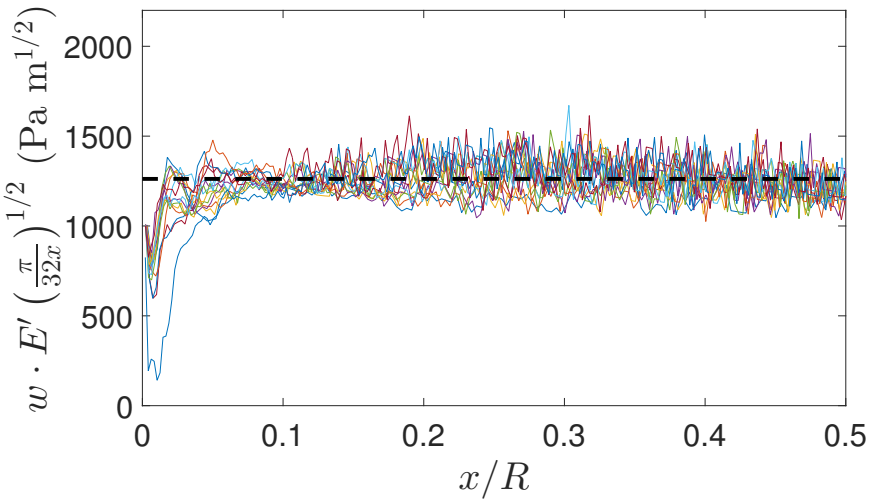

FIGURE 4.6: Fracture opening normalised by (2.37) versus distance from the crack tip x/R. Curves are plotted at 10 different time steps. The stress intensity factor K_I is given by the fit to the data denoted by the black dotted line. This fit was obtained from the average of values where x/R between 0.1 and 0.3.

modulus independent of fracture energy. It allows us to tune the characteristic time for transition (2.34) appropriately.

Moreover, this technique of determining fracture energy can become extremely useful when trying to characterise heterogeneous or layered gel systems.

4.4 Fracture surface

After fracturing occurs in these hydrogels, the crack surface is examined by peeling open the gel in the plane of fracture growth. The surface pattern generated by fluid-driven fracturing is clearly distinguishable from the rest of the surface by the light blue colour

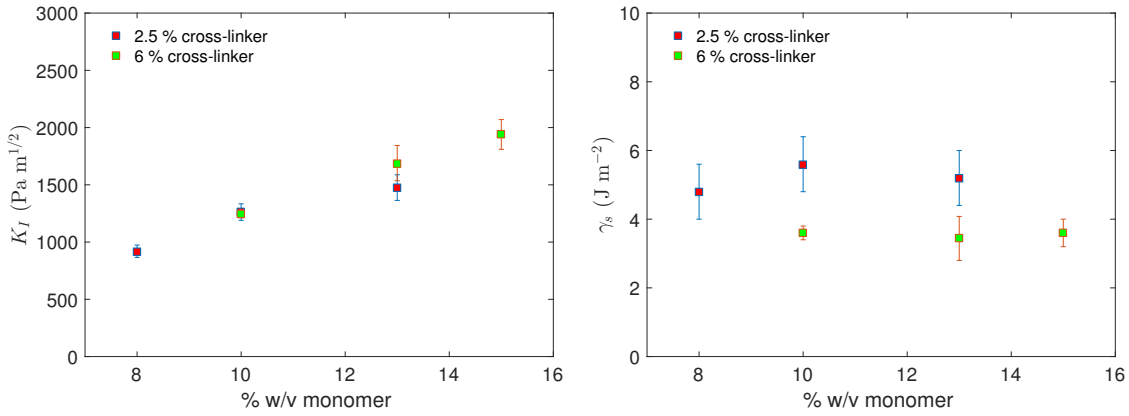

(a) Stress intensity (b) Fracture energy

FIGURE 4.7: (a) Stress intensity K_I versus % w/v monomer. (b) Fracture energy γ_s versus % w/v monomer. Both plots refer to gels with 2.5 and 6 % wt. cross-linking.

of the region, which occurs as a result of staining from the methylene blue in the fracturing fluid. Varying amounts of roughness are clearly evident on this surface (Figs. 4.8 and 4.9). These patterns are similar in shape to shear banding (or strain localization). A shear band is a narrow zone of plastic failure caused by intense strain on the material, and corresponds to a loss of homogeneity in the deformation of the material. This phenomenon is most often observed in ductile materials, but is also seen in quasi-brittle materials such as rock, ice and concrete.

However, our hydrogels are brittle materials and the two surfaces post-fracture are identical, suggesting that no plastic deformation of the gel matrix has occurred. The patterns evident on the crack surfaces are commonly referred to as 'step-lines' (Tanaka *et al.*, 1996). These steps-lines are small changes in height ($\mathcal{O}(10^{-1}$ mm)) and have been observed in hydrogels fractured in a peel-test configuration (Tanaka *et al.*, 2000, 1996). The step-lines are observed in two forms, orientated at an angle to the crack propagation direction and parallel to the direction of growth. Previously, these patterns have been labelled 'scale' and 'river' step-lines, respectively (Tanaka *et al.*, 1996). Wallner (1939) observed similar step-lines on the crack surfaces of glass. These Wallner lines are explained by proposing that they are the intersections of the paths between the moving crack front and the stress pulses. This mechanism is inadequate for the explanation in these experiments, as the fracture velocity is of order $\mathcal{O}(10^{-2}$ m/s), while the sound velocity is of the order $\mathcal{O}(10^{0}$ m/s); meaning the intersections would be near the crack tip and approximately perpendicular to the propagation direction.

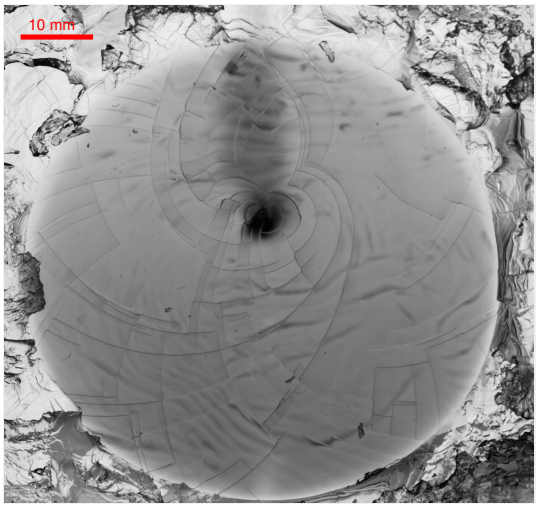

(a) 8 - 2.5%

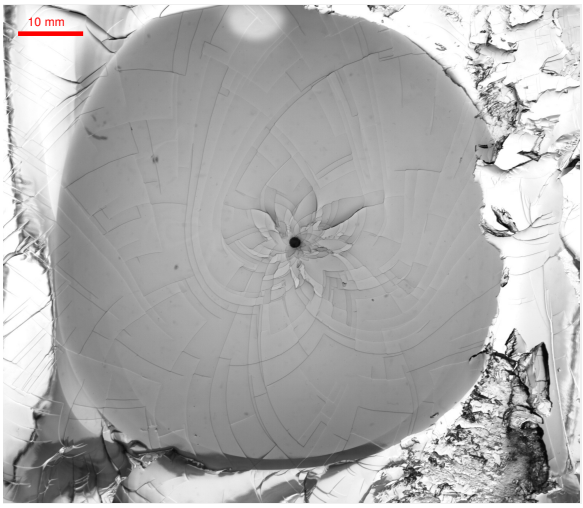

(b) 15 - 2.5%

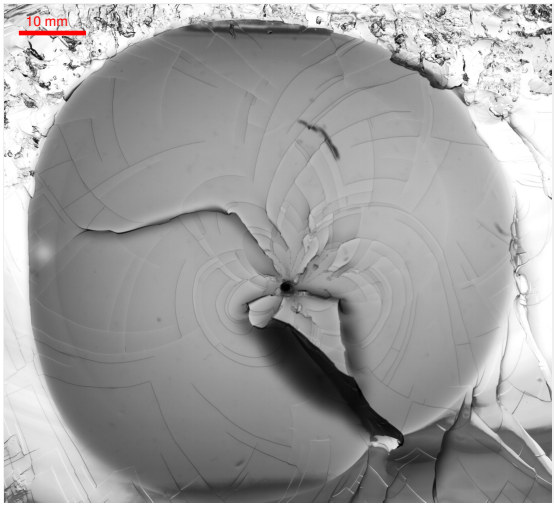

(c) 13 - 1.9%

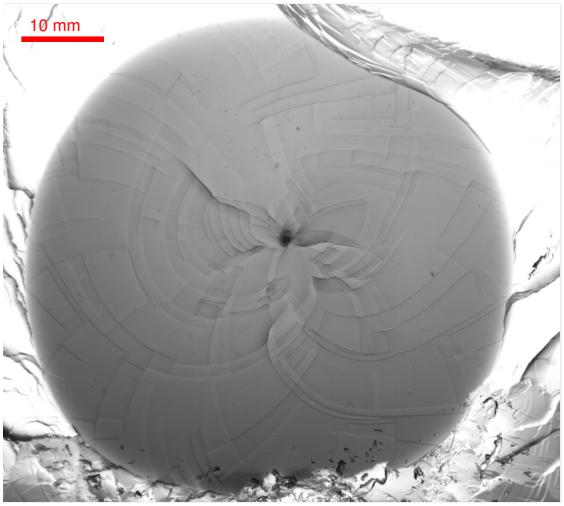

(d) 13 - 2.5%

FIGURE 4.8: Step-line pattern as a result of hydraulic radial fracture in gels with cross-linking between $1.9 - 2.5\%$.

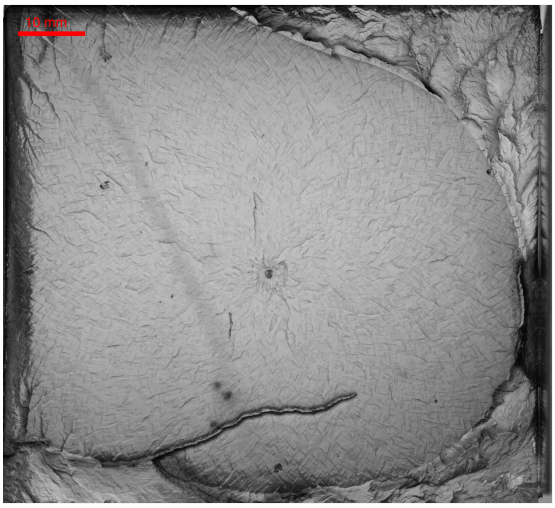

(a) 13 - 6%

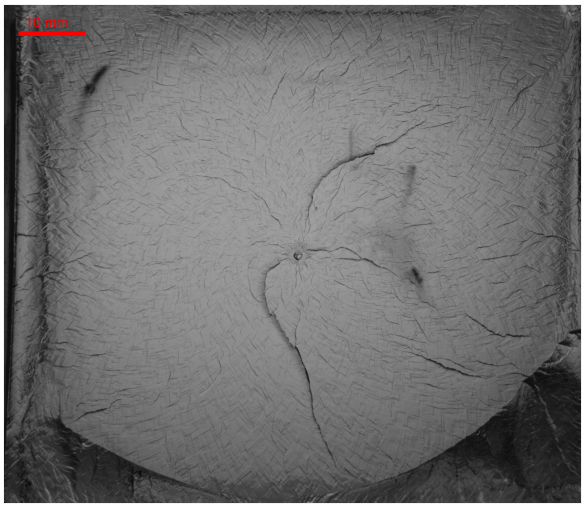

(b) 13.3 - 6%

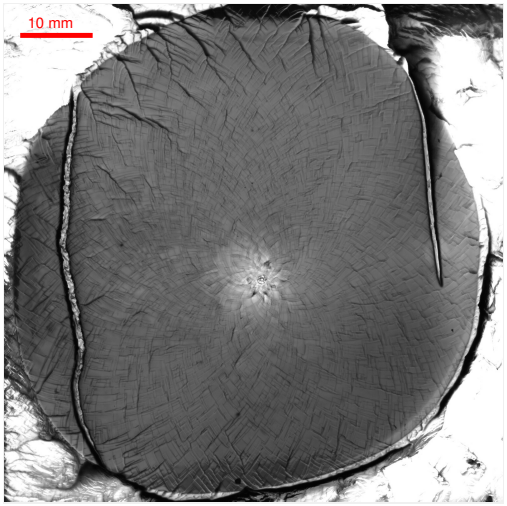

(c) 15 - 6%

FIGURE 4.9: Step-line pattern as a result of hydraulic radial fracture in highly cross-linked gels (6%).

In Figs. 4.8 and 4.9 examples of scale step-line patterns post-fracture can be observed. These patterns are created as small areas of the crack tip are aligned towards the fracture propagation direction. The behaviour of these sections is similar to a mode III tearing crack (Fig. 2.1(c)). It has been suggested that, in the scale case, these regions propagate at an angle of $\pi/4$ to the propagation direction and in a river pattern they propagate parallel to the propagation direction (Tanaka *et al.*, 1996). The observation of these scale and river step-lines have been found to be dependent on the velocity at which the fracture propagates. As the velocity of the fracture increases the pattern transitions from a scale to river step-line morphology.

As mentioned this pattern formation is very similar to shear banding, which has been shown to depend upon the dimensionless parameter (Poliakov *et al.*, 1994)

$$B = \frac{p_c c}{G V_{bc}}, \tag{4.5}$$

where p_c is the confining pressure, c is the velocity of sound in the material, G is the shear modulus (or Lamé constant) and V_{bc} is the velocity of the boundary or crack tip. With increasing B the shear bands are located further apart. A common explanation for this is that as a shear band forms, the stress inside the band decreases because of elastic unloading. Outside the shear band the pressure increases, suppressing another band formation in close proximity. The pressure difference then travels through the material at the speed of sound. Therefore, when B is large the banding pattern will occur on a larger scale. On the other hand, when B is small, the sound velocity is smaller compared to the loading rate of the crack, and the bands are located closer together in order to release the strain.

Therefore, we know an inverse relationship between spacing and velocity exists in the shear banding case. This relation is also observed for our brittle step-lines. The spacing between patterns increases as the crack tip velocity decreases. This is seen in Fig. 4.8, as the nucleation of these mode III regions is less evident away from the injection source. In fluid-driven fractures the crack velocity is decreasing as it propagates radially outwards, and thus, any patterns observed further away from this source materialised at a lower velocity. We can analyse the spacing between patterns by constructing a series of concentric circles with increasing radii around the point of initiation. We then count the number of patterns that touch this circle and divide by $2\pi r$, the circumference, to calculate the average spacing between patterns. Plotting this spacing against the radius from the injection point in Fig. 4.10(a) quantifies the qualitative observation that the spacing between patterns increases with distance from

the centre. In addition, from Fig. 4.10(b) it is clear that the spacing of the patterns is inversely proportional to the velocity of the fracture tip V. For highly cross-linked gels the relationship is less evident due to insufficient resolution of the images.

The formation of these mode III-like zones in our material could be caused by local material inhomogeneities that would cause the crack front to break into numerous sections, which propagate at different heights. This may also be due to blunting of the crack tip due to the stresses involved and the existence of small cavities in front of the crack tip. The tensile stress can lead to coalescence of the crack tip and cavities, which may cause the creation of these step-line discontinuities. At lower velocities this softening and cavitation may take longer to occur due to the crack loading and, thus, result in fewer discontinuities. Similar corrugations have been observed in other brittle materials such as brittle metallic glasses (BMGs) and glassy polymers (Narayan *et al.*, 2014; Sharon *et al.*, 2002; Xi *et al.*, 2006).

As mentioned before, the spacing between patterns has an inverse relation to fracture velocity. The fracture spacing also depends on the material properties of the gel such as monomer and cross-linking percentage, which is clear from Figs. 4.8 and 4.9. It is expected that the sound velocity of the material increases with increasing cross-linking due to the larger number of bonds present. Thus, more chains on the fracture surface must be broken in order for the crack to propagate. This higher cross-link density explains why more patterns are seen on the fracture surface in Fig. 4.9, as any softening of the crack tip and cavitation will occur on a much smaller scale, meaning step-lines are located closer together.

If we consider the radial geometry of our fracture and take into account that previous studies have found that these patterns occur at angles of $\pm\pi/4$ to the direction of propagation (Tanaka *et al.*, 2000), we can theoretically predict the shape they will take. Logarithmic spirals pitched at $\pi/4$ capture this behaviour, as seen in Fig. 4.11. This pattern is extremely similar to those observed in ductile systems through indentation (Antoniou *et al.*, 2007; Jeong *et al.*, 1994).

Considering Fig. 4.12, we measure the angles between step-lines of a specific $15 - 2.5\%$ gel post hydraulic fracture. In this example the angles are consistently less than $\sim 90^\circ$ and vary from $\sim 80 - 90^\circ$.

4.4.1 Fractal analysis

A fractal is a pattern that exhibits a similar pattern at different scales. Beautiful fractal patterns are seen to originate from the distribution of the crack surface markings in

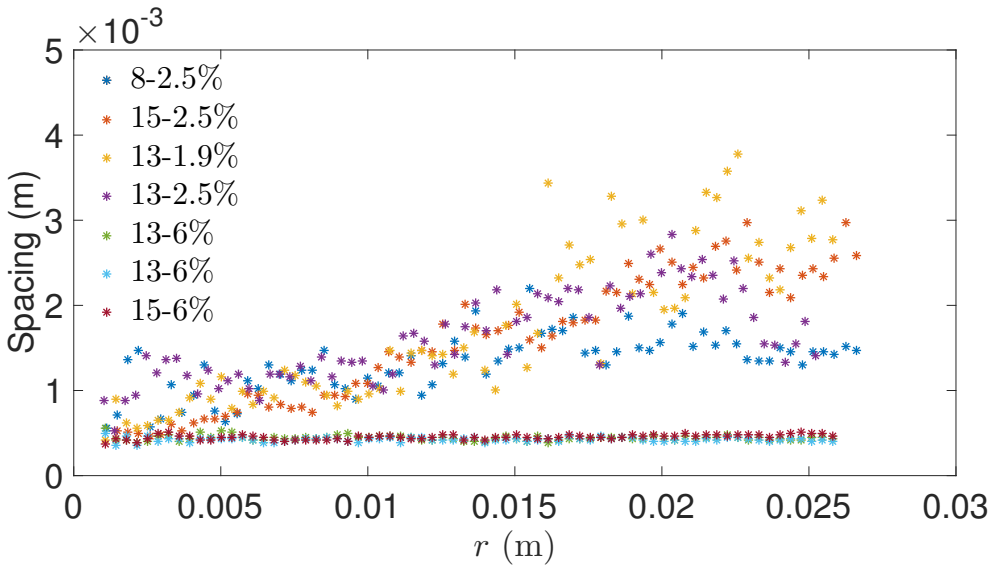

(a)

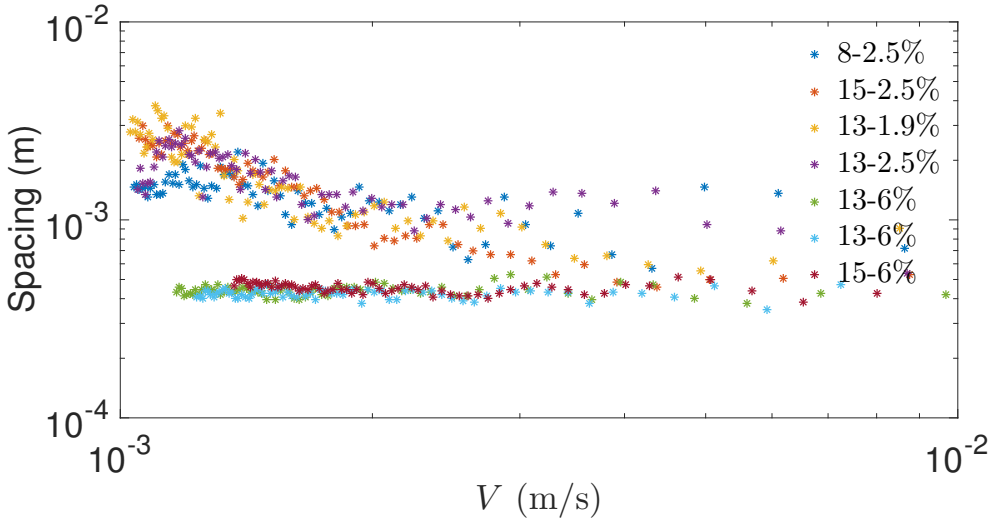

(b)

FIGURE 4.10: (a) Fracture surface pattern spacing versus radius. (b) Pattern spacing versus fracture tip velocity.

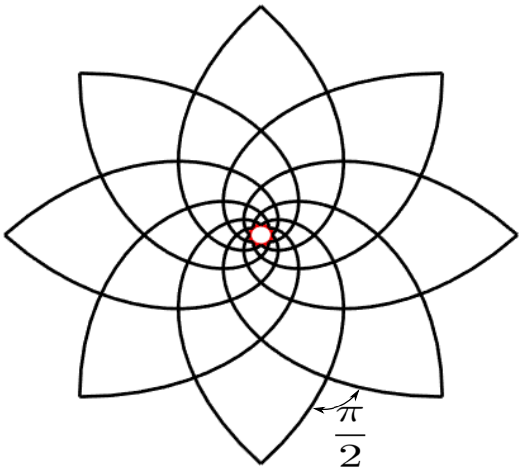

FIGURE 4.11: Theoretical prediction of step-line patterns around a circular indentation with logarithmic spirals pitched at an angle of $\pi/4$.

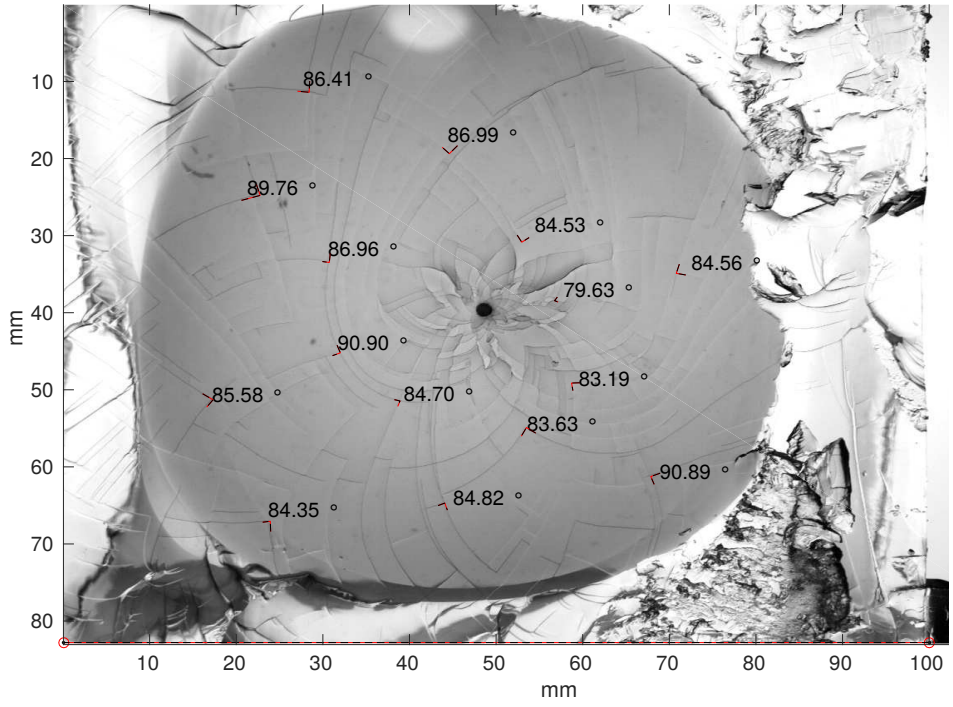

FIGURE 4.12: Measurement of the angles between emanating step-lines.

our experiments. Observing the patterns in Figs. 4.8 and 4.9, it is evident that these patterns created by the step-lines meeting at approximately 90° angels to each other, occur at various length scales throughout the fracture surface. The fractal dimensions of these patterns were computed using the classical box-counting technique (Matlab Boxcount, F. Moisy (2009)) (Sarkar & Chaudhuri, 1994). The fractal dimension can be thought of as quantifying how detail in a pattern changes with scale.

If we denote C as the two dimensional image, n is the number of boxes of side length b that are needed to cover the non-zero elements of C. If C is a fractal set with fractal dimension $D_f < D = 2$, where D is the dimension, then n scales like

$$n \propto b^{-D_f}, \tag{4.6}$$

where D_f is also known as the box-counting or Minkowski-Bouligand dimension. By plotting the local slope $D_f = -\mathrm{d}\ln n/\mathrm{d}\ln b$ versus b, we can observe when D_f is a constant over a range of b. If this is the case, then this constant D_f is the fractal dimension of C.

During the analysis, a computer generated mask was created around the radial fracture, so that only the surface patterns in this area are considered. The results of the fractal analysis can be seen in Fig. 4.13. It is clear from this graph that gels with a cross-linking of $1.9-2.5\%$ and those with cross-linking $\sim 6\%$ follow two different curves, in relation to the fractal dimension at specific box sizes. The $1.9-2.5\%$ and 6% gels have approximately constant fractal dimensions in the ranges $1.3\times10^{-3} \leq b \leq 1.1\times10^{-2}$ and $3.4\times10^{-4} \leq b \leq 2.7\times10^{-3}$, respectively. Thus the fractal dimensions are averages of D_f values in these ranges, which gives $D_f \approx 1.7\pm0.14$ and 1.92 ± 0.08 for $1.9-2.5\%$ and $\sim 6\%$ cross-linking, respectively. The fractal dimension for 6% cross-linking is similar to that of the theoretical logarithmic spirals in Fig. 4.11, which have a fractal dimension of $D_f \approx 1.97\pm0.04$.

Interestingly, the range of these fractal values is consistent with those observed in the literature for plastic shear bands (Poliakov *et al.*, 1994). It has also been observed that the fractal dimension depends on the dimensionless parameter B in (4.5). The fractal dimension D_f is consistently larger in systems with lower B values. This is observed in our experiments, if we assume the confining pressure and ratio of sound to boundary velocity to be constant for each gel. Hydrogels with higher percentages of monomer and cross-linking have a larger elastic modulus, and therefore a smaller B and larger fractal dimension.

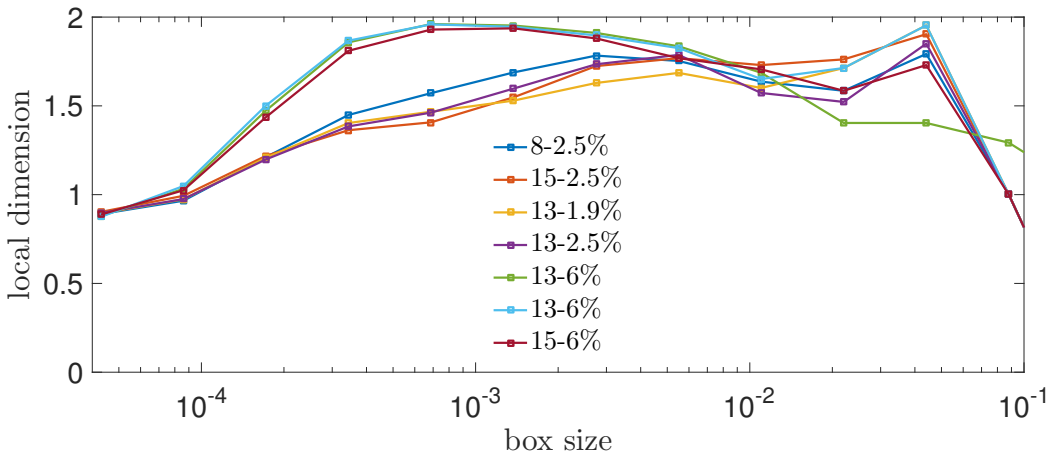

FIGURE 4.13: The fractal dimension analysis using the box-counting method for varying gel concentrations.

4.5 Conclusions

Polyacrylamide hydrogels were synthesized to study fluid-driven fractures in an impermeable elastic medium. These gels allow detailed measurements of the radial extent and full-field thickness of a fracture, as well as the fracture energy of the particular gel configuration. The transparent gels permit hydraulic fracturing experiments with a significant range of Young's modulus and fracture energy values. The sufficiently wide range of experimental parameters ensures both toughness and viscosity limiting regimes can be characterised fully in the context of dynamic hydraulic fracturing (O'Keeffe *et al.*, 2018).

This approach to studying hydraulic fracturing also gives rise to crack surface deformation patterns, which have been observed in fractured rock formations. The spacing between these phenomena is seen to depend heavily on the chemical configuration of the specific gel matrix, as well as the fracture velocity. These step-line patterns appear to occur due to minuscule inhomogeneities within the gel and/or small areas of the crack tip experiencing mode III loading due to crack tip softening and cavitation, which mimics the effects seen in ductile materials.

The calculation of fractal dimension values for the step-line patterns is easily obtainable, which will allow comparisons with geological field observations. This chapter demonstrates how these gels can be made, their physical properties obtained and their suitability to further explore fracturing phenomena in great detail.

Chapter 5

Experimental results of a radial fluid-driven fracture

5.1 Introduction

In this chapter, we present the results of an experimental exploration of a radial crack driven by an incompressible Newtonian fluid, injected at a constant rate into an elastic matrix. We set out to verify the time-dependent radial and aperture fracture scalings outlined in Chapter 2, using the experimental setup and techniques detailed in Chapter 3. We will also analyse the time-dependent crack tip behaviour of these fractures to further characterise the two dominant regimes, toughness or viscosity, and the transition between them. Finally, we will report on the internal fluid flow within these fractures and the differences in the flow structure, dependent on the regime of propagation. Most of the information contained in this chapter has been published in O'Keeffe *et al.* (2018).

5.2 Radial crack growth

Once fluid is injected at a constant flux, a fracture propagates radially outwards from the source, with no observable lag between the fluid-filled region and the crack tip, as expected from § 2.4. We can see two examples of this type of fracture in Fig. 5.1. Initially, there is a small fast fracture burst when the crack is first formed, due to the release of elastic energy stored in the matrix. After this initial crack is created, the fracture then propagates in the appropriate regime. Generally, toughness-dominated

Exp No.	Fluid	E' (kPa)	μ (Pa·s)	Q (mL/min)	γ_s (J m^{-2})	t_{mk} (s)
exp1	glycerin	165	0.1	15	4.4	5×10^{-7}
exp2	glycerin	129	0.1	20	5.6	2×10^{-7}
exp3	glycerin	209	0.28	20	5.2	5×10^{-6}
exp4	glycerin	200	0.08	35	5.6	1×10^{-7}
exp5	glycerin	207	0.08	10	3.6	6×10^{-8}
exp6	glycerin	129	0.08	10	5.6	6×10^{-8}
exp7	water	207	0.001	15	3.6	2×10^{-11}
exp8	glycerin	85	0.08	15	4.8	6×10^{-8}
exp9	glycerin	347	0.08	15	10.8	3×10^{-9}
exp10	glycerin	209	0.08	15	5.2	1×10^{-7}
exp11	silicone	427	1	2	3.6	2×10^{-4}
exp12	silicone	213	1	2	3.6	4×10^{-4}
exp13	glycerin	213	1.2	10	3.6	6×10^{-4}
exp14	glycerin	209	1.13	20	5.2	2×10^{-4}
exp15	glycerin	425	1.13	23	3.6	8×10^{-3}
exp16	glycerin	489	1.13	23	3.6	1×10^{-2}
exp17	syrup	415	3.4	23	3.6	1×10^{-1}
exp18	syrup	489	10	20	3.6	2×10^{0}
piv1	water	85	0.001	11	4.8	7×10^{-13}
piv2	water	129	0.001	20	5.6	2×10^{-12}
piv3	glycerin	415	1.13	23	3.6	8×10^{-3}
piv4	syrup	427	7	20	3.6	1×10^{0}

TABLE 5.1: Experiments conducted with particular values of physical parameters.

fractures were observed to propagate with slightly more asymmetry than fractures in the viscosity limiting regime, and this is discussed more thoroughly in § 5.6. Fig. 5.1 exhibits the typical raw experimental images obtained and the associated thickness measurements. The ridges seen are due to the injection tube and the apparatus used to hold the injection needle in place.

All of the experiments reported in this chapter can be found in Table 5.1, which contains the variable parameters and transition timescale t_{mk} for each experiment.

In Fig. 5.2(a), we plot the radial extent versus time for experiments in the toughness regime, where $t \gg t_{mk}$. These raw data show a linear progression on the log-log scale for late times. By rescaling the radius using (2.30) and time with the characteristic timescale (2.34), we produce Fig. 5.2(b). We observe that this scaling collapses all of the experimental curves onto a horizontal line, which obeys the $t^{2/5}$ power law, as expected for late times. The best fit line has a pre-factor $k = 0.83 \pm 0.07$, where

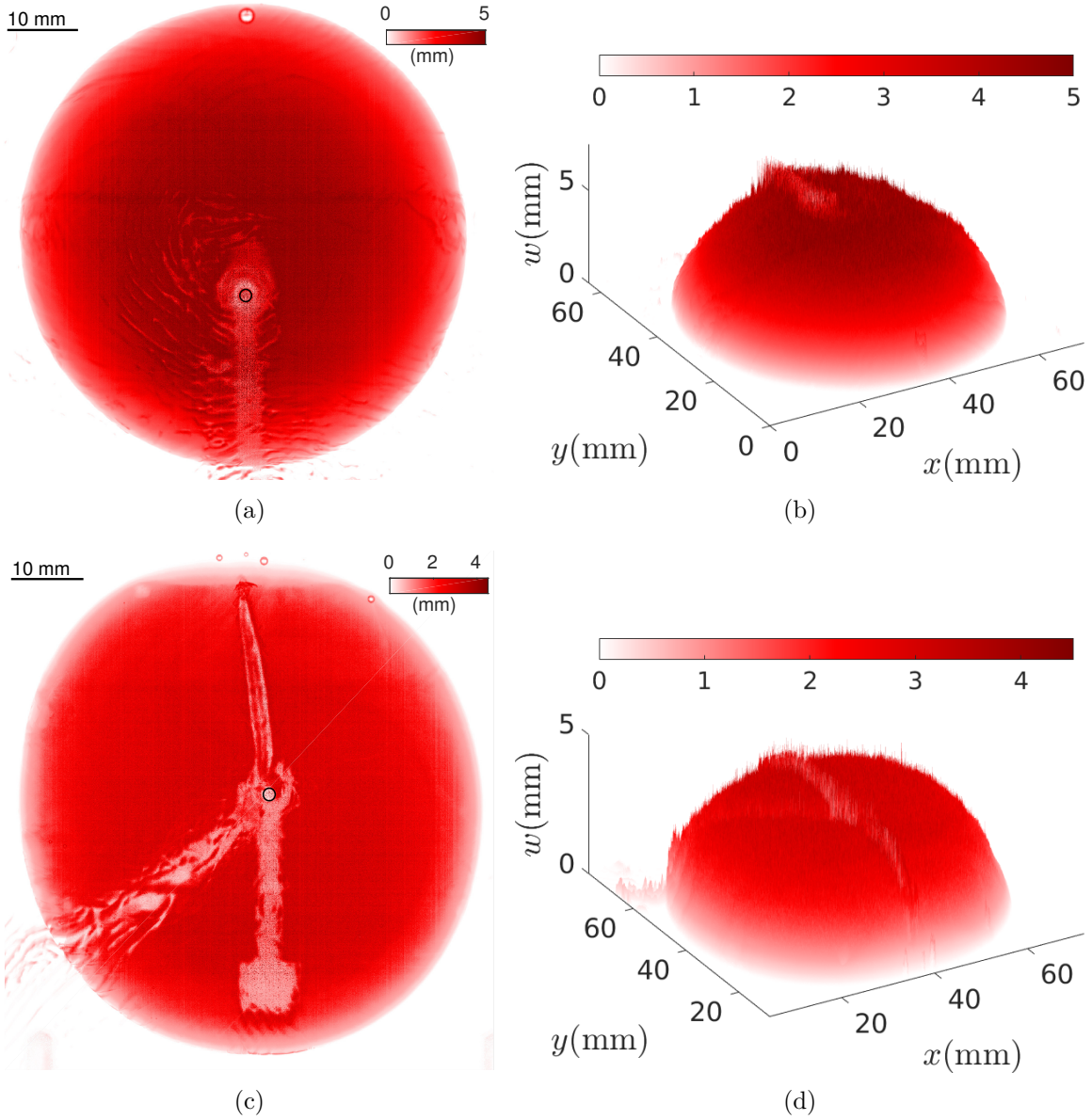

FIGURE 5.1: Experimental radial and aperture profiles of sample experiments (exp8($t \approx$ 39.4 s), Fig. 5.1(a) & Fig. 5.1(b)) and (exp15($t \approx 40.6$ s), Fig. 5.1(c) & Fig. 5.1(d)). (a) and (c) are raw images of radial extent with colour corresponding to aperture. (b) and (d) are processed images showing the radial extent and fracture aperture w in three dimensions.

$$R_k(t) = k\left(\frac{E'^2Q^2}{K'^2}\right)^{1/5} t^{2/5}. \tag{5.1}$$

This agrees well with the theoretical pre-factor, which has a value of 0.85 from Savitski & Detournay (2002). Also calculating a slope to the data on a log-log scale has the value 0.4 ± 0.04 which matches the time exponent of 2/5. We can compare this result to that of another experimental study using gelatin in Lai *et al.* (2016). On accounting for the different constants used in their scaling, the pre-factor in that study would correspond to a value of $k = 0.56$. This suggests that the polyacrylamide hydrogel performs well as a brittle solid, under the modelling assumptions made in Chapter 2.

Fig. 5.3(a) plots the crack radius R versus time for experiments in the viscous regime, in which $t \lesssim t_{mk}$. Once again, the raw data follow a power law, and using the radial viscosity-dominated scaling as in Table 2.1, the data collapse onto the same horizontal line (Fig. 5.3(b)). The best fit line has a pre-factor $m = 0.3 \pm 0.1$, where

$$R_m(t) = m\left(\frac{E'Q^3}{\mu'}\right)^{1/9} t^{4/9}. \tag{5.2}$$

The pre-factor m differs significantly in the viscous regime from the theoretical value of 0.7. However, calculating a slope to the data on a log-log scale has the value 0.46 ± 0.04 which matches the time exponent of 4/9. To account for this discrepancy we examined some possibilities:

(i) There may have been storage of fracturing fluid in the initial stages of the experiment, leading to a different value of Q from the expected one. This was explored using PIV measurements from § 5.5. The resulting flux estimates from the velocity data match the syringe pump values to within approximately 10%, suggesting that storage effects were negligible and Q was accurately reported.

(ii) The parameter values were not as prescribed. However, we believe that the experimental parameters are well characterised. Young's modulus E was calculated from two different methods (compression tests and spherical indentation) and the fluid viscosity μ was measured using a u-tube viscometer before every experiment. In order for our experimental viscous pre-factor to match the theoretical value of 0.7, the ratio of $E'Q^3/\mu$ would have to be significantly different as it is raised to a power of 1/9.

(iii) The viscosity regime does not start at time $t = 0$. This could be due to the initial elastic response of the hydrogel. However, estimates for the maximum value of this from $t_{om} = E'\mu'/\sigma_0^3 \approx 0.03$ s, are not sufficient to explain the difference (Bunger &

Detournay, 2007). We can fit the theoretical pre-factor to the data, where time is equal to $(t - t_{om})$, to find a suitable t_{om} after which the viscosity regime propagates. We find that the t_{om} value is in the range from $\approx 5 - 25$ s, which seems to be an implausibly long time.

This analysis suggests that there may be some unidentified physical mechanisms that were unaccounted for in the modelling, and that are responsible for this experimental underprediction. A similar discrepancy can be found in the study by Lai *et al.* (2015), where their scaling argument has an extra constant $(1/32\pi^3)^{1/9}$, when compared with (5.2). The rescaled data in that study has a pre-factor of 0.62, which would correspond to a value of m = 0.29 here using (5.2). Therefore, both their and our independent experimental studies exhibit similar underpredictions.

To distinguish between regimes, we plot all experiments scaled with the toughness-dominated radial power law (2.30) in Fig. 5.4. The dashed line is fitted to experiments where $t/t_{mk} \lesssim 10^2$, and the solid line is fitted to experiments where $t/t_{mk} \gtrsim 10^2$. The difference in fits between the two groups of experiments shows that it is possible to distinguish between the two different regimes. One particular experiment, exp16, is known to transition from a viscous to toughness-dominated regime, and will be discussed in detail in § 5.4. Moreover, in Fig. 5.5 all experiments are plotted using the non-dimensional expressions for radius and time (2.33). This plot shows the full range explored by the experiments and the collapse of the data. However, once again it is difficult to distinguish between regimes for this plot due to the similarities in crack growth rate for both viscous and toughness regimes.

Viscous experiments where $t/t_{mk} < 10^{-1}$ were difficult to obtain due to the syringe pump stalling when trying to force extremely viscous liquids to high flux rates. This was mainly caused by the plastic syringe deforming and spring loading under the high force exerted on it.

5.3 Crack aperture

The crack aperture measurements obtained from dye attenuation provide us with the full crack profile. In Figs. 5.6 and 5.7, we plot the cross section, which intersects the injection needle so we can properly analyse the crack aperture scalings. The anomalous points observed in the data for both experiments, which occur around $R = 0$, are due to the presence of the injection needle blocking measurements from being taken at this point.

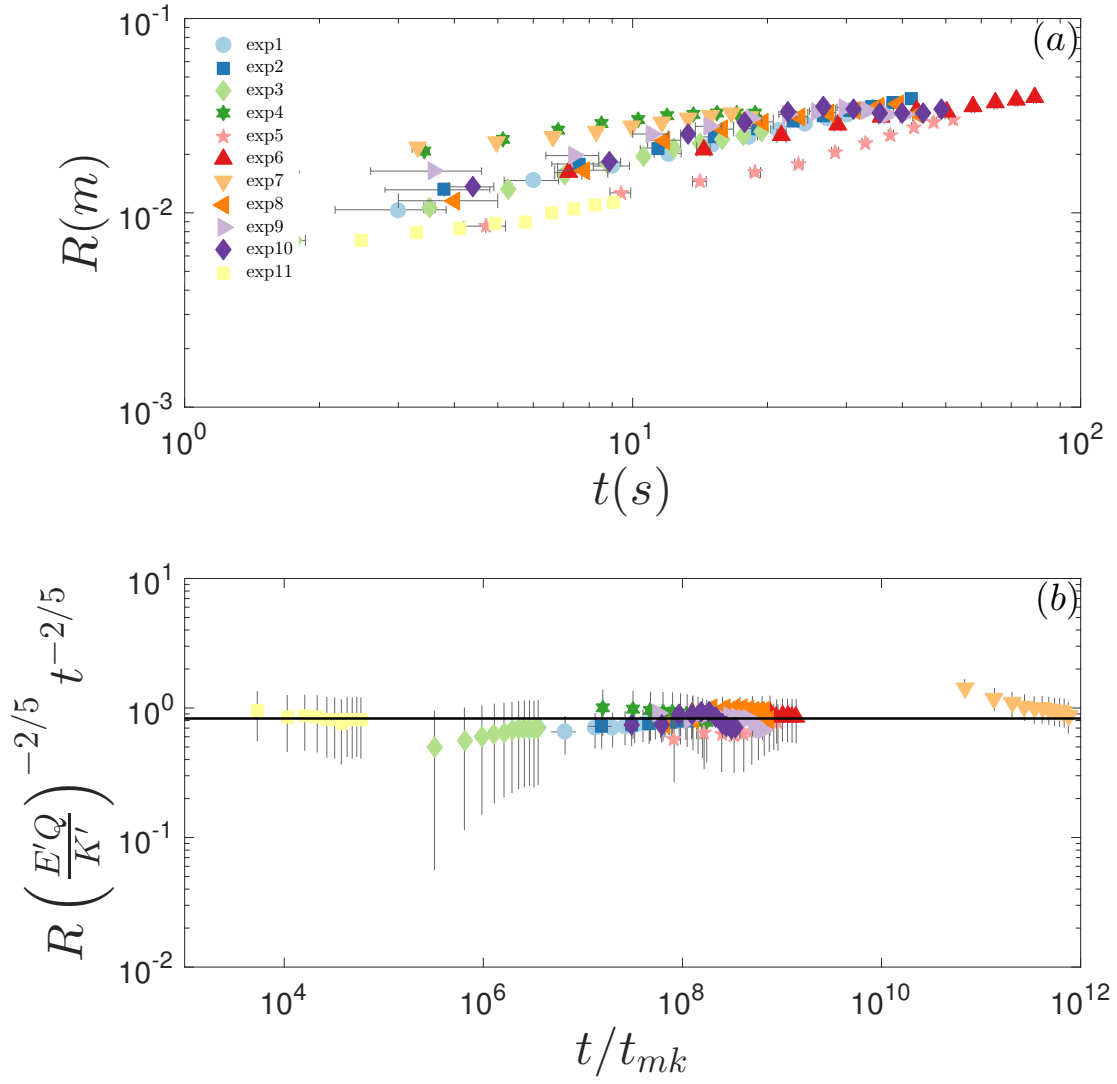

FIGURE 5.2: (a) The growing crack radius R versus time for a number of experiments with varying injection rate Q, viscosity μ and elastic modulus E. (b) The toughness rescaling $R_k(t)$ of crack dependence versus rescaled time t/t_{mk}. The solid line represents the best fit to the data.

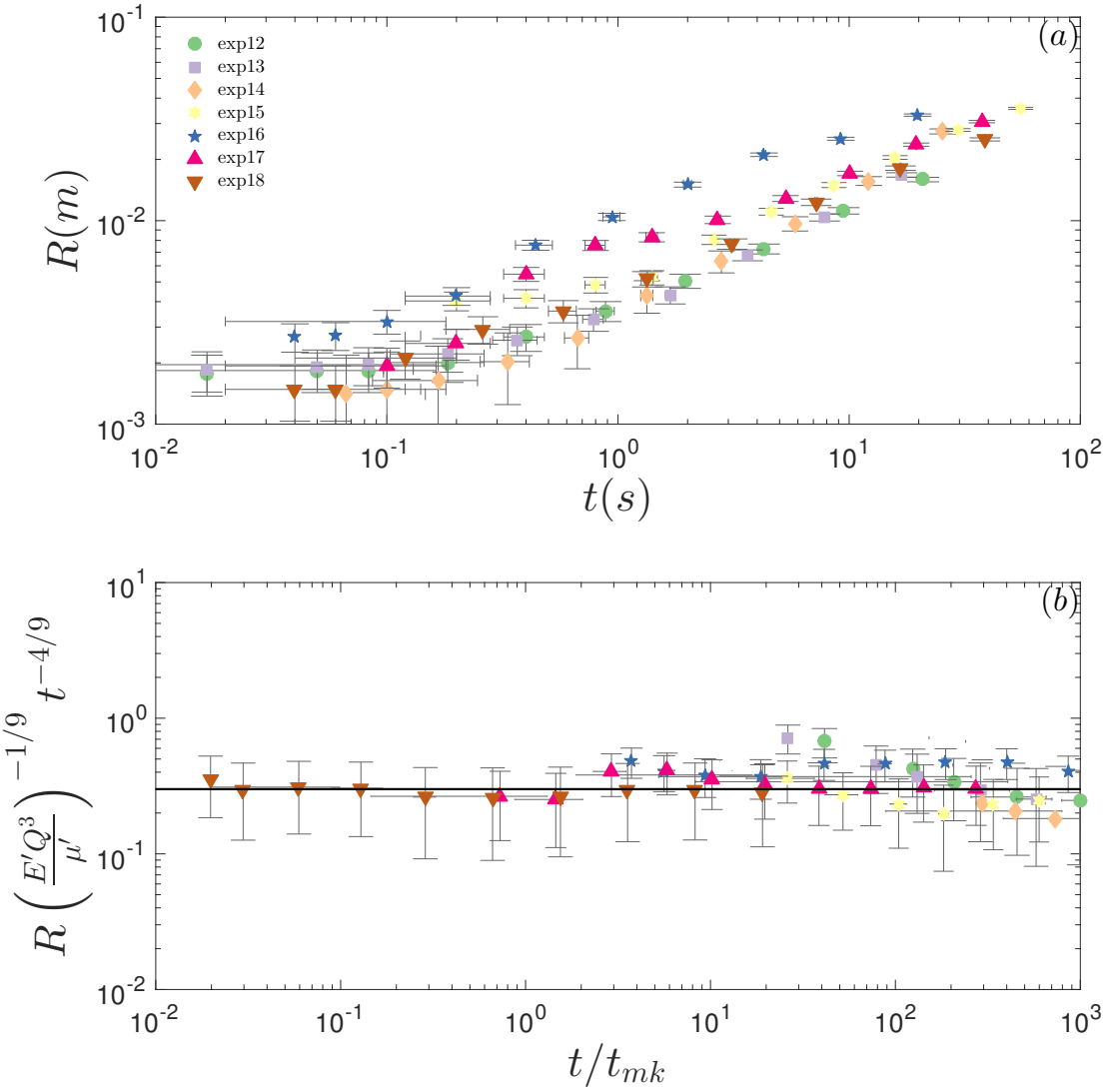

FIGURE 5.3: (a) The growing crack radius R versus time for a number of experiments with varying injection rate Q, viscosity μ and elastic modulus E. (b) The viscosity rescaling $R_m(t)$ of crack dependence versus rescaled time t/t_{mk}. The solid line represents the best fit to the data.

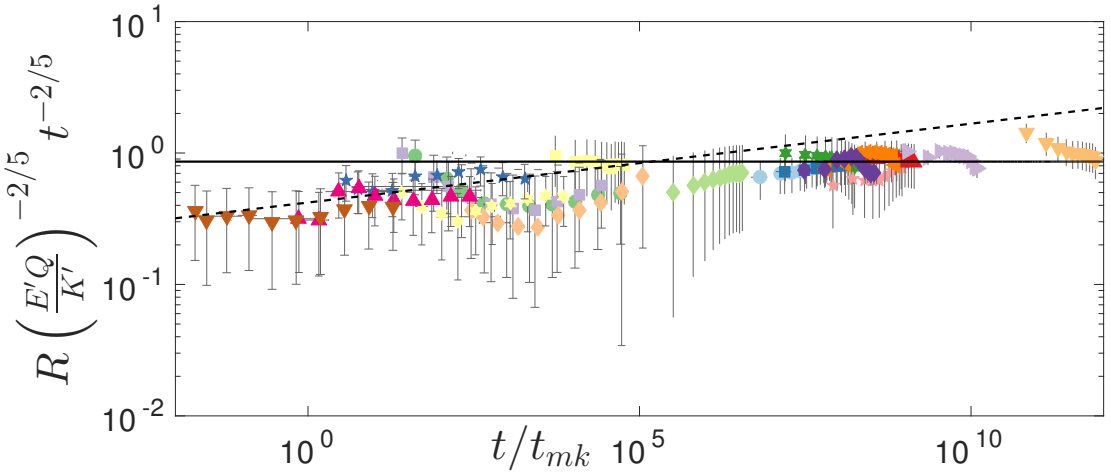

FIGURE 5.4: All experiments scaled using the radial toughness-dominated power law (2.30). The solid and dashed lines represent the best fits to the toughness and viscosity data, respectively.

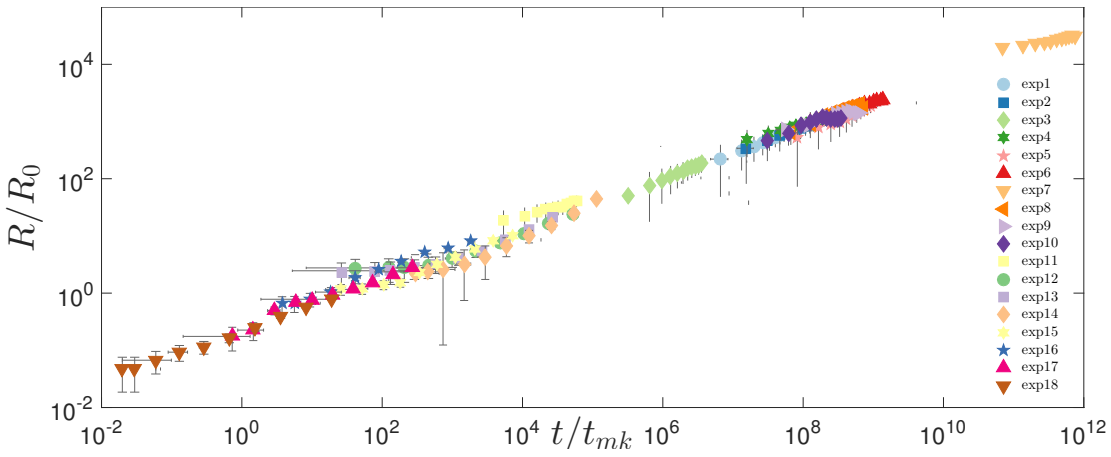

FIGURE 5.5: All experiments scaled using the non-dimensional radial and time expressions (2.33).

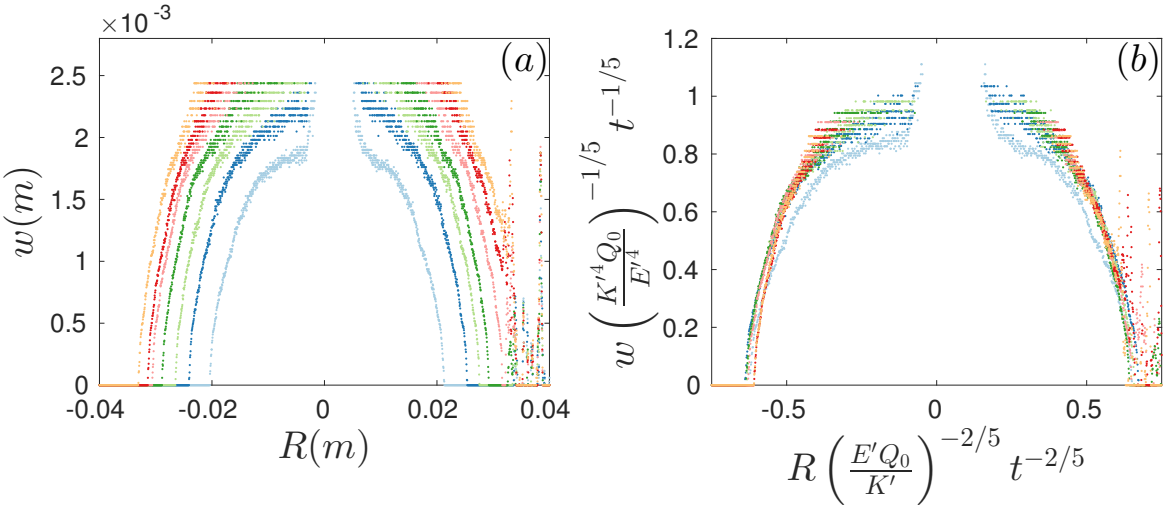

FIGURE 5.6: (a) The crack aperture profile of a cross section intersecting the injection needle of the radial fracture, for experiment exp9 (Table 5.1). Each set of coloured data points corresponds to the crack aperture at a certain time, with time evolving outwards in increments of $\Delta t = 4$ s from the crack centre for each curve. (b) The rescaled fracture aperture profile using the toughness-dominated radial and width power law scalings from Table 2.1.

In Fig. 5.6(a), the width versus radius is plotted for a fracture in the toughness-dominated regime. Each coloured curve corresponds to the crack aperture at a certain time, with the curves at the outer edges corresponding to the later times. Fig. 5.6(b) shows that scaling the cross section data, with the radial and width toughness power laws from Table 2.1, results in collapse of the curves.

Results from an experiment near the viscosity regime are shown in Fig. 5.7. Once again, the curves collapse under the appropriate scalings onto a single curve, as seen in Fig. 5.7(b), thus behaving in the expected way as outlined in Table 2.1. Although Figs. 5.6 and 5.7 only correspond to two particular experiments (exp9 & exp15), this behaviour can be reproduced by other experiments. The scaled data produces a very well-behaved radius collapse, while the error at large heights of the fractures are related to the tuning of the calibration to capture the tip behaviour.

5.4 Crack tip behaviour

These aperture measurements additionally allow us to explore the tip behaviour of these fractures. This method provides an extra validation of the toughness and viscosity regimes, while also allowing us to observe the transition between regimes. Fig. 5.8 shows

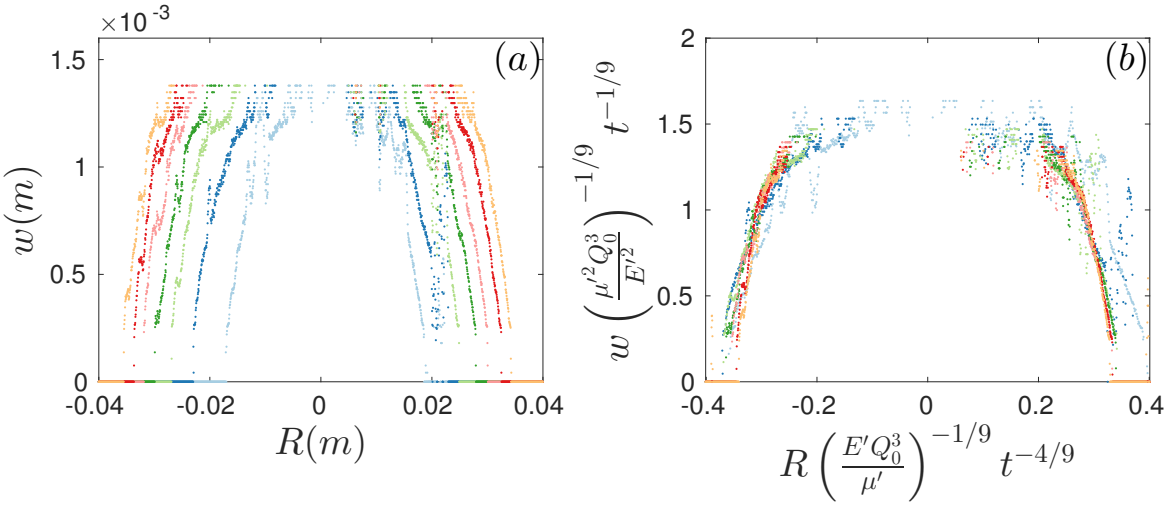

FIGURE 5.7: (a) The crack aperture profile of a cross section intersecting the injection needle of the radial fracture, for experiment exp16 (Table 5.1), with $\Delta t = 4$ s. (b) The rescaled fracture aperture profile using the viscosity-dominated radial and width power law scalings from Table 2.1.

the crack tip opening profile for a fracture propagating in the toughness-dominated regime compared with the asymptotic forms for the toughness and viscous regimes, (2.37) and (2.38) respectively. It is clearly seen that the LEFM asymptotic behaviour in (2.37) is observed for different times throughout the experiment.

Fig. 5.9 shows the transition from the viscous to toughness-dominated asymptote. Fig. 5.9(a) shows that the tip region is governed by the viscous intermediate asymptote (2.38) when the fracture is transitioning between regimes at $t = 0.76$ s. As the fracture evolves, the crack tip then transitions fully into the toughness-dominated regime at later times. Fig. 5.9(b) shows the crack shape in this regime.

5.5 Fracture fluid flow

In modelling the radial fracture problem, we have assumed (see (2.7)) that lubrication theory adequately captures the physical mechanisms of the flow; meaning that the flow is laminar and radial in nature. The appropriate Reynolds number for the lubrication fluid flow in the fracture is defined in (2.6).

If we first consider an example of a fracture near the viscosity-dominated regime (piv3, Table 5.1), where $Q \approx 23$ ml/min, $\mu \approx 1130$ mPa·s, $E \approx 311$ kPa, $\gamma_s \approx 3.6$ J/m^2, $\rho \approx 1.26$ g/cm^3, $w \approx 1.7$ mm and $R \approx 25$ mm, then $Re_m \approx 1.9 \times 10^{-4}$ ($t_{mk} \sim 0.008$ s). In a toughness limiting regime (piv2, Table 5.1), where $\mu \approx 1$ mPa·s, $E = 97$ kPa,

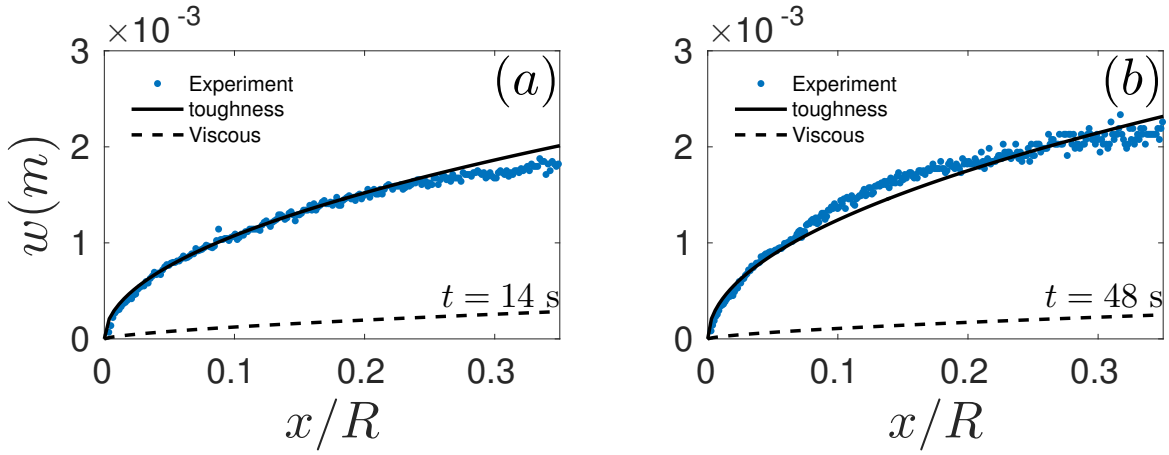

FIGURE 5.8: The crack tip region for a toughness-dominated fracture (exp10), which follows the LEFM toughness asymptote (2.37) denoted by the solid line. (a) $t/t_{mk} = 1.4 \times 10^8$ and (b) $t/t_{mk} = 4.8 \times 10^8$.

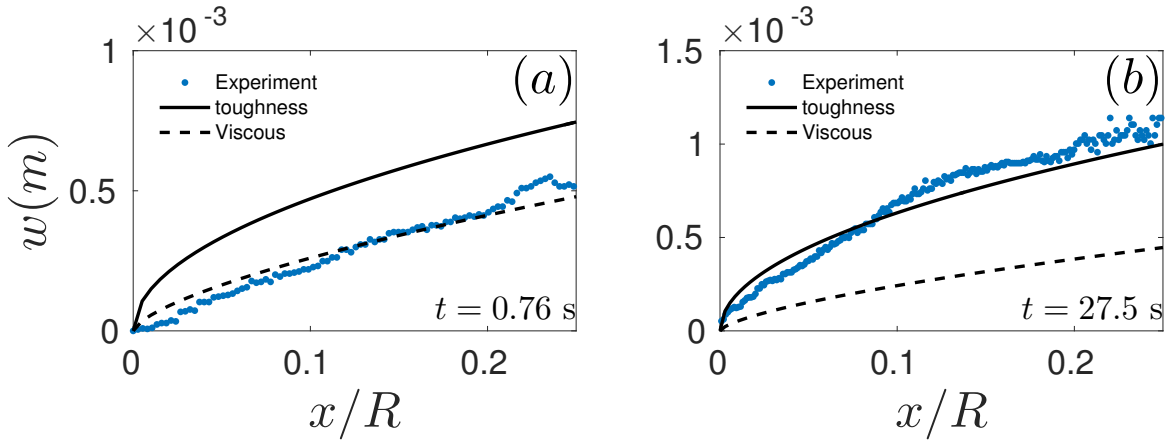

FIGURE 5.9: The crack tip region for a fracture (exp16), which transitions from the viscous dissipation (2.38) to the toughness asymptote (2.37) denoted by the dashed and solid lines, respectively. (a) $t/t_{mk} = 76$ and (b) $t/t_{mk} = 2.8 \times 10^3$. Even though the fracture is transitioning between regimes in (a), viscous behaviour is still exhibited in the crack tip shape.

$Q = 20$ mL/min, $\gamma_s = 5.6$ J/m^2, $\rho \approx 1$ g/cm^3, $w \approx 2$ mm and $R \approx 25$ mm, then $Re_k \approx 1.7 \times 10^{-1}$ ($t_{mk} \sim 10^{-12}$ s). This approximation suggests that the range of Reynolds numbers involved is sufficiently small to the extent that inertial effects can be neglected.

Examples of the velocity field in the viscosity regime (piv4, Table 5.1) obtained from the PIV measurements are shown in Fig. 5.10. The velocity fields exhibit laminar radial flow emanating from the injection needle source in the centre of the fracture. The magnitude of the velocity vectors diminishes with distance from the source, which is consistent with a constant volume flux spreading radially outwards. Due to the constant volume flux into the fracture, the quantity $2\pi u_r r w$ is conserved. Therefore, if the fracture is propagating in the viscosity limiting regime, $u_r \propto r^{-5/3}$. This is observed in Fig. 5.11, where the azimuthal by-averaged radial velocity is plotted versus the normalised distance from the source for the two times seen in Fig. 5.10. The dip at the end of the experimental curves is due to fluid reaching the fracture tip and a lack of particles in this newly created region to accurately measure the velocity. It is expected that there might be an increase in velocity just before the fracture tip due to the minuscule aperture at this point, but this was unable to be determined because of resolution at this point as mentioned above.

The velocity fields in an experiment that transitions from a viscosity to toughness-dominated fracture regime (piv3, Table 5.1), are shown in Fig. 5.12. In Fig. 5.12(a), the velocity field at early times when $t/t_{mk} \sim 10^2$ is similar to that observed in the viscosity regime, as anticipated. However, at later times in the experiment (Figs. 5.12(b) and 5.12(c)), when the fracture has transitioned fully into the toughness regime, the fracturing fluid noticeably circulates around the fracture once it has reached the tip. Two small circulations form at the top of the fracture and grow in size as the crack propagates radially, until they finally encompass the whole fluid-filled fracture.

For experiments that are toughness-dominated at all times, the flow within the fracture can be very disordered. Fig. 5.13 shows the average velocity fields for two such experiments at late times. Similarly to the late-time behaviour of the transitioning fracture, the structure of the flow appears to be split into circulation cells within the fracture, which are quite different from the assumed flow field under lubrication theory. The number of cells that formed also appears to vary between experiments. So far, we have observed a variation between 1 and 4 for the number of cells present in a single fracture.

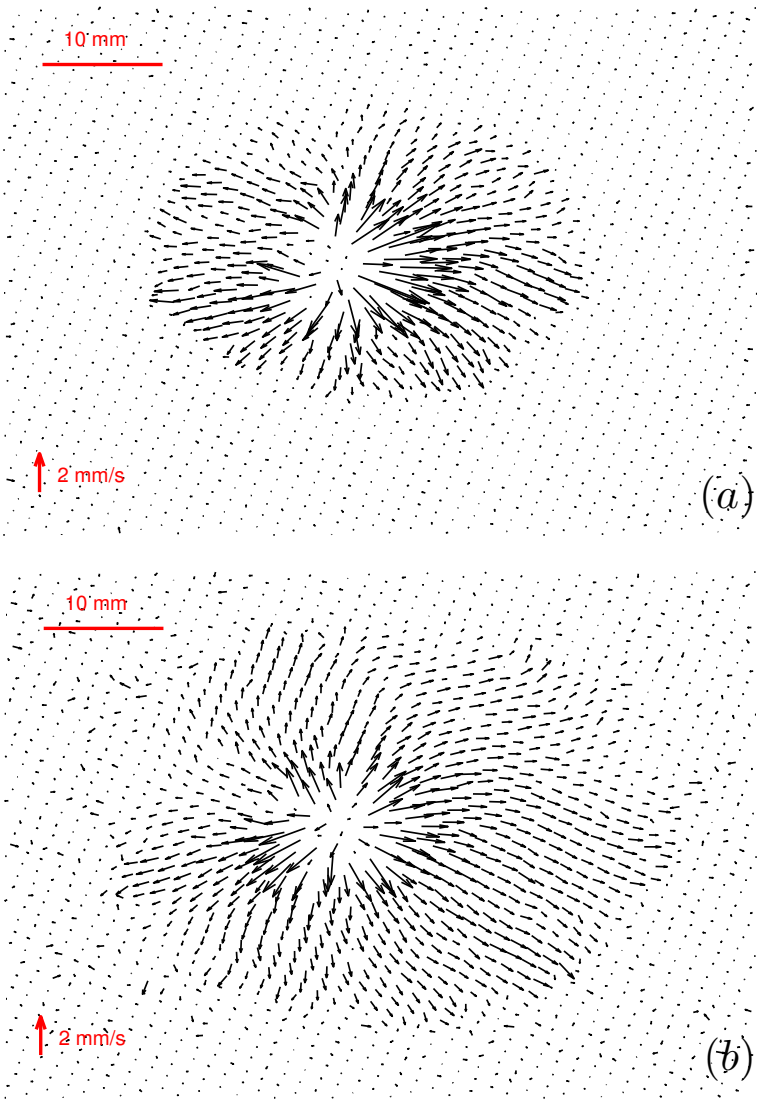

FIGURE 5.10: Velocity fields for a fracture in the viscosity regime (piv4). (a) $t/t_{mk} \sim 10$ and (b) $t/t_{mk} \sim 20$.

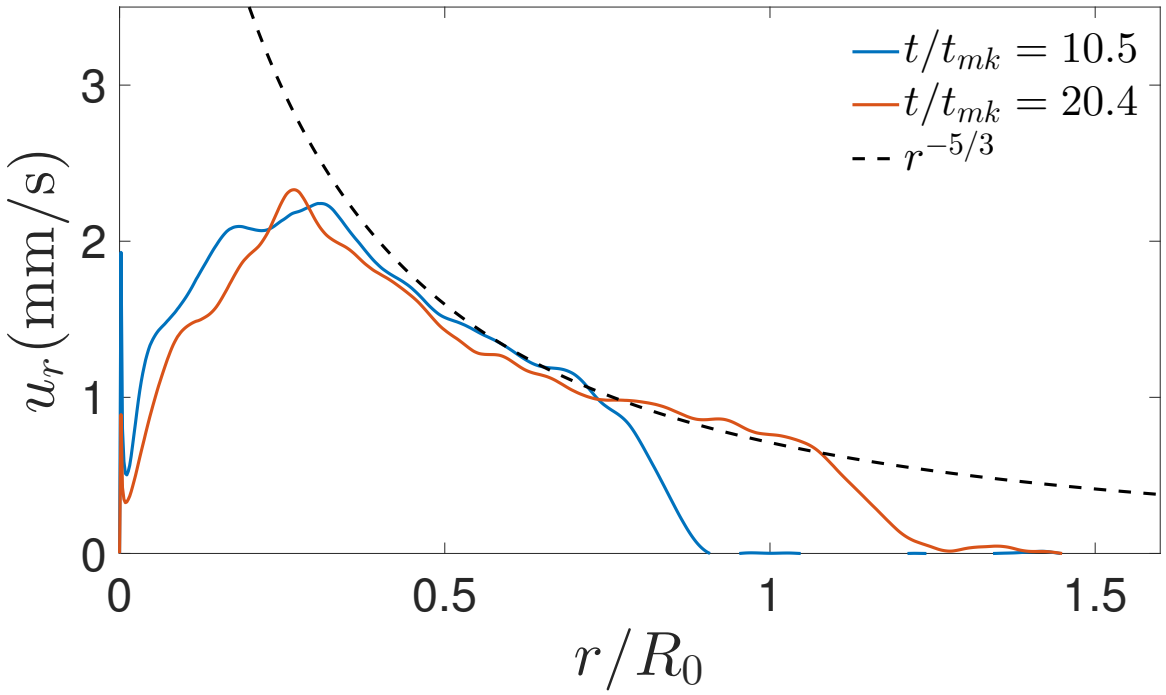

FIGURE 5.11: Azimuthal velocity average of fluid versus non-dimensionalised distance from the source r/R_0 (piv4).

This behaviour is thought to be due to the extent of the departure of the crack shape from a perfect circle around the injection needle. Firstly, a small initial asymmetry is usually introduced into the fracture shape due to the experimental conditions, such as small heterogeneities in the gel. The injected fluid is then drawn into the tip of the quasi-statically propagating fracture, which is not propagating at exactly the same rate at every point of the fracture. Some preferential direction will be established at each time step of propagation. This area will attract more fluid within the fracture. Then, once this preferential direction has changed, the fluid present will circulate around to the more dominant area of growth. This type of behaviour can be seen in Fig. 5.12, where the fracture initially grows preferentially upwards, and then the flow begins to circulate around when more fracturing occurs downwards at later times.

5.6 Drift and eccentricity

When a fracture initially propagates, it forms a circular shape as expected due to the stress state of the gel matrix. However, it was noticed that as fractures evolved the centre of this radial shape began to drift away from the original injection point. This

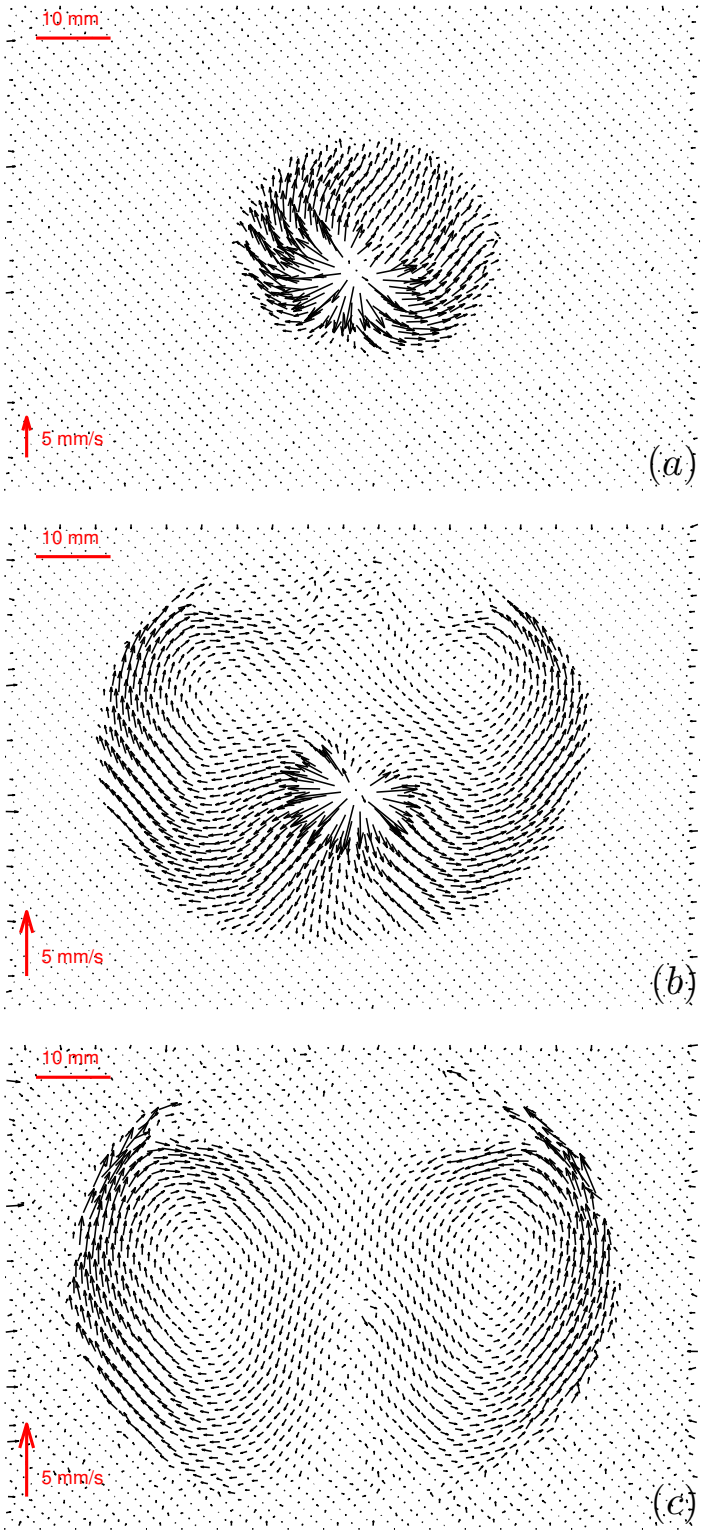

FIGURE 5.12: Average velocity fields at different stages for a fracture transitioning between regimes (piv3). (a) $t/t_{mk} \sim 5\times10^2$, (b) $t/t_{mk} \sim 5\times10^3$ and (c) $t/t_{mk} \sim 1\times10^4$.

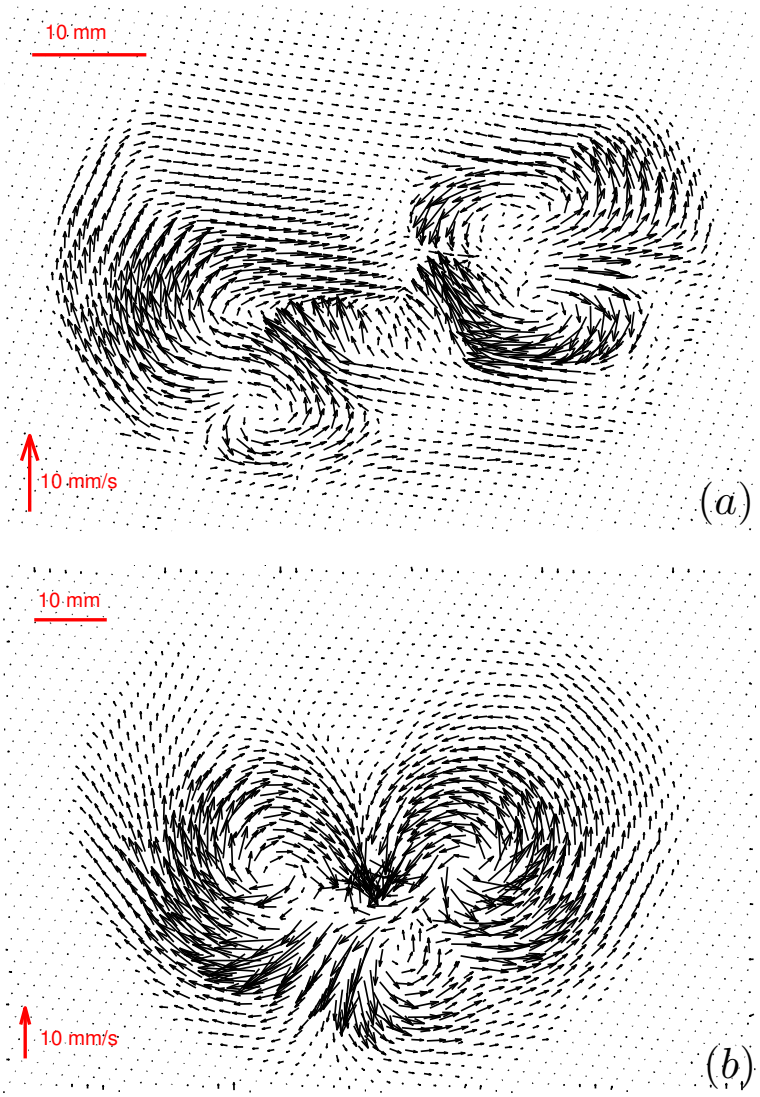

FIGURE 5.13: Average velocity fields at late times for fractures in the toughness regime. (a) $t/t_{mk} \sim 10^{12}$ (piv1) and (b) $t/t_{mk} \sim 10^{11}$ (piv2).

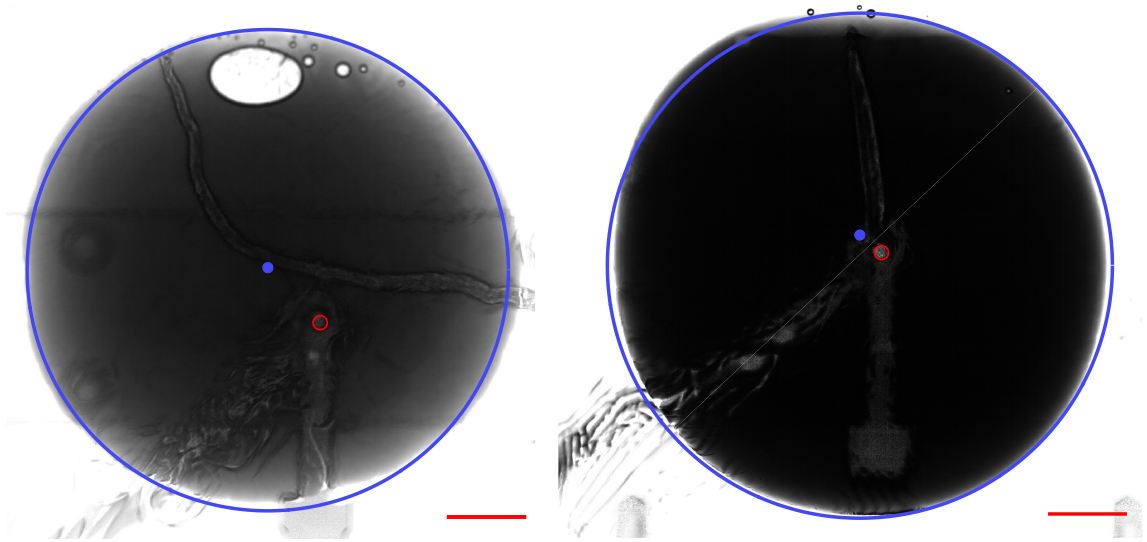

(a) (b)

FIGURE 5.14: Experimental view of fractures, (a) exp7 ($t \approx 12$ s) and (b) exp15 ($t \approx 38$ s). The red circle marks the position of the injection needle. The blue dot represents the centre of the evolving fracture, corresponding to the best fit circle given by the blue line. The red scalebar is 10 mm.

behaviour is thought to be mainly due to small heterogeneities in the gel matrix. If the material toughness K_{IC} varies at different areas in the gel, preferential growth will be established in the direction of least resistance. This will cause the centre of the fracture to move away from the injection point in the preferential direction of growth. An example of this process can be seen in Fig. 5.14, where the blue centre of the fractures have moved significantly from the original red initiation point.

We can analyse this behaviour by examining the dye attenuation measurements for several experiments. The dye provides us with information about the extent of a fracture and from this the two dimensional area can be calculated. Using this data, the MATLAB function *regionprops* can provide details such as the centre of this area, the radius of a circle fit and eccentricity. We can define the drift distance of the new centre from the original position as

$$d_r = \sqrt{(x_n - x_0)^2 + (y_n - y_0)^2}, \tag{5.3}$$

where (x_0, y_0) and (x_n, y_n) are the positions of the injection point and new fracture centre, respectively.

The time evolution of this drift distance d_r for various experiments can be seen in Fig. 5.15(a). The variation of d_r between experiments is observed to be quite significant. Moreover, the centres of the fractures do not always continually increase their distance from the origin (x_0, y_0). Fluctuations in the curves demonstrate that the moving centre can move both away and towards this point. This behaviour appears to be random and not correlated between experiments. One trend that may be deduced from this plot is that the amplitude of these fluctuations appear to dampen with time, eventually settling down to some fixed distance from the origin. This is possibly due to the fact that as the fracture evolves, the perimeter where tensile fracturing is occurring also increases. When this circumference is sufficiently large, small heterogeneities within the gel will have less of an effect on the fracture centre movement. Multiple minor anisotropic material toughness effects present all along the tip will likely cancel each other out, minimising the total effect on preferential fracture propagation direction.

We can also obtain the total drift distance of the fracture centre by calculating the distance between centres at consecutive frames and summing this over the total time of propagation. This distance c_d can be defined as

$$c_d = \sum_{i=1}^{n} \sqrt{(x_i - x_{i-1})^2 + (y_i - y_{i-1})^2}. \tag{5.4}$$

The time-dependence of this parameter for various experiments is plotted in Fig. 5.15(b). Once again, the difference in behaviour is significant between experiments, with an approximate linear dependence with time observed for some experiments, and a higher order power law dependence for other experiments. From the corresponding characteristic timescale t_{mk} values contained in Table 5.1, we notice that generally the more toughness-dominated a fracture is, the more the centre drifts. This trend is expected as any material variations will have a much larger impact on a toughness regime experiment, where bond-breaking is the dominant energy dissipation mechanism.

Finally, we can also estimate the eccentricity of the radial fractures, which is a measure of its deviation from a perfect circle. The eccentricity e can be calculated using the following formulation,

$$e = \sqrt{1 - \frac{b^2}{a^2}}, \tag{5.5}$$

where a and b are the lengths of the semi-major and semi-minor axes, respectively. When $e = 0$ the shape is a perfect circle and when $e = 1$ it is a line segment. Plotting this value versus time in Fig. 5.15(c), we notice that eccentricity is approximately

constant for the duration of the fracturing process. The value is consistently less than 0.5 and averages around a value of 0.3. This means that the fractures are not perfectly circular but $e = 0.3$ is equivalent to only a 5% difference between the length of the semi-major and minor axes. Thus, despite the fracture centre drifting and preferential directions of propagation, the radial assumption is still valid for modelling purposes.

5.7 Conclusions

This chapter describes the properties of a radial fluid-driven fracture in an elastic medium. The literature discussed in Chapter 2 provided scaling relationships of fracture radius, aperture and crack tip shape dependent on the dominant energy dissipation mechanism, viscosity or material toughness. These relationships were then verified experimentally in brittle hydrogels, with transitions between the two regimes also observed. It can be difficult to distinguish between regimes, due to the similarity of the respective power laws describing the growth of the fracture radius with time. This motivated three dynamic measurements, radius, aperture and velocity, to identify the presence of limiting regimes and the possibility of observing the transition experimentally. The toughness regime measurements for radius growth provide good agreement between experimental and theoretical pre-factor values. However, the discrepancy observed between the pre-factors in the viscous regime is significant, suggesting that some unknown physical mechanism might be unaccounted for. It is extremely important in industrial applications of hydraulic fracturing that the regime of propagation is known. The injection timescales for these operations can sometimes be several days. Therefore, even though the power law dependence for radial growth is similar, over large timescales, fractures will propagate significantly further, $\mathcal{O}(10^2$ m), in the viscosity regime compared to toughness-dominated cracks.

PIV analysis of fluid within these fractures revealed that two distinct types of flow are also present. In the viscosity limiting case, the fluid travels radially outwards from the source to the tip, as expected. However in the toughness limiting case, where the quasi-static propagation of the crack is not dependent on the flow, the fracturing fluid travels in a more complex manner, circulating within the crack. This type of flow will have a significant effect on the transport of proppants within fractures, and ultimately on the success of a hydraulic fracturing operation. The flow pattern may inhibit the ability of the proppants to travel to desired locations so that fractures are propped open and gas extracted.

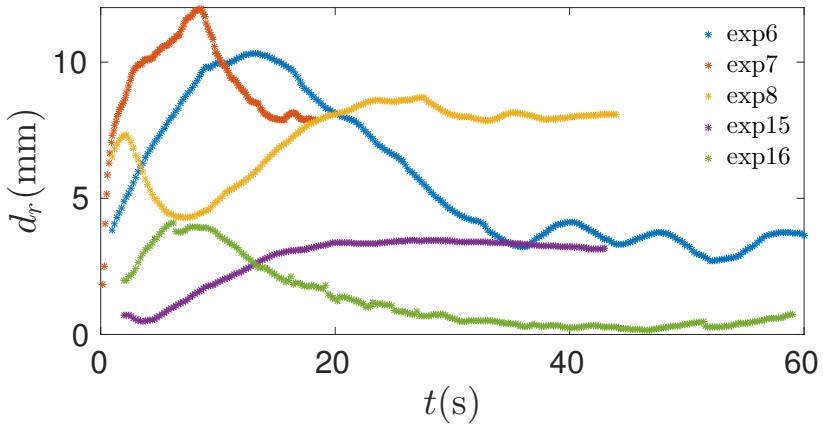

(a)

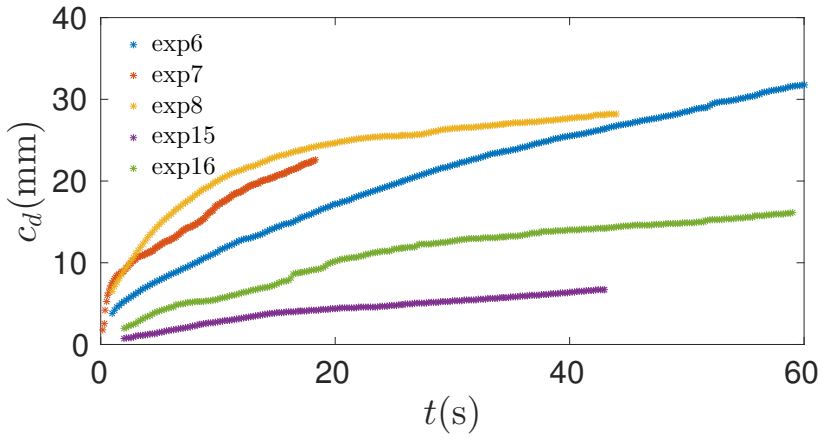

(b)

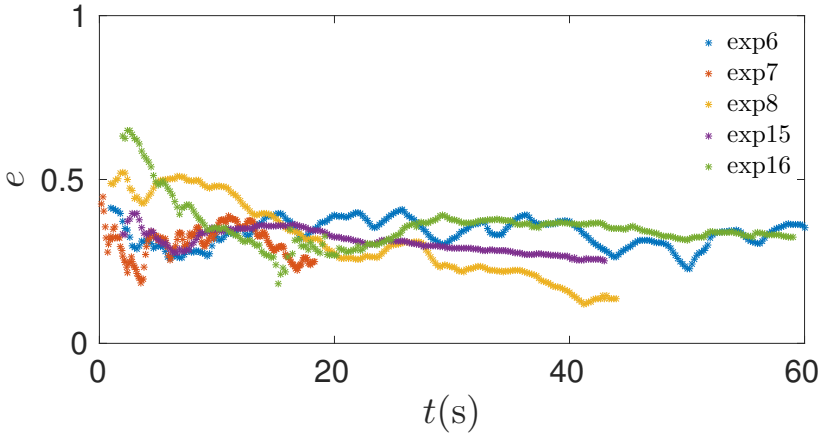

(c)

FIGURE 5.15: (a) The distance of the fracture centre from the injection origin d_r versus time. (b) The cumulative distance travelled by the fracture centre c_d versus time. (c) The eccentricity of the fracture e versus time.

Finally, the asymmetry around the injection point of the fracture was analysed. Drift of the fracture centre was found to be more pronounced in toughness-dominated experiments due to heterogeneities in the gel matrix having more of an influence than in the viscous regime. This drift may explain and drive the flow-fields observed from PIV measurements.

These results involving a single fracture inspired our next area of focus, where we analyse the interaction of two radial fractures propagating in the same plane. This leads to complex physical processes but also provides more of an insight into how fracture networks or formations may develop.

Chapter 6

Two coplanar radial fluid-driven fractures

6.1 Introduction

In this chapter we discuss a dual-fracturing experiment in which two injection needles initiate radial fractures that propagate in the same plane and coalesce in a gel matrix. This experiment was designed to observe fundamental dynamics that can occur in a fracture network and provides a wide range of physical mechanisms to be studied. The areas we focus on include pre-coalescence growth of the fractures, coalescence dynamics along the bridge between fractures, transition to a single fracture, asymmetric coalescence, non-coalescing fractures and the resulting fracture surface patterns created. Each of these areas include many interesting phenomena, which will be detailed in the sections to follow. Some of the information in § 6.4 has been published in O'Keeffe *et al.* (2018).

6.2 Experimental setup

To investigate the coalescence of hydraulic fractures, we designed a dual-fracturing experimental setup, which consisted of two injection needles with radii of 0.81 mm set in a polyacrylamide hydrogel of dimensions $100 \times 100 \times 77$ mm (Fig. 6.1). Similarly to our previous setup, four polycarbonate plates of 1 mm were introduced into the sides of the acrylic container to impose a small initial principal stress perpendicular to the needle, which sets the direction of fracture propagation as detailed in Chapter 3. In addition,

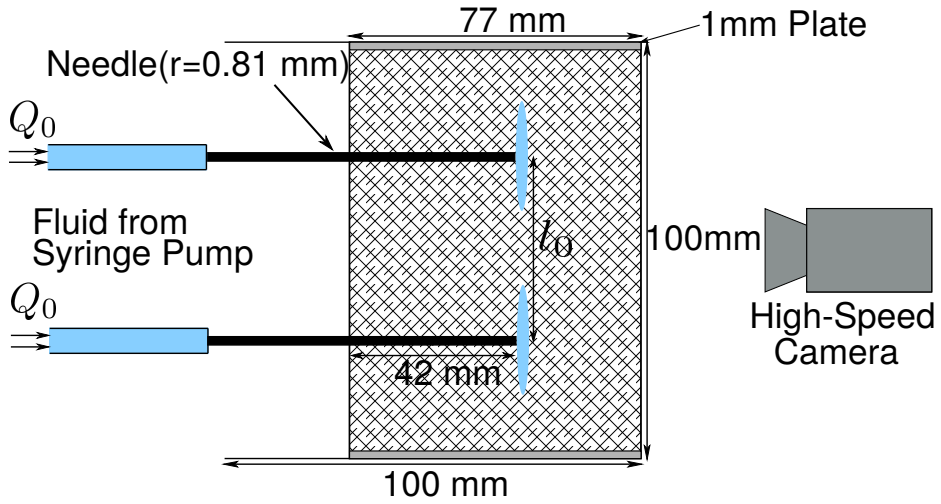

FIGURE 6.1: Schematic of the dual-fracturing experimental apparatus. Fluid is injected from two separate syringes on a dual-syringe pump to ensure an equal injection rate into both fractures, which are generated on the same plane.

inserting these plates ensures that the two tensile fractures coalesce approximately on the same plane, as long as the needle positions are fixed to the same depth into the gel. The two needles were placed a distance l_0 apart, which is chosen to be sufficiently large so that any rapid fracture due to initiation ($R \lesssim 5$ mm) around the needle tip does not influence the dynamics of coalescence. The separation l_0 is also sufficiently small so that finite container size does not affect fracture propagation.

The hydrogels used in these experiments are the same as those in Chapter 5, whose properties were detailed in Chapter 4. Both the Young's modulus E and fracture toughness K were varied between experiments, by using different amounts of gel concentrations. Newtonian fluids of varying dynamic viscosities μ, such as water and glycerin mixtures, were injected at constant volumetric rates Q_0 through each needle into the hydrogel using a syringe pump (HA PhD Ultra). The experimental parameters were chosen so that the fractures propagate in the toughness-dominated regime before coalescence. Similarly to the single fracture experiments, all measurements were taken using a high speed camera (Dalsa Falcon 2 4MP) and the Digiflow software was used extensively in processing the videos and taking measurements.

Once again, we implemented both light attenuation and PIV techniques to obtain dynamic measurements of fracture radial extent, aperture and internal flow velocity (see Chapter 3).

6.3 Pre-coalescence

In our experimental setup, fractures are initiated at the tip of the injection needles and propagate into the solid matrix. Initially, the two fractures propagate independently of one another as isolated penny-shaped fractures in the x-y plane, where the injection needles are aligned along the x-axis. With time, the distance between the fractures gradually reduces until the fractures begin to interact, altering the direction of growth. An example of this can be seen in Fig. 6.2, where two fractures are propagating in the toughness regime (Chapter 5). After a certain time the fractures establish a preferential direction of growth towards the other fracture in the medium. The internal flow fields for such an experiment, Figs. 6.2(b) and 6.2(d), show that the fluid travels preferentially towards the other fracture, with fluid near the outer tips circulating around. This behaviour can be explained by analysing the stress state in the gel, which induces propagation in the direction of the other cavity, causing coalescence.

All the experiments used in this chapter propagate in the toughness regime, where the radius transition timescale varies from $8 \times 10^{-7} \leq t_{mk} \leq 4 \times 10^{-4}$, as seen in Table 6.1.

6.3.1 Stress state

The stress state around a fracture may be represented by stress functions using complex variable methods (Westergaard, 1939). To visualise the distribution of stress around a two-dimensional fracture inside an elastic solid, a set of curves can be constructed of equal principal shearing stress $\tau = \alpha p_0$, where α is a parameter and p_0 is the pressure within the crack (Sneddon, 1946). These curves are the same as the isochromatic lines of photoelasticity, which can be visualised using polarisers for some gel systems. A sample plot of these isochromatic lines for a single fracture can be seen in Fig. 6.3(a). As expected, the contours concentrate around the crack tips at either end of the two-dimensional crack, where there is a singularity in the tip stress. Thus, when fracturing occurs it takes place at these positions, where the stress is highest and capable of overcoming the strength of the material.

This method has also been carried out for collinear two-dimensional Griffith cracks in Willmore (1949) and Yokobori *et al.* (1965). An example of the isochromatic lines around two equal length fractures placed a certain distance apart can be seen in Fig. 6.3(b). From this figure it can be seen that the presence of the second crack significantly increases the stresses near the tips of the cracks closest to each other. This

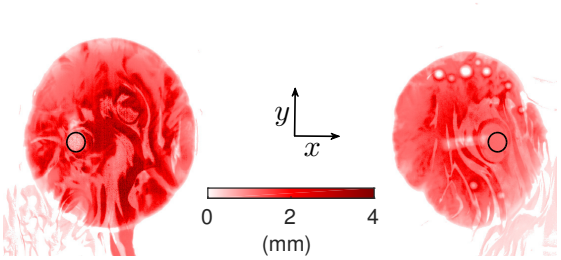

(a) $t = -5.9$ s

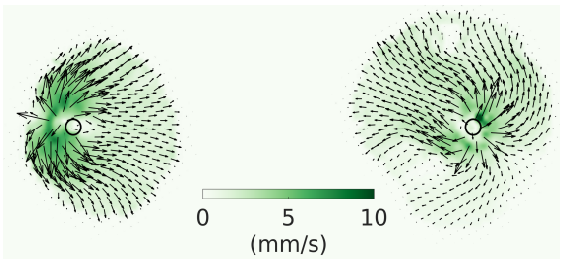

(b) $t = -6.25$ s

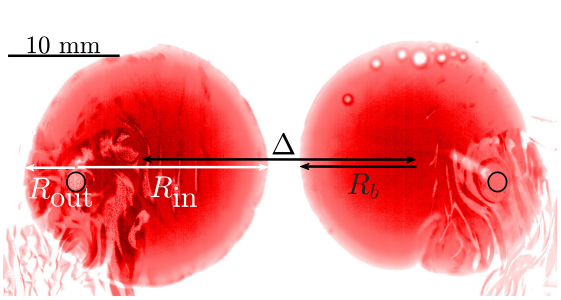

(c) $t = -0.6$ s

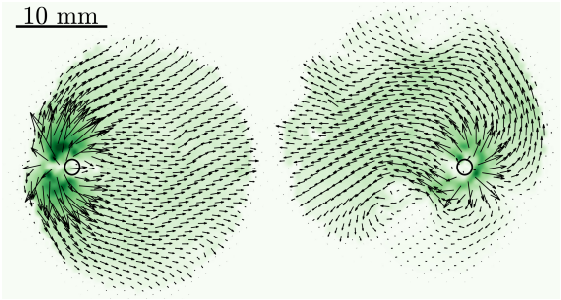

(d) $t = -0.8$ s

FIGURE 6.2: Dual-fracture evolution pre-coalescence. Light attenuation experimental images (db3) are shown in (a) and (c). Velocity fields (pivdb13) of the fracturing fluid are shown in (b) and (d), where the colour bar corresponds to velocity magnitude. Times given are negative because $t = 0$ corresponds to the moment of coalescence.

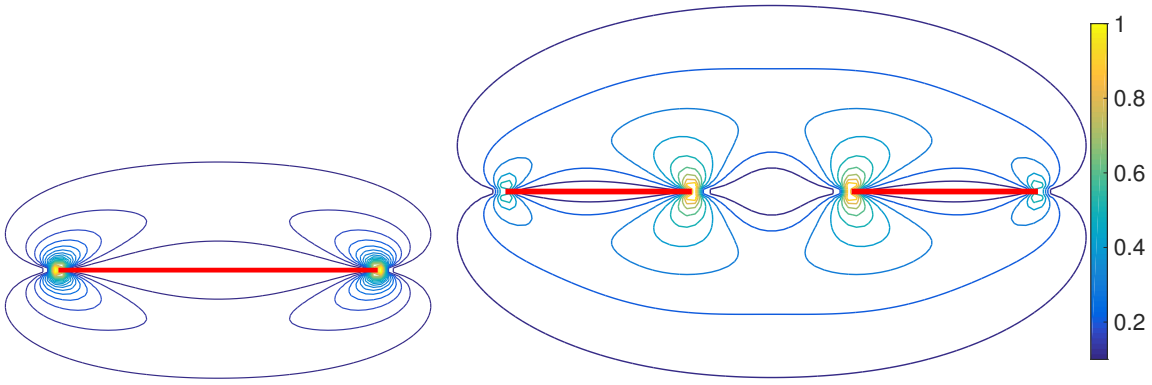

(a) (b)

FIGURE 6.3: Contour plot of the shear stresses around: (a) a single two-dimensional fracture (Sneddon, 1946); (b) two collinear two-dimensional fractures of equal length with spacing between them equal to 6/7 of the length of each crack (Willmore, 1949). The fractures are shown in red. The curves are the isochromatic lines of photoelasticity. The colour bar used is the value of the contours normalised by the maximum principal shearing stress value.

indicates that fracturing will preferentially take place in these positions compared with the outer tips.

Although we only briefly discussed a two-dimensional system, the principal shearing stress around a three-dimensional radial crack is similar in shape to that in Fig. 6.3(b), and the stresses become infinite near the crack tip where some plastic flow will occur (Sneddon, 1946).

6.3.2 SIFs for two coplanar radial fractures

As mentioned in § 2.2.3, stress intensity factors (SIFs) predict the stress state near the tip of a crack. Since propagation in the toughness regime is dependent on the criterion (2.11), the behaviour of attraction between the cracks is determined by the SIFs. In Xiao *et al.* (1994) an approximate solution for the problem of two coplanar penny-shaped cracks under uniaxial tension was obtained using a superposition principle. Consider two penny-shaped fractures with their centres aligned in the x-direction. Crack A is the left crack with radius R_a, crack B is the right crack with radius R_b and the distance between their centres is given by Δ, where $\Delta = l_0$ at $t = 0$, but not necessarily afterwards due to centre drift as shown in Fig. 6.2(c). Two coordinate systems are defined (x_a, y_a, z_a) and (x_b, y_b, z_b), with origins situated at the centres of cracks A and B respectively. These are related by

$$x_b = x_a - \Delta, \qquad y_b = y_a, \qquad z_b = z_a. \tag{6.1}$$

The SIF on the boundary of A is given by

$$K_I^a = 2\sqrt{\frac{R_a}{\pi}}\sigma_{zz}\left[1 + \vartheta\left(\frac{R_b}{\Delta}\right)^3 + \vartheta\left(\frac{R_b}{\Delta}\right)^3\frac{x_a}{\Delta} + \frac{24}{5}\vartheta\left(\frac{R_b}{\Delta}\right)^3\left(\frac{x_a}{\Delta}\right)^2 - \frac{9}{10}\vartheta\left(\frac{R_b}{\Delta}\right)^3\left(\frac{R_a}{\Delta}\right)^2 + \frac{3}{5}\vartheta\left(\frac{R_b}{\Delta}\right)^5\right] + \mathcal{O}(\delta^6), \tag{6.2}$$

where $\delta = \max(R_a, R_b)/\Delta$ is a dimensionless quantity and ϑ is a constant related to Poisson's ratio of the elastic matrix,

$$\vartheta = \frac{2(3-4\nu)(1-\nu)^2}{3\pi(1-2\nu)^2}. \tag{6.3}$$

Also, the SIF on the boundary of B is given by

$$K_I^b = 2\sqrt{\frac{R_b}{\pi}}\sigma_{zz}\left[1 + \vartheta\left(\frac{R_a}{\Delta}\right)^3 - \vartheta\left(\frac{R_a}{\Delta}\right)^3\frac{x_b}{\Delta} + \frac{24}{5}\vartheta\left(\frac{R_a}{\Delta}\right)^3\left(\frac{x_b}{\Delta}\right)^2 - \frac{9}{10}\vartheta\left(\frac{R_a}{\Delta}\right)^3\left(\frac{R_b}{\Delta}\right)^2 + \frac{3}{5}\vartheta\left(\frac{R_a}{\Delta}\right)^5\right] + \mathcal{O}(\delta^6). \tag{6.4}$$

It is interesting to note in this case that the SIFs are dependent on the Poisson's ratio of the material, which is not relevant in the single fracture case.

In Xiao *et al.* (1994) a comparison of the effect that the presence of the second crack has on the SIF of the first crack is presented. Only one fracture needs to be analysed, because all the results are similar for the other fracture. We normalise K_I^a by K_I^0, the SIF for a single penny-shaped crack under uniaxial tension,

$$K_I^0 = 2\sqrt{\frac{R_a}{\pi}}\sigma_{zz}, \tag{6.5}$$

which can be derived from (2.13) when constant pressure, $p = \sigma_{zz}$, is assumed.

If we take $\nu \approx 0.48$ (§ 4.3.1), so that $\vartheta \not\to \infty$, the differences between the SIFs in the coplanar fractures and the single fracture case can be seen in Fig. 6.4. For fractures of the same length we can see the evolution of the SIF for one of the fractures from

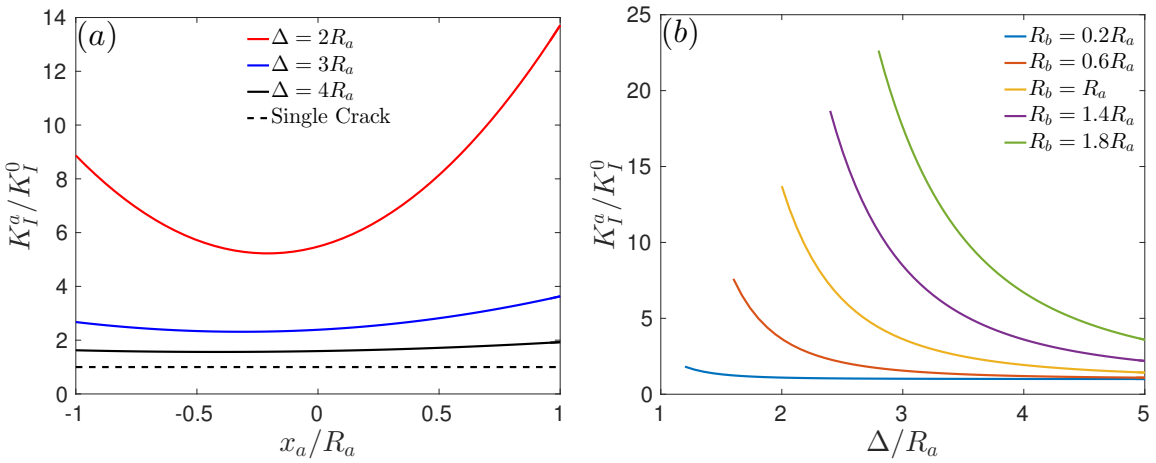

FIGURE 6.4: (a) Normalised SIF at the edge of crack A when the cracks are equal in length. (b) Normalised SIF at the right tip of crack A with varying crack length ratios R_b/R_a (Xiao *et al.*, 1994).

Fig. 6.4(a), with varying distances between the centres. Here, it is evident that when the distance between the fractures decreases the SIF increases. Clearly, the SIF is not constant along the edge of the crack, with a maximum value obtained at the point closest to the other fracture. This reveals that the easiest direction for propagation to occur is towards the other fracture, and explains the non-uniform growth along the edge seen in Fig. 6.2. Moreover, in Fig. 6.4(b) the effect on the SIF when both fractures are unequal in radius is shown. We notice that a larger crack has a much larger effect on the SIF of a smaller crack, compared with a minimal effect on the SIF of the larger crack by the smaller crack.

Under the assumption that the flow within the crack is quasi-steady in the toughness regime, we may apply these SIF relations deduced under the assumption of uniform tensile stress to the fluid-driven fracture problem. Therefore, pressure within the fracture is independent of space and only a function of time, and the uniaxial tension assumption is satisfied with $\sigma_{zz} = p(t)$. We note that in the viscous regime, pressure is dependent on distance from the source, however SIFs are not used in the analysis of this regime.

Exp	l_0(mm)	E(kPa)	μ(Pa·s)	Q_0(mL/min)	γ_s(Jm^{-2})	t_{mk}(s)	$t_{\mathcal{MK}}$(s)
db2	40	125	0.08	11	4.4	2×10^{-7}	-
db3	40	97	1.13	5	5.2	2×10^{-5}	5×10^{-4}
db6	40	125	1.13	2	4.4	1×10^{-5}	-
db8	40	97	1.13	2	5.2	3×10^{-6}	2×10^{-4}
db12	40	125	1.13	20	4.4	4×10^{-4}	3×10^{-3}
db16	35	157	0.2	15	5.2	3×10^{-6}	-
db20	35	125	0.28	10	4.4	5×10^{-6}	2×10^{-4}
db21	30	125	0.66	2	4.4	3×10^{-6}	2×10^{-4}
db22	35	320	0.66	20	3.6	4×10^{-4}	4×10^{-3}
db23	35	97	0.55	15	5.2	1×10^{-5}	-
db24	35	97	0.57	15	5.2	1×10^{-5}	-
db25	35	157	0.55	5	5.2	6×10^{-6}	-
db30	35	97	0.26	10	5.2	1×10^{-6}	-
pivdb9	40	97	0.4	5	5.2	8×10^{-7}	7×10^{-5}
pivdb11	35	157	0.3	7	5.2	3×10^{-6}	-
pivdb13	40	97	0.44	5	5.2	1×10^{-6}	8×10^{-5}
pivdb14	35	157	0.35	5	5.2	2×10^{-6}	1×10^{-4}
pivdb15	30	125	0.37	5	4.4	3×10^{-6}	2×10^{-4}

TABLE 6.1: Dual-fracturing experiments conducted with particular values of physical parameters and the corresponding characteristic timescales.

6.3.3 Results

When an experiment commences, the syringe pump causes fluid pressure to build in the injection needles located in the gel matrix. Once this pressure is greater than the material toughness at the end of these needles, the fractures propagate. However, due to small differences in the toughness of the material, ensuring fractures are initiated at the exact same time is very difficult. Thus, in most of these experiments a small offset time t_{off} is observed between initiations, where $t_{\text{off}} \lesssim 1.5$ s.

6.3.3.1 Radial growth

Analysing the growth of the fractures before coalescence, we can examine the radial extent in a number of different ways. If we take the radius R as half the diameter of

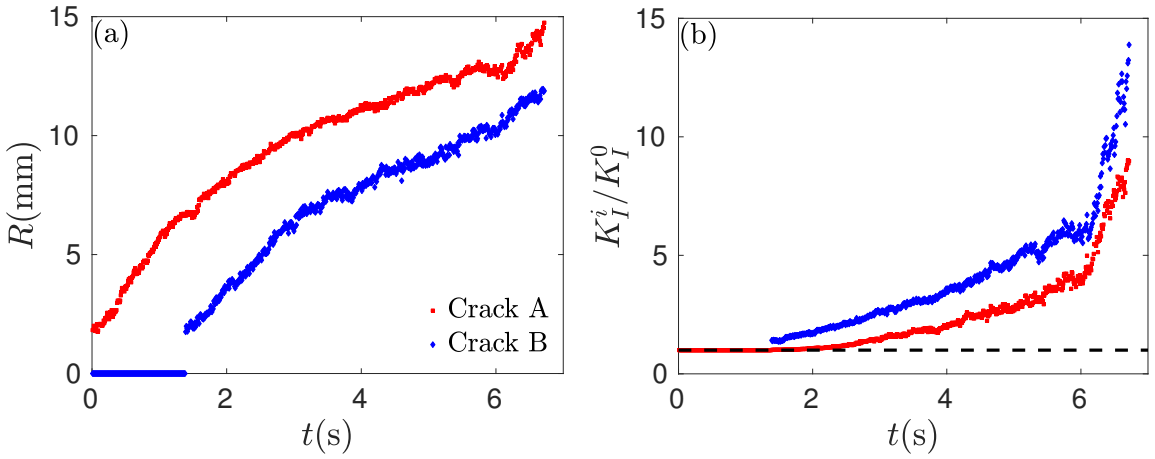

FIGURE 6.5: (a) Fracture radii, R, versus time for both the left and right fractures A and B, where $t = 0$ is the moment the first fracture propagates (pivdb14). (b) Normalised SIFs at the inner tips K_I^i/K_I^0 for both cracks versus time, where i = A,B.

the whole fracture, a sample plot (piv db14) of the evolution of this physical parameter can be seen in Fig. 6.5. In this figure it is first noticeable that the fractures do not start at the same time, with crack A starting at $t = 0$ and B at $t = t_{\text{off}} \approx 1.5$ s. Secondly, we can see that just before coalescence near $t = 6$, there is a sudden large increase in the rate of growth of both fractures. From § 6.3.2 we know that the SIFs will be largest at the tip of the fracture closest to the other, and propagation will preferentially take place in this direction (Fig. 6.2). Plotting the SIFs at this point produces Fig. 6.5(b). Here, before the second fracture propagates, the SIF is constant and equal to that of a single radial crack. Then, as the second fracture is introduced into the matrix, the SIFs for both cracks slowly increase, with the bigger fracture having a larger effect on the smaller fracture. Corresponding to the late time growth rate increase in Fig. 6.5(a), a significant increase in the SIFs of the cracks is evident at the same time, explaining the mechanism for this rapid growth.

We also examine the growth of each fracture without accounting for the time offset t_{off}. Taking $t = 0$ as the time when an individual fracture starts, we plot the raw experimental evolution of R with time in Fig. 6.6(a). It is evident that the growth follows a $t^{2/5}$ power law behaviour, similar to that of a single fracture in the toughness regime, until late times when the fractures coalesce and growth along the line connecting their centres ceases. It is also noted that for each individual experiment the first and second fractures to propagate follow a similar growth trajectory with time, as denoted by the diamond and pentagram markers, respectively. In Fig. 6.6(b) we can see that the

toughness scaling law (2.30) presented for the single crack case in Chapter 2, performs well in collapsing the data onto a single curve. The pre-factor for this universal curve is also ≈ 0.8, which agrees with the theoretical and previous experimental results.

The growth of both inner and outer fracture extent from the injection source can also be examined, without accounting for the time offset t_{off}. We define R_{in}, the inner radius, as the fluid filled region along the x-axis starting at the injection point, in the direction towards the other fracture and ending at the crack tip, as shown in Fig. 6.2(c). Similarly, we define R_{out}, the outer radius, as the fracture extent from the injection point to the outer tip along the x-axis. The physical measurements of these parameters and their evolution with time are shown in Fig. 6.7. In Fig. 6.7(a) at early times where $t \lesssim 1$, for most experiments a $t^{2/5}$ growth behaviour is noted. The times when this behaviour is observed corresponds to the time when the fractures propagate independently of each other, in a similar manner to that observed in Chapter 5. During this timescale the outer radius R_{out} also has an approximate $t^{2/5}$ growth rate, seen in Fig. 6.7(b). After this initial phase, the growth of the inner and outer radii transition to different rates of growth. The outer radius R_{out} stagnates after this initial time, with no further growth occurring before the cracks coalesce. On the other hand, R_{in} transitions to a $t^{4/5}$ growth rate. This is easily explained by the fact that once the SIFs on the inner tips are sufficiently large, all growth occurs in this direction and therefore, the growth rate previously occurring on the outer tips is transferred to the inner tip, resulting in the compounded new inner radius evolution rate.

Additionally, we note the large increase in growth observed in Fig. 6.5 at late times just before coalescence is observed in all experiments. However, this is not so evident in Fig. 6.6 due to the spacing between points and the logarithmic scale.

Finally, we can analyse the separation between the inner tips, which we define as $\widehat{\Delta} = \Delta - R_a - R_b$. In Fig. 6.8(a) we can see the decrease of $\widehat{\Delta}$ over time and the times of offset for each experiment. Fig. 6.8(b) shows the ratio of the inner and outer SIFs for each fracture as the distance between the fractures decreases. When $K_I^i(\text{in})/K_I^i(\text{out}) > 1$, propagation takes place only at the inner tips. This does not take place at one critical separation distance for every fracture due to the variation of initiation times in each experiment, but is approximately seen around $\widehat{\Delta} = 0.03$ m.

6.3.3.2 Aperture growth

Casting our attention towards aperture data from the light attenuation measurements, we once again observe the preferential growth directions and drift of the fracture centre.

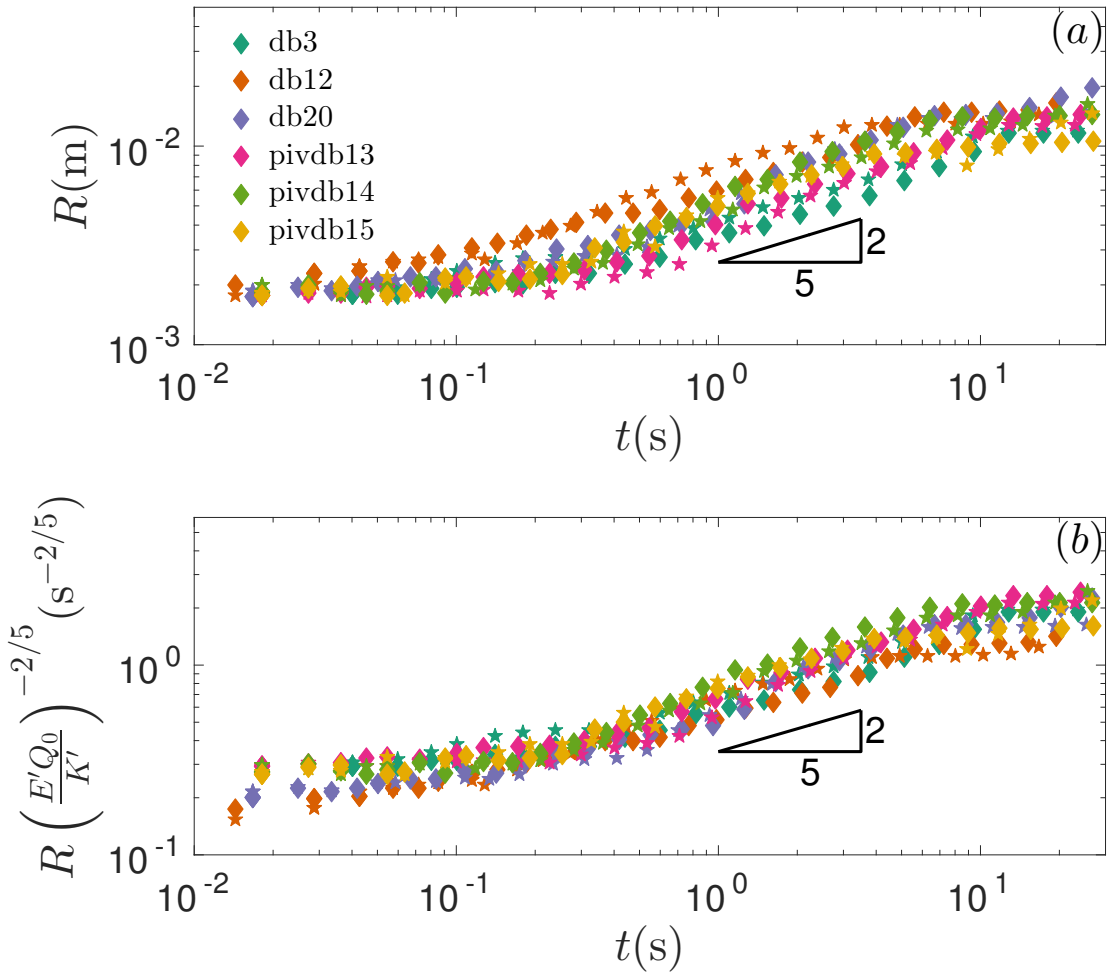

FIGURE 6.6: (a) Fracture radii R growth versus time, where R is half the fracture diameter. (b) Scaled fracture radii measurements versus time using (2.30) and $K_I = K_{\mathrm{IC}}$ the material toughness (2.11). The radius R is defined as half of the fracture diameter. Diamond and pentagram markers denote the first and second fractures to propagate for each experiment, respectively.

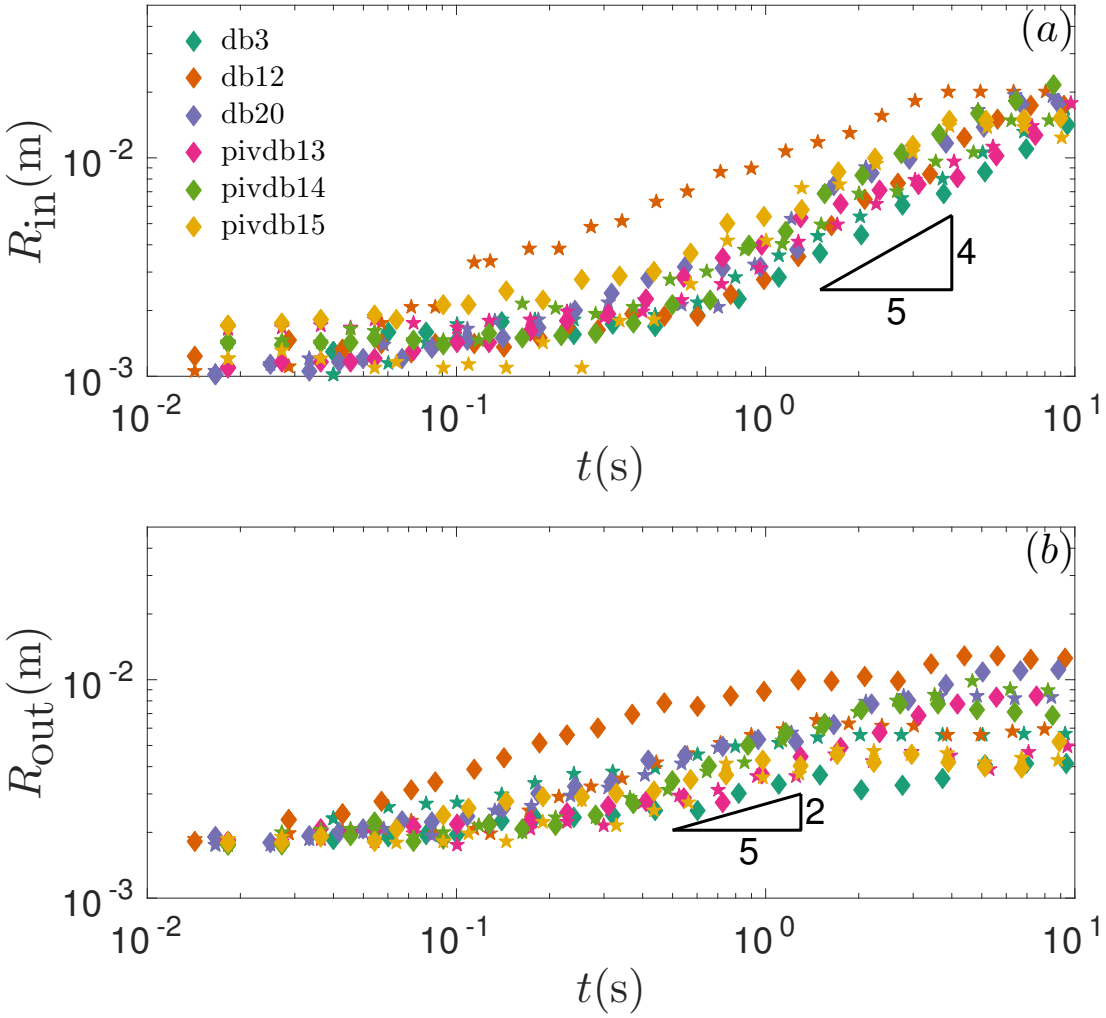

FIGURE 6.7: (a) Inner fracture radii, R_{in}, growth versus time. (b) Outer fracture radii, R_{out}, growth versus time. Measurements are shown for both fractures. Diamond and pentagram markers denote the first and second fractures to propagate for each experiment, respectively.

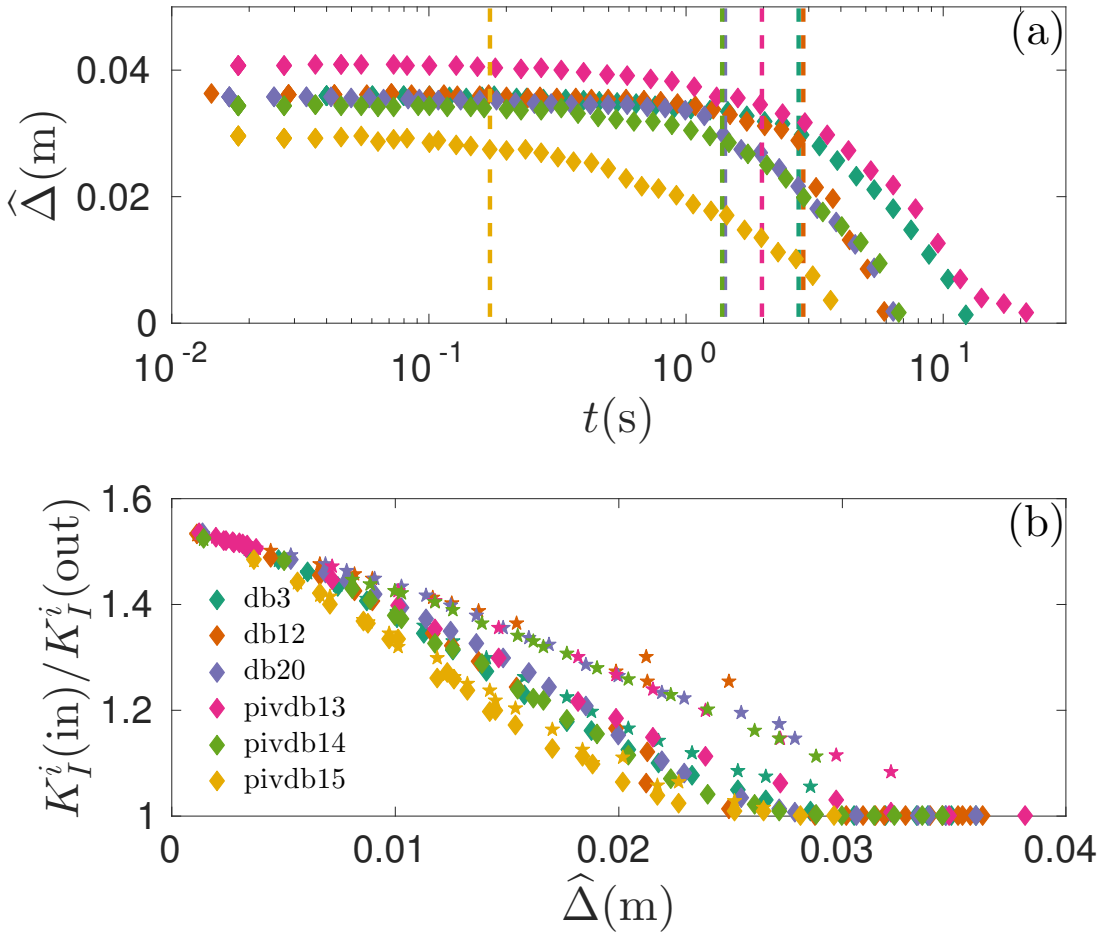

FIGURE 6.8: (a) The time evolution of the separation between the fracture inner tips $\widehat{\Delta}$. The vertical dashed lines mark t_{off} of the second fracture. (b) The ratio of the SIFs at the inner and outer tips of each fracture versus the separation $\widehat{\Delta}$. Diamond and pentagram markers denote the first and second fractures to propagate for each experiment, respectively.

Choosing a sample experiment (db12), we plot the aperture measurements at varying times in cracks A and B in Fig. 6.9(a) and (b). Crack B is the first fracture to propagate, with crack A being initiated at a lag time $t_{\text{off}} = 2.9$ s. The times shown in Fig. 6.9 correspond to $t = 0$ being the moment of initiation for each fracture individually, i.e. $t_b = t_a + t_{\text{off}}$. Measurements around the needle and at very early times are omitted, as the injection tube apparatus and fixings block the lighting of these regions, meaning there is a lack of data at these points.

In Fig. 6.9(a) and (b), we see that the fracture growth on the outer tip ceases after a certain time. More growth is evident in the outer tip of fracture B than in A, as initially B is a solitary fracture present in the medium and growth is only arrested when the other fracture emerges around $t_b \gtrsim t_{\text{off}}$. As the offset time is quite large, once fracture A emerges, fracture B is of a substantial size that the affect on A's SIF is significant. Thus, the outer tip of A is arrested quickly and growth in the inner tip is much more extensive even at early times.

The fractures can then be centred at 0, so that they are symmetric and the radii values correspond to half the diameter. This is constructed in Figs. 6.9(c) and (d) for both fractures. Here, it is noted that fracture B is slightly larger than A due to the significant offset noted before. These centred measurements are then treated similarly to that of the single radial fracture, and we attempt to collapse the aperture profiles using the previously presented toughness scalings for both radial extent and aperture in Table 2.1. Applying these in Figs. 6.9(e) and (f), we obtain a satisfactory collapse of the data, which is comparable with the corresponding results in Chapter 5 (Fig. 5.6). This implies that the treatment of both of these fractures pre-coalescence, as single fractures in the toughness regime is justified, provided they are centred to account for preferential growth induced by the presence of the other cavity.

6.3.4 Drift and eccentricity

The drift of the centre of these fractures can be analysed similarly to those of the single fracture experiment in § 5.6. Again, we define and calculate the drift position d_r as the distance away from the original injection point at a particular time, using (5.3). The drift in the coplanar fracture scenario given in Fig. 6.10(a), has significantly fewer fluctuations than for a single fracture (Fig. 5.15(a)) and is only increasing with time. However, this is expected due to the attraction that occurs, meaning the centre is always moving away from the fluid source.

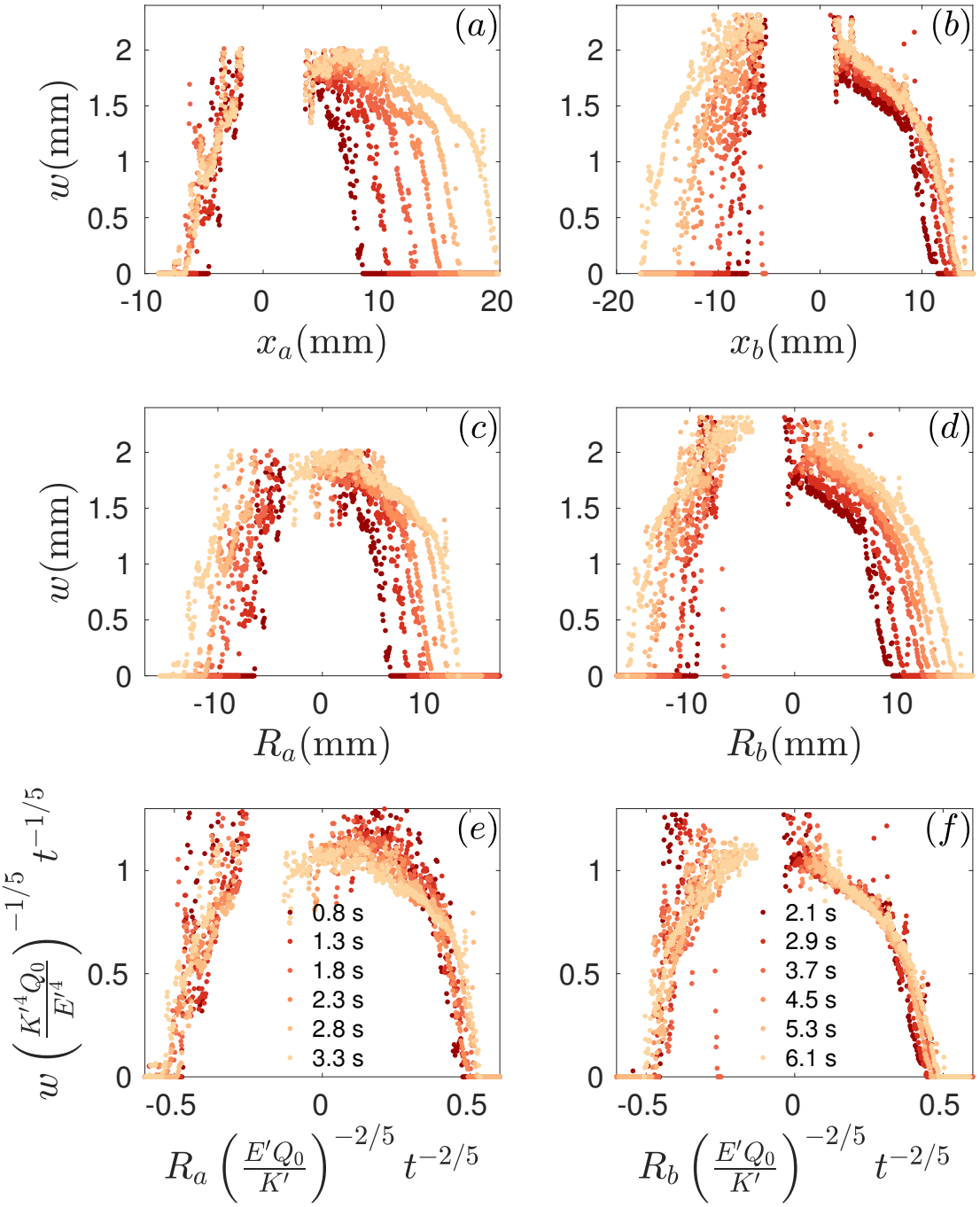

FIGURE 6.9: Aperture profiles of a cross section intersecting the injection needles of both fractures (db12). The first and second columns represent the left and right fractures (A and B), respectively. In this particular example fracture B propagates first and A second with $t_{\text{off}} \approx 2.9$ s. (a) & (b) Raw aperture measurements and the centre is located at the injection point. (c) & (d) Profiles centred so that the radii are half the diameter values. (e) & (f) Scaled profiles using toughness scalings in Table 2.1.

The total drift, using (5.4) as a function of time, is seen in Fig. 6.10(b). The variation in c_d is comparable for each experiment, which may be explained by the fact their transition timescales t_{mk} are similar in magnitude (Table 6.1).

The eccentricity (5.5) of these fractures is observed in Fig. 6.10(c). The values range from $0.1 \lesssim e \lesssim 0.5$ and the behaviour is similar to, but with more variation than, that of the single fracture experiments (Fig. 5.15(c)). Nonetheless, when the fractures are most eccentric, at $e \approx 0.5$, the length of the minor axis is 87% that of the major axis. Thus, the circular approximation is still satisfactory for deducing geometric relationships (see § 6.4.3). A signature increase in ellipticity as time increases towards the coalescence point is not seen due to variation in ellipticity after fracture initiations and time offsets involved.

6.4 Coalescence

A representative time evolution of the coalescence between two fractures is shown in Fig. 6.11 and a composite image of overlain fracture edges is also exhibited in Fig. A.1. After the attraction towards each other, they are observed to coalesce and form a narrow bridge at a particular time. In this section, this time of coalescence is defined as $t = 0$. Shortly after coalescence, we observe that significant fracture growth only occurs in the region close to the bridge, which causes a rapid growth of this bridge (Fig. 6.11(b)). When the bridge half length d becomes comparable to the diameter $2R_0$ of each fracture, growth spreads to the entire envelope of the two interacting fractures. It is crucial to note that $R_0 \neq l_0/2$, due to the drift of the fracture centre as described above. As time progresses, the two fractures gradually become indistinguishable, and approach the shape of a standard single radial fracture. PIV measurements are provided for each stage of the fracturing and coalescing process in Figs. 6.11(a)-(e). We can see from Fig. 6.11(a) that initially the flow is mostly radial, similar to that observed at early times for single fractures in the toughness regime (see Chapter 5). Once the fractures coalesce, the flow everywhere is attracted towards the bridge and a large increase in velocity occurs in the vicinity of the bridge, as shown in Fig. 6.11(b) where the velocity scale is four times that of the other PIV images. After this initial spike in velocity and as the bridge begins to grow, a stagnation point develops, which is identified by the white region in the centre of the coalesced fracture in Figs. 6.11(c)-(e). Within this area, velocity vectors are pointing along the bridge in the y-direction towards its edges.

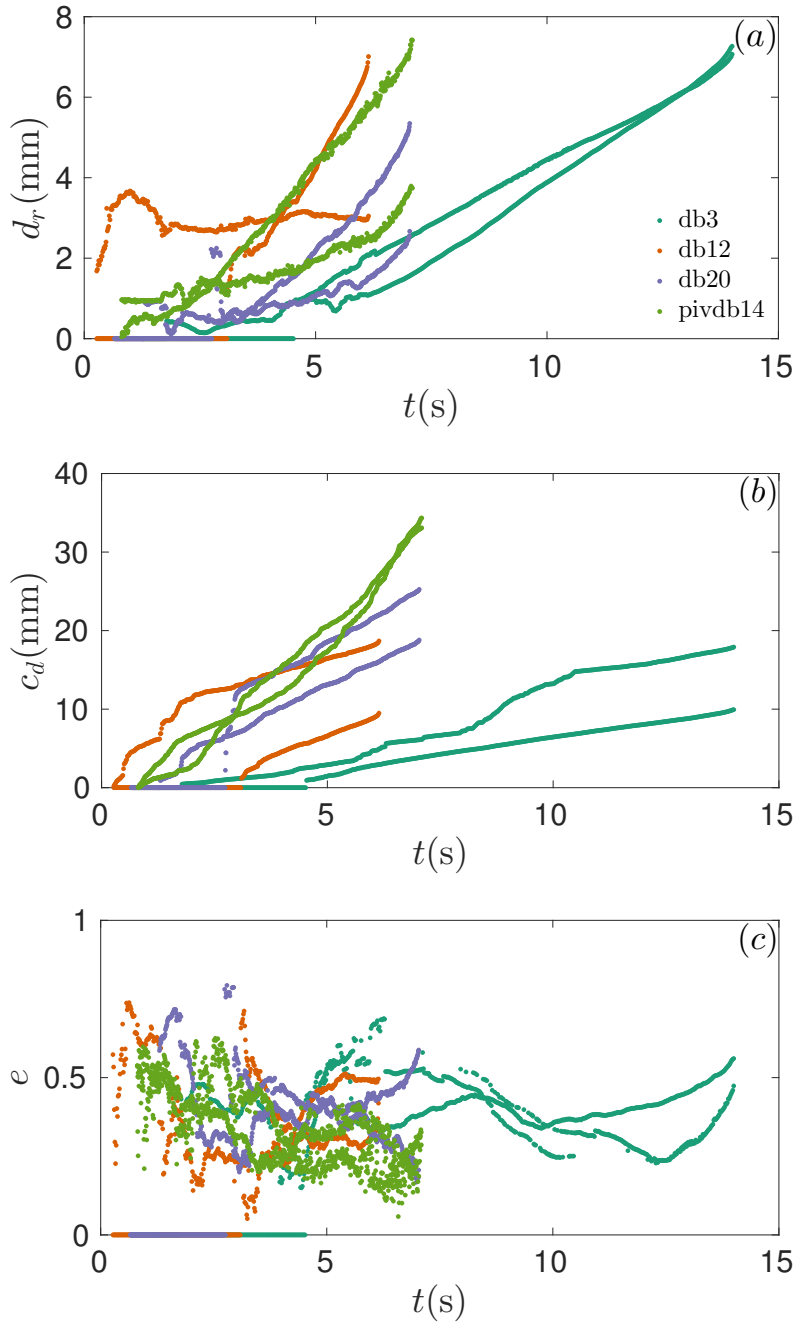

FIGURE 6.10: (a) The distance of the fracture centres from the injection origin d_r versus time. (b) The cumulative distance travelled by the fracture centres c_d versus time. (c) The eccentricity of the fractures e versus time. The time $t = 0$ is the moment the first fracture propagates

In Figs. 6.11(f) and (g) we can see the evolution of coalescence along the x-z plane. Shortly after the cracks first touch, the profile in this plane centred on the point of coalescence can be seen to level out quickly. A three dimensional image of the bridge at a particular time is also shown in Fig. 6.12, where the full shape of the bridge and its roughness can be seen.

6.4.1 Initial rapid growth

From light attenuation measurements we can analyse the growth of the bridge around the moment of coalescence. The height evolution of the bridge at the point of coalescence for this period is given in Fig. 6.13. Before $t = 0$, the small constant values ($\mathcal{O}(10^{-4}$ m)) observed in each experiment are an artefact of the calibration, and signify a time when no fluid is present at this point in the medium. When coalescence begins to occur, a large rapid increase in height takes place. This increase is so swift that the time resolution of up to 120fps is not sufficient to deduce the growth rate. This rapid increase is observed to arrest when h reaches the bulk aperture value of the fractures on either side of the bridge. This is illustrated in Fig. 6.14(a), where a cross section in the x-z plane is plotted that intersects both the injection points and the position of coalescence. Inertia may be dominating the behaviour in this very early time regime, where no fracturing is taking place due to the absence of a barrier between the cavities, and the profile is just equilibrating out to the global bulk aperture value. A balance between inertia and the elastic forces may provide an appropriate scaling for this initial behaviour (De Maleprade *et al.*, 2016). The growth in height then slows to the power law behaviour that will be discussed in § 6.4.3.

Analysing the PIV information in the corresponding timescale for this rapid growth, we can see from Fig. 6.15 that a significant spike in the velocity of the internal fluid is also measured at the time of coalescence.

6.4.2 Elastic waves

If we analyse closely each set of data points in Fig. 6.14(a), we notice that from the centre of the fractures to the outer tips, the profiles at later times are very slightly smaller than those pre-coalescence. Thickness measurements at a particular point near the injection needle for experiment db12 is shown in Fig. 6.14(b). From this plot a dip in aperture is observed at the dashed line, which corresponds to the moment of coalescence. A similar dip is observed in every experiment systematically at the time of

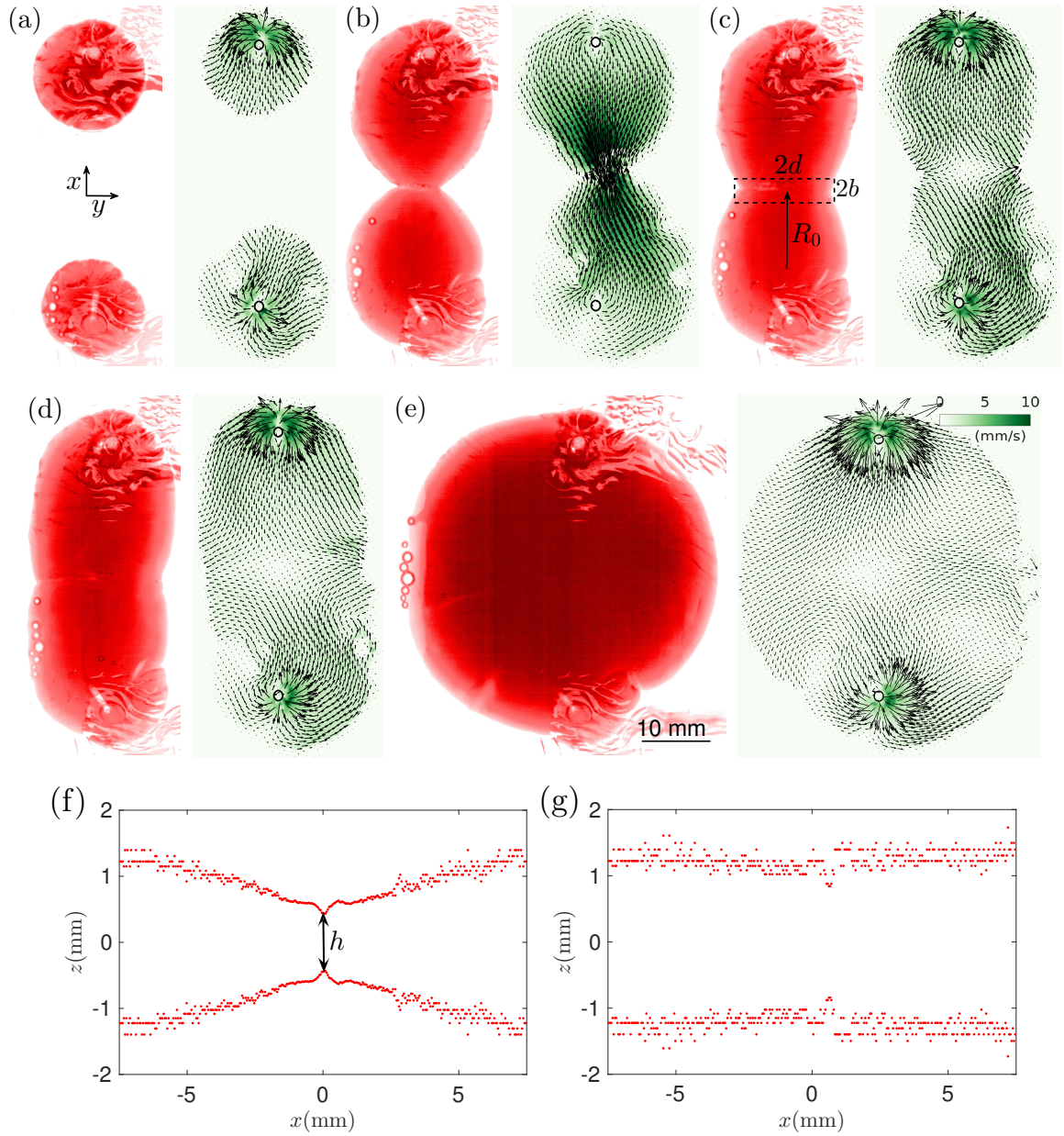

FIGURE 6.11: Time evolution of the coalescence process of two fractures: (a)-(e) top-view images and (f)-(g) side-view images. The time for each image is (a) $t = -6$ s; (b) $t = 0.01$ s; (c) $t = 0.8$ s; (d) $t = 2.5$ s; (e) $t = 21$ s; (f) $t = 0.04$ s; and (g) $t = 0.6$ s. The noise in **f** and **g** is an artefact of the calibration. Both light attenuation (db3) and PIV (pivdb13) measurements are employed (but not simultaneously for the same experiment), and in (a) to (e) we show the fracture thickness and velocity field at the same times from two repeated experiments at the same time. The distortion of light in the dyed images is due to the presence of injection tubes connected to the syringe pump. The colour bar of the PIV images correspond to the velocity magnitude, and values shown in (b) are 4 times larger than those in other top-view images.

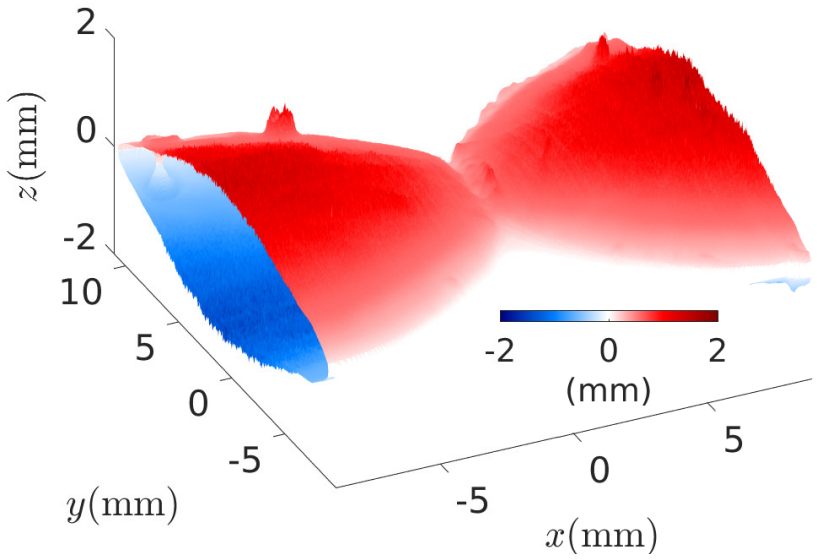

FIGURE 6.12: Three dimensional image of the bridge formed during the coalescence of two fractures in db3 at $t = 0.04$ s.

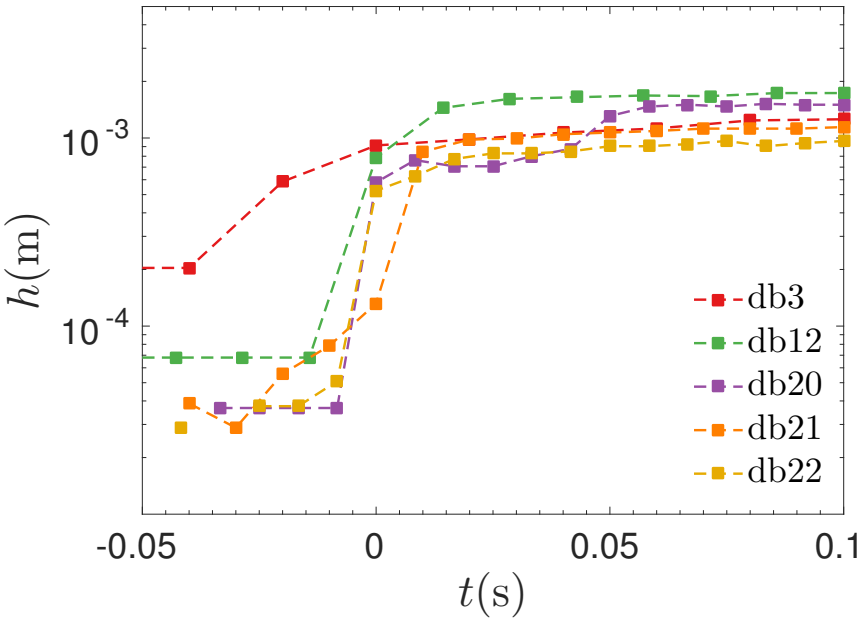

FIGURE 6.13: Evolution of the height of the bridge h at the point where the fractures coalesce and $t = 0$ is the moment of coalescence. Measurements shown before $t = 0$ s are below the experiment resolution

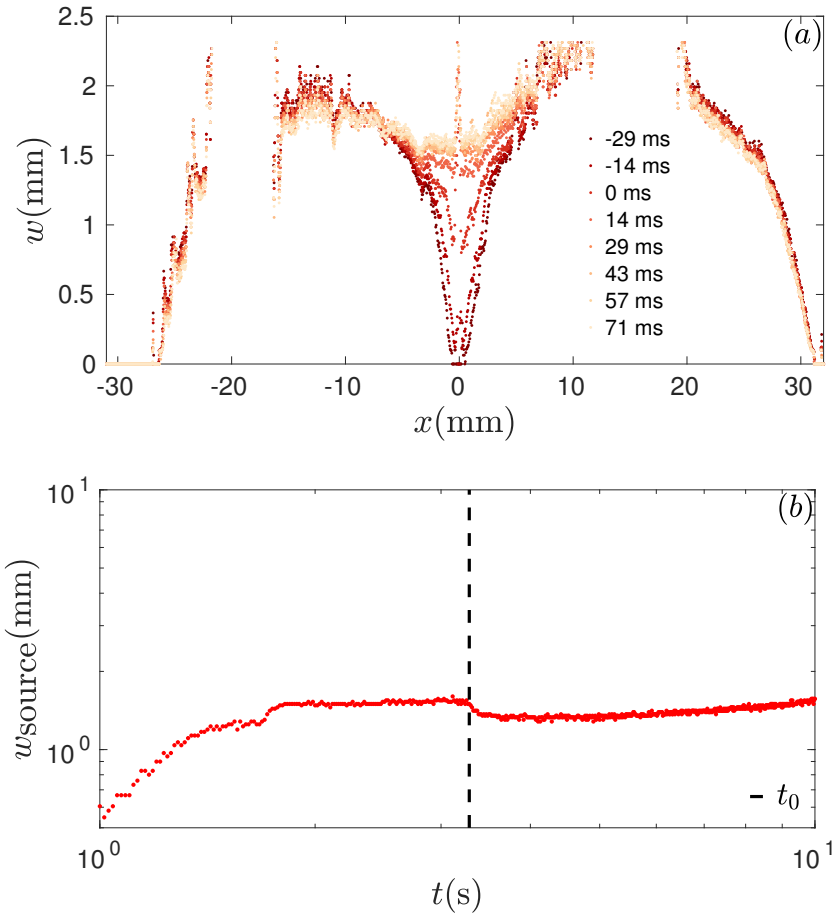

FIGURE 6.14: (a) x-z aperture profile w of the fractures around the time of coalescence (db12). Each set of data points correspond to the thickness values at a certain time, given in milliseconds. (b) Aperture values of a point located near the injection needle of a fracture versus time. The dashed line t_0 marks the moment of coalescence that coincides with a dip in the fracture aperture value near the fracture source.

coalescence. This is thought to be due to a possible elastic shear wave that is initiated by the response of the medium to a change in the distribution of fracture energies and the movement of fluid into the newly created bridge near the point of coalescence, where the height is equilibrated to the bulk value in the fractures pre-coalescence. The shear wave has a speed

$$V_s \sim \sqrt{\frac{G}{\rho_s}}, \tag{6.6}$$

where $G = E/2(1+\nu)$ is the shear modulus and ρ_s is the density of the medium. For typical values $E = 125$ kPa and $\rho_s \approx 1100$ kg m^{-3} (db12), $V_s \sim 6$ ms^{-1}. Thus, the time taken for this wave to travel 20 mm is approximately 3×10^{-3} s, which is within the timescale of the observed initial rapid growth. Therefore, we conclude it is possible that a shear wave is triggered at the moment of coalescence and leads to the levelling out of the aperture profile between fractures.

6.4.3 Bridge growth

The interface shape in the x-y plane motivates us to explore the possible universal behaviour for the growth of the bridge shortly after the coalescence of two fractures. In particular, we investigate the growth of the bridge length $2d$, employing a volume conservation argument (Ristenpart *et al.*, 2006). We consider a box around the bridge of volume V (Fig. 6.11(c)), with length $2d$, width $2b$ and height h. As the individual fractures are approximately circular, which was verified in § 6.3.4, geometry implies that

$$\begin{aligned} b &= R_0 - \sqrt{R_0^2 - d^2}, \ \text{ provided } d \gg b, \\ \Rightarrow b &= R_0 - R_0\sqrt{1 - \left(\frac{d}{R_0}\right)^2}. \end{aligned} \tag{6.7}$$

Then using a series expansion,

$$\begin{aligned} b &\approx R_0 - R_0\left(1 - \frac{1}{2}\left(\frac{d}{R_0}\right)^2 + \text{h.o.t}\right), \\ \Rightarrow b &\approx \frac{d^2}{2R_0}. \end{aligned} \tag{6.8}$$

Thus, the volume of this box is $V \approx 4dbh \approx 2d^3h/R_0$. The PIV experiments further illustrate that after a very brief initial increase, the flow rate into either side of the box

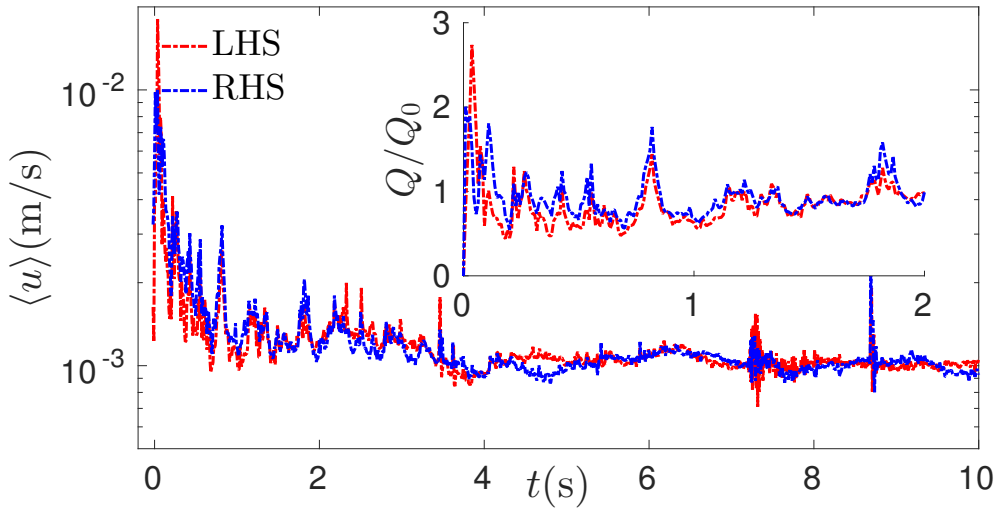

FIGURE 6.15: Measured velocity into either side of the bridge box as in Fig. 6.11(c) (pivdb13). Inset: a representative computed flux value into each side of the bridge box is constant and approximately Q_0, the imposed injection rate (see § 6.5).

settles to a constant value and is approximately equal to the imposed injection rate Q_0 (Fig. 6.15). This is due to the rest of the fracture not growing outside the bridge region. It follows that

$$\frac{\mathrm{d}V}{\mathrm{d}t} \approx \frac{2d^3h}{R_0 t} \approx 2Q_0, \tag{6.9}$$

which equals a mass balance relation for the bridge box. This provides the scaling relation for the length of the bridge,

$$d \approx \left(\frac{Q_0 R_0}{h}\right)^{1/3} t^{1/3}. \tag{6.10}$$

Note that the scaling relation equation (6.10) is based on a geometrical argument, dependent on the height h of the bridge, and does not include any dynamics. Consequently, we further assume that the bridge section can be approximated as a two-dimensional fracture, to obtain a relationship for the bridge height evolution with time.

For a two-dimensional fracture centred at $y = 0$, with edges at $-d(t)$ and $d(t)$, we define the net pressure $p(y,t) = -\sigma_z$. This pressure is related to the fracture aperture $h(y,t)$ by the integral relation (Spence & Sharp, 1985)

$$p(y,t) = -\frac{E'}{4\pi} \int_{-d(t)}^{d(t)} \frac{h'(s,t)}{s-y} \mathrm{d}s, \tag{6.11}$$

As before, the fracture propagation criterion $K_{\mathrm{I}} = K_{\mathrm{IC}}$ is based on LEFM (2.10). The mode I SIF for a two-dimensional fracture, which we will denote simply as K, takes the form (Rice, 1968)

$$K \approx p\sqrt{d}. \tag{6.12}$$

The fluid flow within this bridge can be modelled using the two-dimensional Sommerfield equation,

$$\frac{\partial h(y,t)}{\partial t} = \frac{1}{12\mu}\frac{\partial}{\partial y}\left(h^3(y,t)\frac{\partial p}{\partial y}\right). \tag{6.13}$$

This two-dimensional formulation assumes that fluid is injected at a point $y = 0$, rather than distributed along the bridge as a line source. This is a simplification of the actual physics within the fractures where counter flow exists, with a stagnation point at $y = 0$.

The boundary condition of the bridge is similar to that of the penny-shaped fracture, where there is zero aperture at the tip,

$$h = 0,\ y = d(t). \tag{6.14}$$

The mass balance for a two-dimensional fracture with constant flux $2Q_0$ is

$$\int_{-d(t)}^{d(t)} h(y,t)\mathrm{d}y = 2Q_0 t. \tag{6.15}$$

From the assumption that the bridge behaves as a two-dimensional fracture, (6.15) is equivalent to (6.9).

The bridge governing equations using elasticity (6.11), LEFM (6.12), lubrication theory (6.13) and a mass balance (6.9) form a set of equations that can be solved for $h(y,t), d(y,t)$ and $p(y,t)$. Equivalently to the single fracture case, two regimes of propagation, where material toughness or viscous dissipation is the dominant energy dissipation mechanism, are established.

6.4.3.1 Viscosity scaling

Combining elasticity (6.11), lubrication theory (6.13) and a mass balance (6.9), we can produce scalings for the viscosity regime. The order of magnitude of terms in these equations can be written as

$$p \approx E' \frac{h}{d}, \tag{6.16}$$

$$\frac{h}{t} \approx \frac{h^3}{\mu} \frac{p}{d^2}, \tag{6.17}$$

$$d \approx \left(\frac{Q_0 R_0 t}{h} \right)^{1/3}. \tag{6.18}$$

Re-arranging these relations, we derive the power law scalings for this regime,

$$d_{\mathcal{M}} \approx \left(\frac{Q_0^3 R_0^3 E'}{\mu} \right)^{1/12} t^{1/3} \tag{6.19}$$

$$h_{\mathcal{M}} \approx \left(\frac{Q_0 R_0 \mu}{E'} \right)^{1/4} \tag{6.20}$$

$$p_{\mathcal{M}} \approx \left(\mu E'^2 \right)^{1/3} t^{-1/3}, \tag{6.21}$$

where the subscript $\mathcal{M}$ on each variable denotes the viscosity regime. It is interesting to note from (6.19) that d grows more slowly than the radius of a single propagating fracture ($t^{4/9}$), and h is time independent in (6.20). The radial growth is deduced from a three-dimensional geometry, while here the bridge growth is modelled using a two-dimensional assumption.

6.4.3.2 Toughness scaling

Repeating this procedure by combining elasticity (6.11), LEFM (6.12) and a mass balance (6.9), we produce scalings for the toughness regime. Re-arrangement of (6.12), (6.16) and (6.18) provides the power law scalings

$$d_{\mathcal{K}} \approx \left(\frac{Q_0 R_0 E'}{K} \right)^{2/7} t^{2/7} \tag{6.22}$$

$$h_{\mathcal{K}} \approx \left(\frac{Q_0 R_0 K^6}{E'^6} \right)^{1/7} t^{1/7} \tag{6.23}$$

$$p_{\mathcal{K}} \approx \left(\frac{K^8}{Q_0 R_0 E'} \right)^{1/7} t^{-1/7}, \tag{6.24}$$

where the subscript $\mathcal{K}$ denotes the toughness regime. Again, from (6.22), we see that d grows more slowly than the radius of a single propagating fracture ($t^{2/5}$) and h has a very slow time-dependence in (6.23).

6.4.3.3 Transition

We can estimate the transition between regimes by analysing the relative importance of viscous and toughness related stresses. The toughness related stresses $\Delta p_{\mathcal{K}}$ are given by

$$\Delta p_{\mathcal{K}} \approx \frac{K}{\sqrt{d}}, \tag{6.25}$$

which can be found using (6.12). The viscous stresses $\Delta p_{\mathcal{M}}$ are deduced from (6.9) and (6.13) to have the form

$$\Delta p_{\mathcal{M}} \approx \frac{\mu}{t}\left(\frac{d}{h}\right)^2. \tag{6.26}$$

The dimensionless pressure ratio $\Pi = \Delta p_{\mathcal{K}}/\Delta p_{\mathcal{M}}$, can be used to establish the relative influence of viscosity and material toughness in bridge growth,

$$\Pi = \frac{\Delta p_{\mathcal{K}}}{\Delta p_{\mathcal{M}}} = \frac{K h^2 t}{\mu d^{5/2}}. \tag{6.27}$$

We can substitute either the viscous or toughness scaling laws from Table 6.2 into this expression. If we do this for the toughness case, $\Pi_{\mathcal{K}}$ has the form

$$\Pi_{\mathcal{K}} = \left(\frac{K^{24} t^4}{Q_0^3 R_0^3 \mu^7 E'^{17}}\right)^{1/7}. \tag{6.28}$$

If we also substitute in the viscosity scalings to find $\Pi_{\mathcal{M}}$, we find the following relationship between the pressure ratios Π,

$$\Pi_{\mathcal{K}} = \Pi_{\mathcal{M}}^{24/7}. \tag{6.29}$$

Thus, the viscosity and toughness scaling laws are valid when $\Pi_{\mathcal{M}} \ll 1$ and $\Pi_{\mathcal{K}} \gg 1$, respectively.

Similarly to the single penny-shaped fracture case in Chapter 2, the transition from a viscous to toughness regime can also be understood in terms of a characteristic timescale. This dimensionless timescale $t_{\mathcal{MK}}$ is obtained by setting $\Pi = 1$, and gives

Physical parameter	Viscosity($\mathcal{M}$)	Toughness($\mathcal{K}$)
Bridge length	$d_{\mathcal{M}} \approx \left(\frac{Q_0^3 R_0^3 E'}{\mu}\right)^{1/12} t^{1/3}$	$d_{\mathcal{K}} \approx \left(\frac{Q_0 R_0 E'}{K}\right)^{2/7} t^{2/7}$
Bridge height	$h_{\mathcal{M}} \approx \left(\frac{Q_0 R_0 \mu}{E'}\right)^{1/4}$	$h_{\mathcal{K}} \approx \left(\frac{Q_0 R_0 K^6}{E'^6}\right)^{1/7} t^{1/7}$
Net pressure	$p_{\mathcal{M}} \approx \left(\mu E'^2\right)^{1/3} t^{-1/3}$	$p_{\mathcal{K}} \approx \left(\frac{K^8}{Q_0 R_0 E'}\right)^{1/7} t^{-1/7}$

TABLE 6.2: Scaling expressions for bridge growth in viscosity and toughness-dominated regimes.

$$t_{\mathcal{MK}} = \left(\frac{Q_0^3 R_0^3 \mu^7 E'^{17}}{K^{24}}\right)^{1/4} . \tag{6.30}$$

The bridge propagates in the viscosity regime when $t \ll t_{\mathcal{MK}}$, and in the toughness regime when $t \gg t_{\mathcal{MK}}$. Once again, it is found that an increase in volumetric flux, elastic modulus and viscosity contributes to more viscosity-dominated fractures and increases in material toughness to more toughness-dominated propagation, as expected. Interestingly, a larger initial radius also contributes to more viscosity-dominated growth.

6.4.3.4 Bridge tip

The shape of the fracture tip along the bridge is also determined by the dominant dissipation mechanism. Similar to the single fracture case (§ 2.3), asymptotic estimates of the shape of the fracture tip can be deduced.

From Spence & Sharp (1985), the asymptotic shape of a two-dimensional fracture near the singularity at the tip has the form

$$h_{\mathcal{K}} \sim K(1 - y/d)^{1/2}, \quad \text{as} \quad y \to d, \tag{6.31}$$

for the toughness-dominated case, corresponding to an elliptical shape. For the viscosity-dominated case,

$$h_{\mathcal{M}} \sim (1 - y/d)^{2/3}, \quad \text{as} \quad y \to d. \tag{6.32}$$

It is noted that the shape of these asymptotes has the same form for the single fractures.

6.4.3.5 Results

The experimental measurements of the bridge length $2d$ for various parameters are plotted in Fig. 6.16(a). In these experiments we varied the distance between the fractures R_0, fluid viscosity μ, Young's Modulus E and fracture energy γ_s. For these particular parameters the bridge transition timescale varies between $8 \times 10^{-5} \leq t_{\mathcal{MK}} \leq 4 \times 10^{-3}$ (Table 6.1). The trends of the data in Fig. 6.16(a) show that the bridge length d exhibits a power law dependence on time. We rescale the raw data for d, based on the bridge scaling equation in the toughness regime (6.22), which leads to a convincing collapse onto a single curve in Fig. 6.16(b). The best fit line has a dimensionless pre-factor $\beta_1 = 0.81 \pm 0.04$, where

$$d_{\mathcal{K}} = \beta_1 \left(\frac{Q_0 R_0 E'}{K} \right)^{2/7} t^{2/7}. \tag{6.33}$$

This fit was measured from early times after coalescence, when $d \lesssim R_0$. Calculating the slope of the data gives a value of 0.30 ± 0.04 which agrees quite well with the expected value from (6.22) of $2/7 \approx 0.286$, within error bounds. At late times, the growth begins to transition to a $t^{2/5}$ behaviour expected from an isolated radial fracture, as discussed in § 6.4.4.

Similarly, we analyse the experimental data for the bridge height growth at the point of coalescence, as shown in Fig. 6.17(a). We measure h by using a 10 pixel average around the point of coalescence to smooth out any anomalous surface imperfections. We observe that h also has a power law dependence on time. Scaling the data according to (6.23) leads to a good collapse, as shown in Fig. 6.17(b). The best fit line has the form

$$h_{\mathcal{K}} = \beta_2 \left(\frac{Q_0 R_0 K^6}{E'^6} \right)^{1/7} t^{1/7}. \tag{6.34}$$

Fitting this form for early times of bridge growth, we obtain $\beta_2 = 2.6 \pm 0.2$. The slope of the data on the log-log plot has the value of 0.14 ± 0.03. This compares favourably with the expected time exponent from (6.23) of $1/7 \approx 0.143$.

The data collapse in both d and h, and the agreement of the fitting exponents, within error bounds, with the theoretical values (Table 6.2) indicate that we have successfully captured the initial bridge formation process during the fracture coalescence experiments.

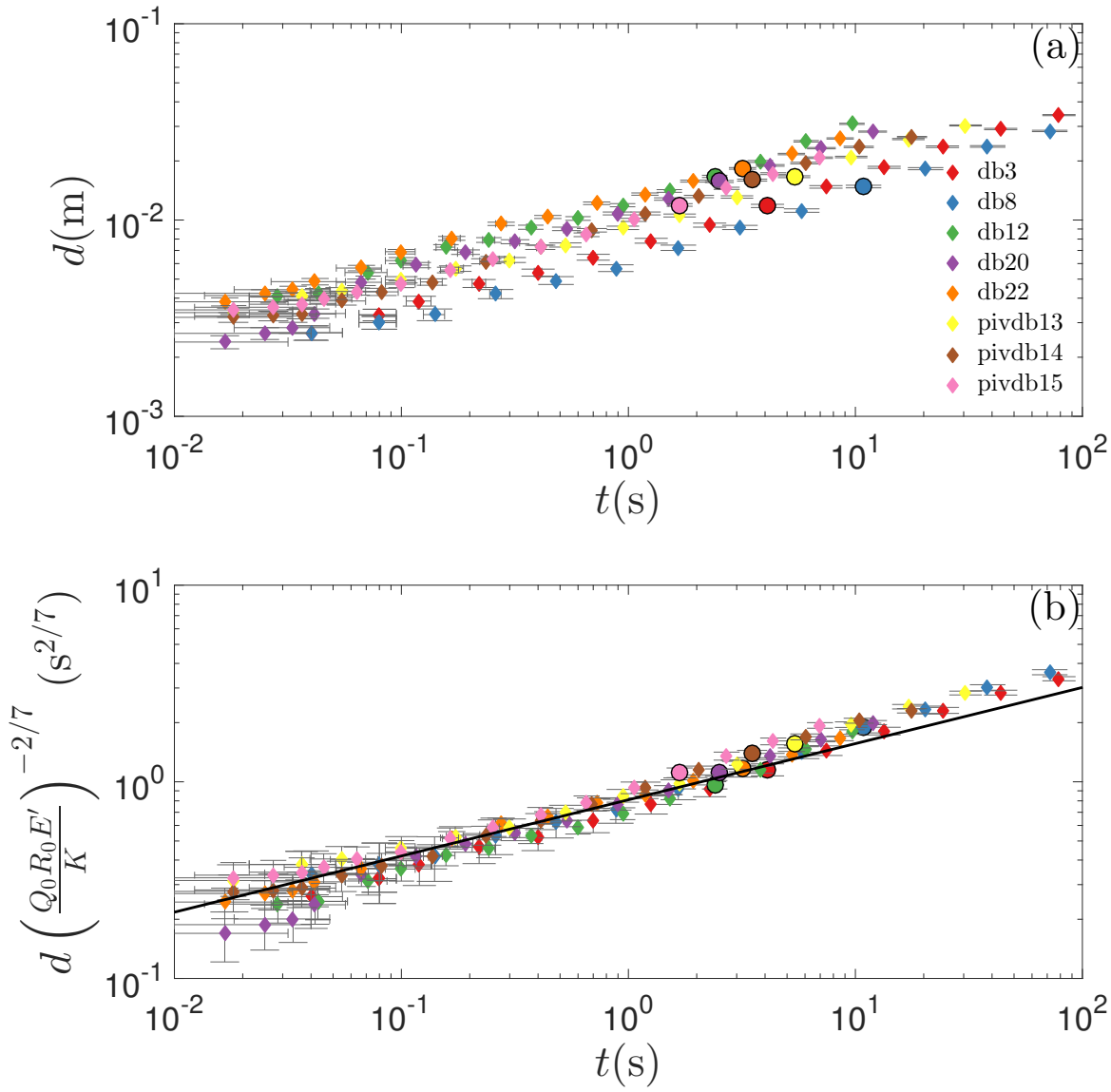

FIGURE 6.16: Experimental measurements of the half bridge length d as a function of time: (a) raw data of d; (b) rescaled data of d according to (6.22). The line represents the best fit to the rescaled data. The point where $d = R_0$ is labelled with a circular marker for each experiment.

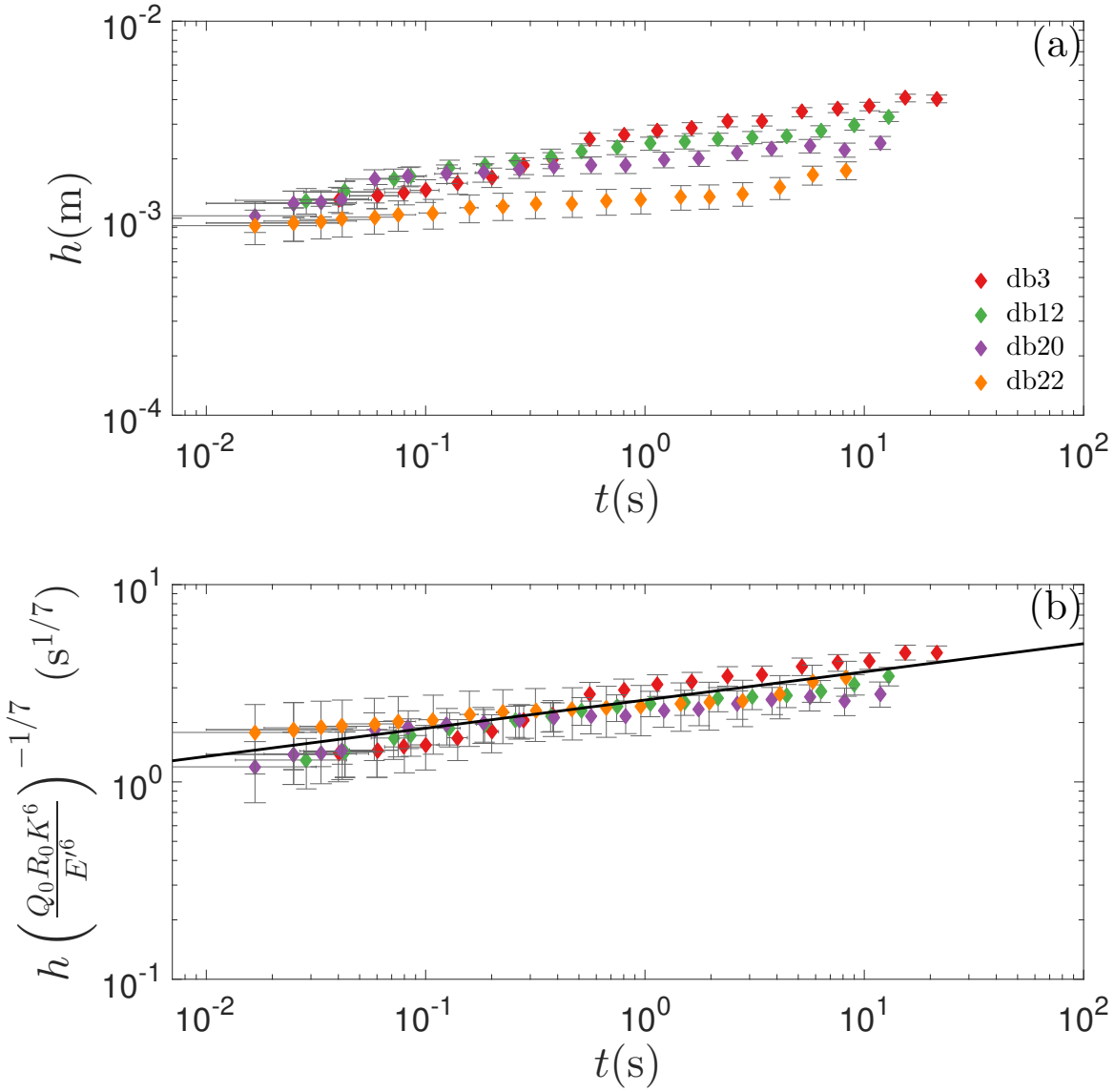

FIGURE 6.17: Experimental measurements of the bridge height h as a function of time: (a) raw data of h; (b) rescaled data of h using (6.23). The line represents the best fit to the rescaled data.

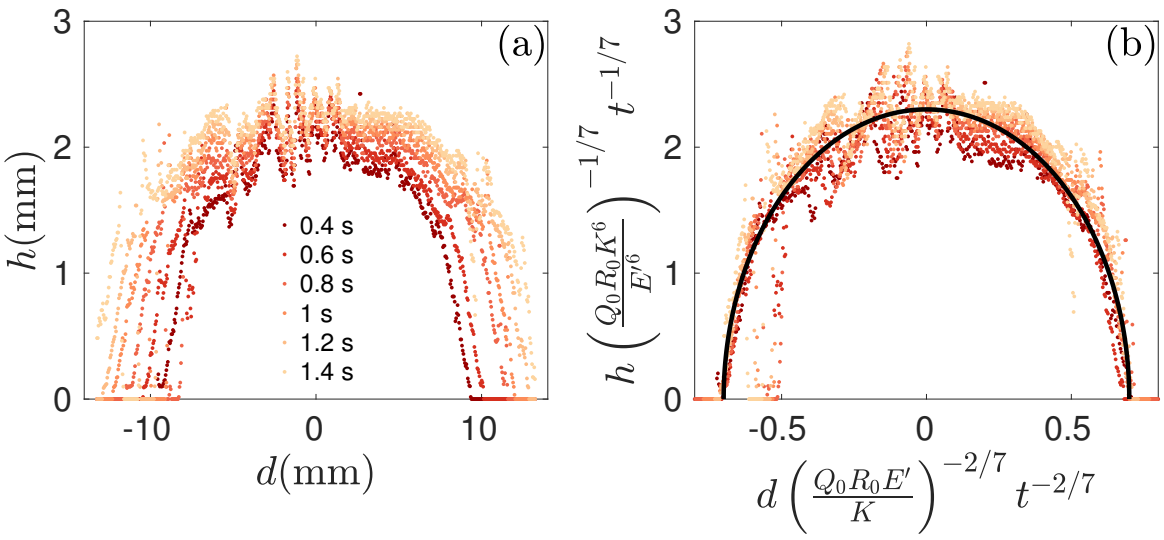

FIGURE 6.18: Experimental measurements of the time evolution of the bridge height profile h in the y-z plane (db12): (a) raw data; (b) rescaled data with time from (6.22) and (6.23). The rescaled bridge heights collapse to a universal profile which has an elliptical shape (bold line). The noise in the data is from surface roughness along the bridge.

Focussing on the height profile along the bridge in the y-z plane, we obtain profiles at various times, as shown in Fig. 6.18(a), for a sample experiment (db12). Using the height and length toughness power law time-dependences (Table 6.2), the thickness profiles at different times collapse to a single universal elliptical shape (Fig. 6.18(b)). This elliptic fit has dimensionless semi-minor and semi-major radii of 0.7 and 2.3, respectively.

This shape of the aperture profile along the bridge provides further evidence of material toughness being dominant at the tip. In Fig. 6.19, for a sample experiment (db22), the bridge shape is observed to follow the fitted toughness asymptote (6.31), and compares poorly with the expected viscous asymptote behaviour (6.32).

The time evolution of the profile shape in the x-y plane is further examined in this initial stage of coalescence in Fig. 6.20(a), where $d_s(x,t)$ represents the profile shape above the line $y=0$ connecting the injection points and hence, $d(t)=d_s(0,t)$. Profiles are plotted at various times after coalescence for a sample experiment (db3). The shape evolution also suggests a local universal behaviour. Rescaling the data using the geometric relationship (6.8) leads to good data collapse around the minimum (Fig. 6.20(b)).

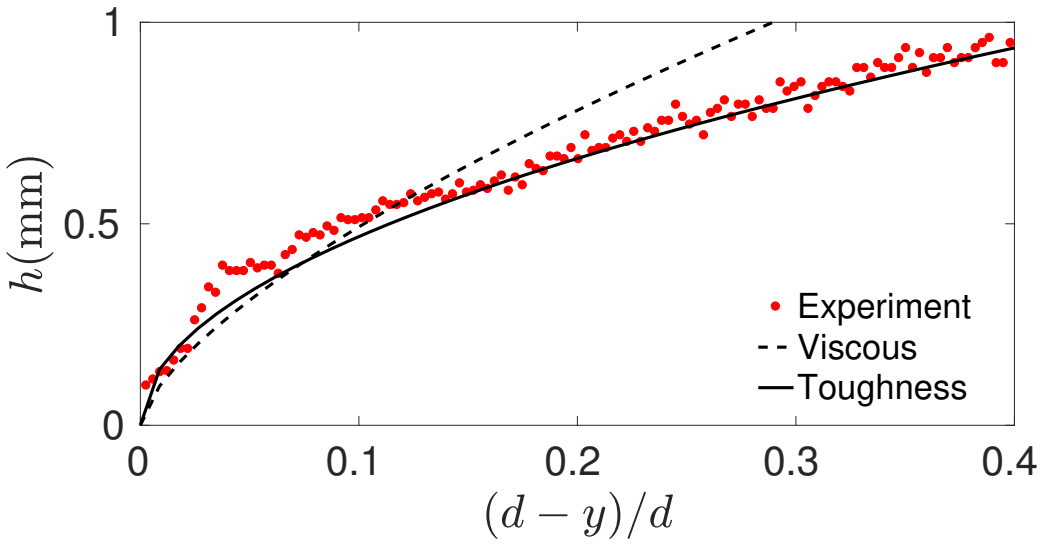

FIGURE 6.19: Bridge tip shape at $t/t_{\mathcal{MK}} \approx 1.6 \times 10^2$ (db22, $t = 0.63$ s), which follows the toughness asymptote (6.31).

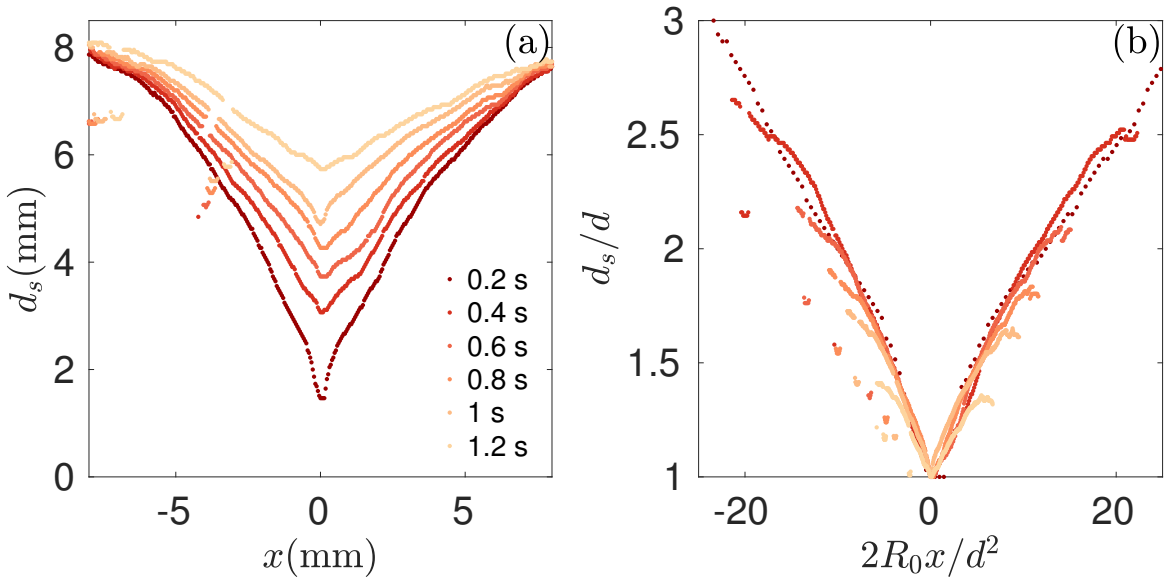

FIGURE 6.20: Experimental measurements of the time evolution of the fracture profile on the x-y plane following the coalescence of two fractures (db3): (a) raw data; (b) rescaled data. The rescaled profiles, according to $b \approx d^2/2R_0$, collapse to a universal shape near the minimum, which suggests a local self-similar dynamic behaviour during the coalescence of two fractures.

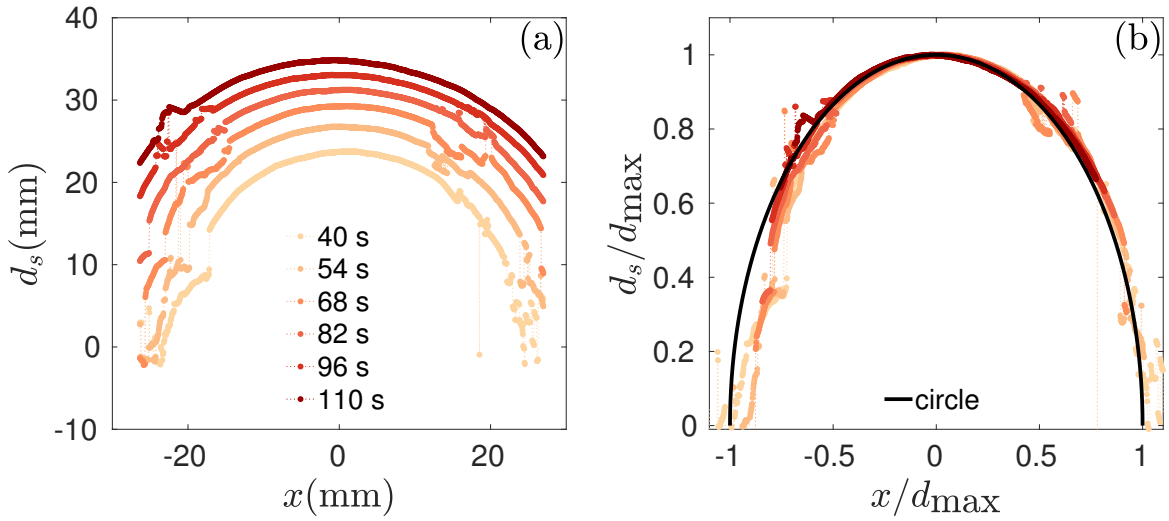

FIGURE 6.21: Time evolution of the fracture profiles at late times from a representative experiment (db3): (a) raw data; (b) rescaled data. The data collapse and agreement with a circular shape (bold curve) indicate that the two fractures already merge into a single fracture subject to a volumetric injection rate of $2Q_0$ in the toughness regime.

6.4.4 Late time growth

At very late times, the coalescing hydraulic fractures fully merge and propagate as a single penny-shaped fracture, which takes an elliptic shape as shown in Fig. 6.11(e) and Fig. 6.21(a). The front of the merged fractures transforms into a radial profile, which is demonstrated in Fig. 6.21(b), where the rescaled fracture profile takes the shape of a circle (the solid curve),

$$\left[\frac{d_s(x,t)}{d_{\max}(t)}\right]^2 + \left[\frac{x}{d_{\max}(t)}\right]^2 = 1. \tag{6.35}$$

We can analyse the transition to this single radial profile after coalescence. From empirical evidence, we observe that growth occurs along the x-axis connecting the fractures when the bridge half length d becomes comparable to $R_f = 2R_0$, the radius of the final fracture. If we consider the scaling of bridge length in the toughness regime (6.22), when $d = 2R_0$, the timescale t_f can be defined as

$$t_f = \frac{KR_0^{5/2}}{Q_0 E'}. \tag{6.36}$$

This can be used to rescale the data and determine the transition to normal single fracture growth. The time evolution of R_f is plotted in Fig. 6.22(a), where $t = 0$

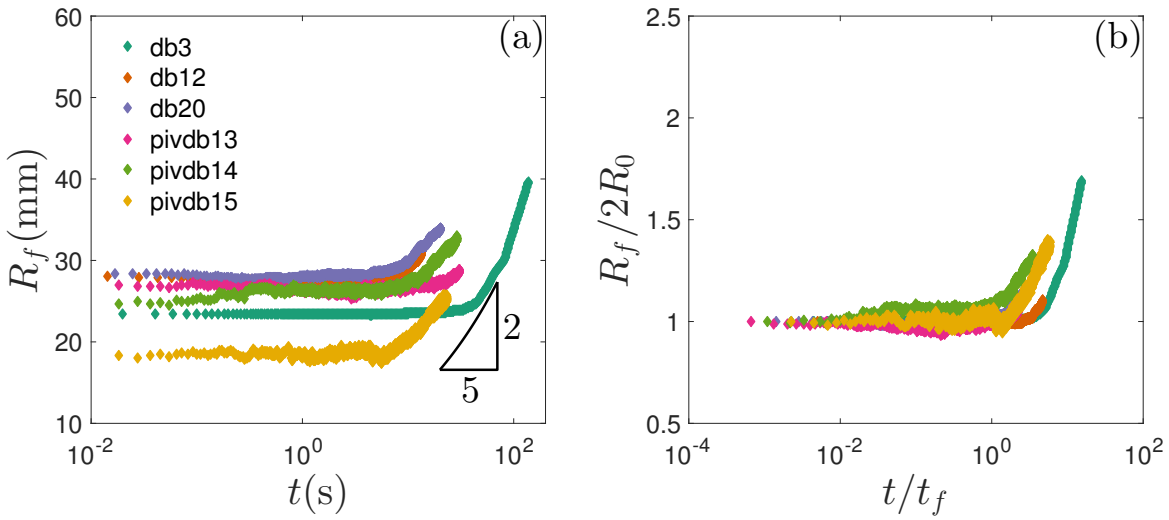

FIGURE 6.22: (a) Time evolution of the final fracture radius R_f. (b) Rescaled data using the dimensionless time t_f (6.36).

corresponds to the moment of coalescence. On first inspection, it is clear that R_f remains constant after coalescence until a certain point, when growth along the x-axis recommences. R_f can then be normalised by the initial radius and plotted versus the dimensionless time t/t_f (Fig. 6.22(b)). This results in the data collapsing onto a single curve, indicating that indeed full single fracture behaviour is achieved only when $d \geq 2R_0$.

This final single fracture propagates such that $R_f \propto t^{2/5}$ with injection rate $2Q_0$. However, the fracture extent at this late time encompasses nearly the whole gel matrix, and thus the effect of the boundaries cannot be neglected. When very close to the boundary ($\lesssim 5$ mm), the rate of growth can become considerably accelerated.

6.5 Velocity fields

The PIV measurements of the flow inside the fractures provide insights into the evolution of the fracture system. The qualitative behaviour of the internal flow field seen in Fig. 6.11 was briefly introduced in § 6.4. Here we will describe the properties of this internal flow field in more detail.

First, we analyse the component of the fluid velocity u_x along the x-axis connecting the injection sources. Fig. 6.23(a) shows the velocity profiles of two fractures pre-coalescence. In this figure the sources are clearly seen at $x \approx \pm 20$ mm and correspond to the maximum values of velocity. On either side of these points the velocity gradually

reduces until the fracture tip is reached. Towards $x = 0$, the advancing fluid front is clearly distinguished for each time-step and a sharp decrease is evident at the moving tip.

As the fractures move closer together, the strength of u_x near the advancing inner tip begins to increase, as seen in Fig. 6.23(b). This behaviour corresponds to the rapid growth just before coalescence, previously observed in Fig. 6.5. Approaching $t = 0$, the velocity near the inner tip becomes larger than near the source. This is mainly due to fluid being transported towards the inner tip from elsewhere in the fracture, because of the rapid attraction.

In Fig. 6.23(c), when coalescence occurs there is a significant increase in u_x, where the value increases by up to a factor of 4 compared to the pre-coalescence value. This increase can also be seen in Fig. 6.15 and coincides with the possible elastic wave and rapid h growth discussed in §§ 6.4.1 and 6.4.2. There is next an exchange between the flows originating from both sources around $x = 0$. As the left fracture is slightly smaller at the moment of coalescence, the velocity strength from that source is marginally larger near the inner tip. During the initial exchange of flow in the bridge region, this causes the stagnation point to be shifted towards the centre of the right fracture. After a short period of time the velocity begins to decrease, following the initial rapid growth, and the stagnation point returns to the point of coalescence.

At later times in Fig. 6.23(d), the strength of u_x is symmetric around the stagnation point and continues to decrease until a steady flow profile is established. This steady profile persists for the remainder of the experiment.

Furthermore, the y-component profiles of the velocity along the y-axis are given in Fig. 6.24. At early times after coalescence in Fig. 6.24(a) there is considerable variation during the initial exchange. In Fig. 6.24(b) a stagnation point at the position of coalescence is established and symmetric velocity profiles are observed. These profiles are stretched in the y-direction as the bridge connecting the fractures grow. Rescaling the y-direction of the velocity profiles u_y using the bridge length d, the profiles follow a similar trajectory.

Finally, we note that in Fig. 6.15 the representative flux Q is calculated using

$$Q \approx \langle u \rangle 2dh. \tag{6.37}$$

Since no measurements of h are available from PIV experiments, it was estimated using the experimental parameters and the pre-factor obtained from the fit in Fig. 6.17(b).

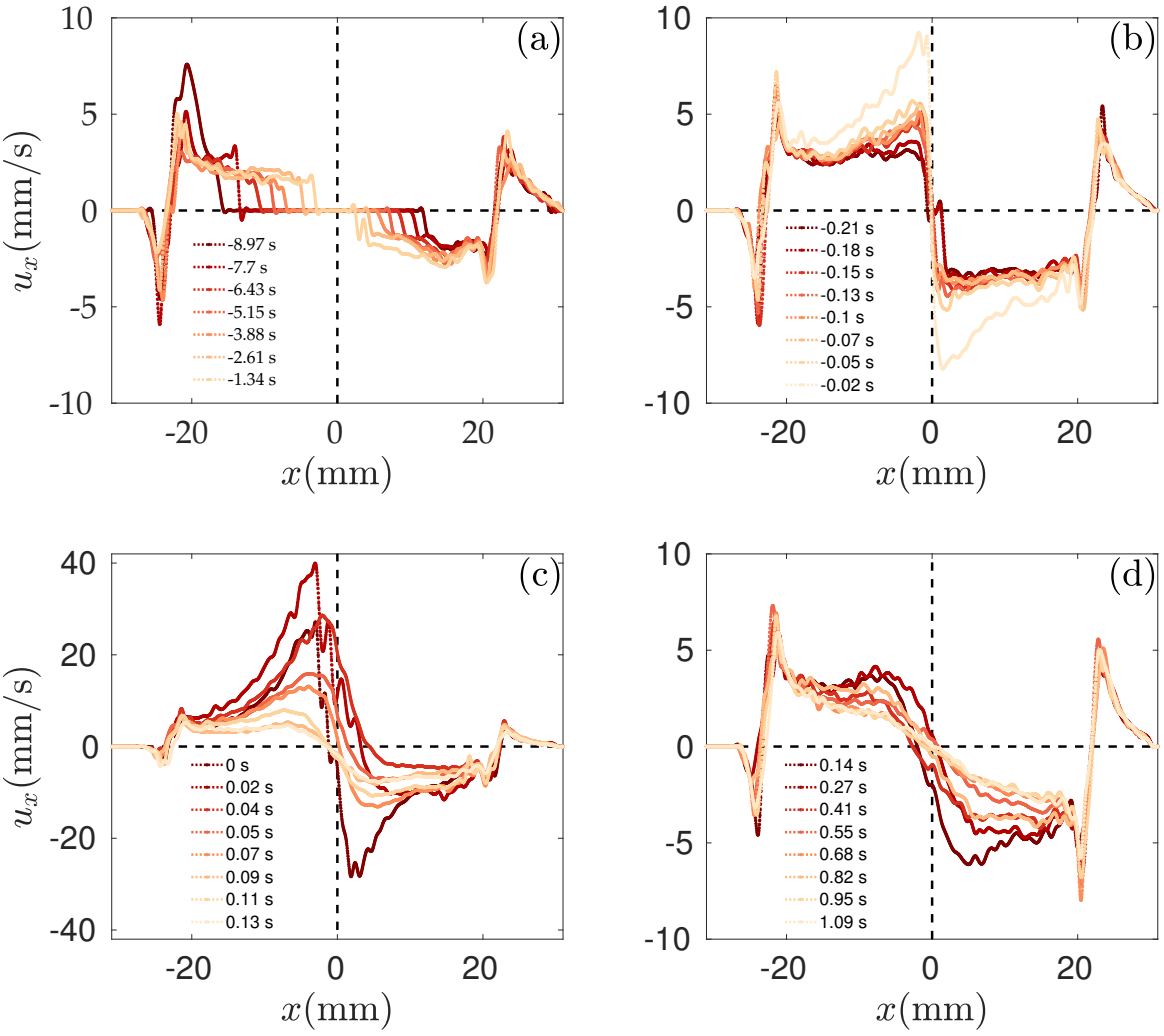

FIGURE 6.23: Internal fracturing fluid velocity u_x along the x-axis connecting the injection sources, for experiment pivdb13. The time $t = 0$ corresponds to the moment of coalescence.

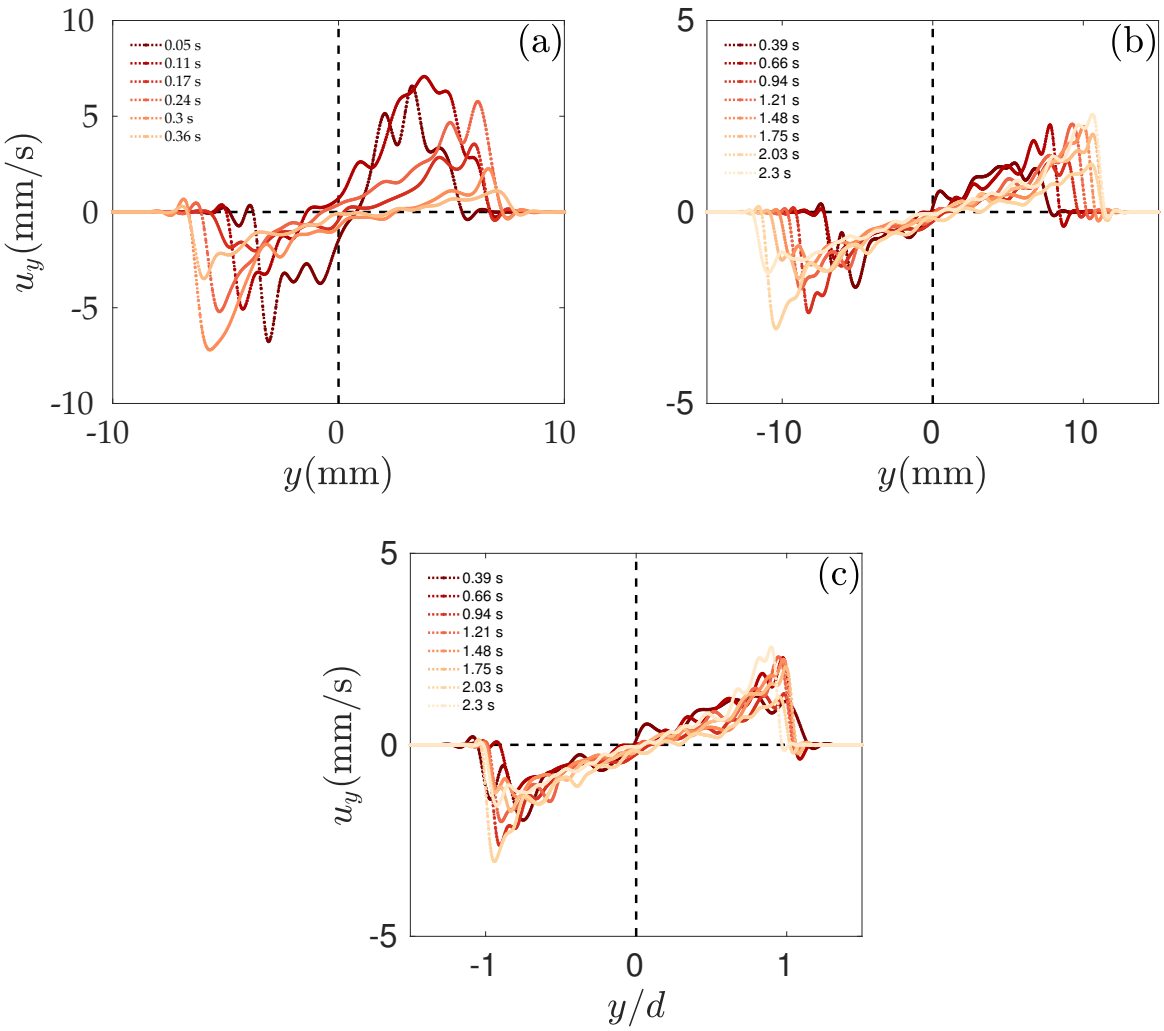

FIGURE 6.24: Internal fracturing fluid velocity u_y along the y-axis connecting the injection sources (pivdb13). The time $t = 0$ corresponds to the moment of coalescence. (a),(b) Raw y-component velocity profiles. (c) Scaled velocity profiles.

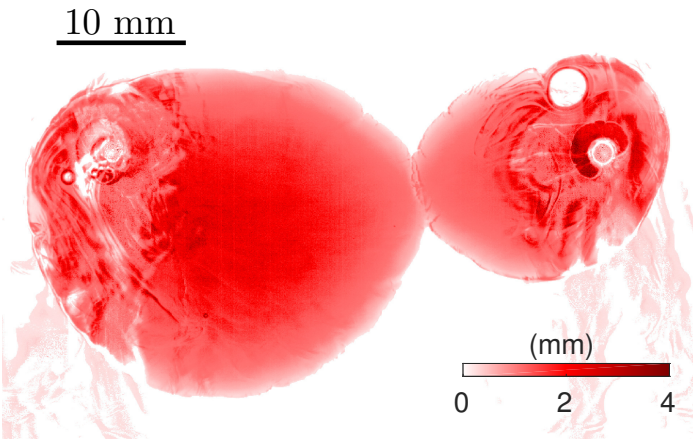

FIGURE 6.25: Asymmetric coalescence of two coplanar fractures (db6).

6.6 Asymmetric coalescence

Sometimes the offset, t_{off}, between initiations of the fractures can be quite significant. Subsequently, if t_{off} is sufficiently large, the size variation between the fractures at t_0 is also considerably large and $R_a \not\approx R_b$. An example of this sort of situation where asymmetric coalescence occurs can be seen in Fig. 6.25.

The fracture profile in the x-y plane in this type of experiment was examined in a similar fashion to that of the symmetric case (Fig. 6.20). The asymmetric fracture profile can be seen in Fig. 6.26(a). It is clear that as the fracture bridge evolves, the lack of symmetry introduces a horizontal displacement of the bridge position. The position of the bridge x_0 is moved towards the centre of the smaller fracture. The fracture profiles can be rescaled in Fig. 6.26(b) by centring the bridge at x_0, normalising d_s by d, and the x-axis by d^2 from the geometric relationship (6.8). This suggests that even in the asymmetric case there is a local universal behaviour of the fracture profile around the bridge minimum.

Fig. 6.27 shows the horizontal displacement generated by the absence of symmetry around the coalescence point. This evolves with a power law dependence on time of $t^{0.11}$. This corresponds to the difference in horizontal growth before coalescence and growth of the bridge after coalescence $t^{2/5}/t^{2/7} \approx t^{0.11}$. A similar type of asymmetric coalescence, with a linearly time-dependent horizontal drift, has been noted in spreading drops on a substrate in Hernández-Sánchez *et al.* (2012).

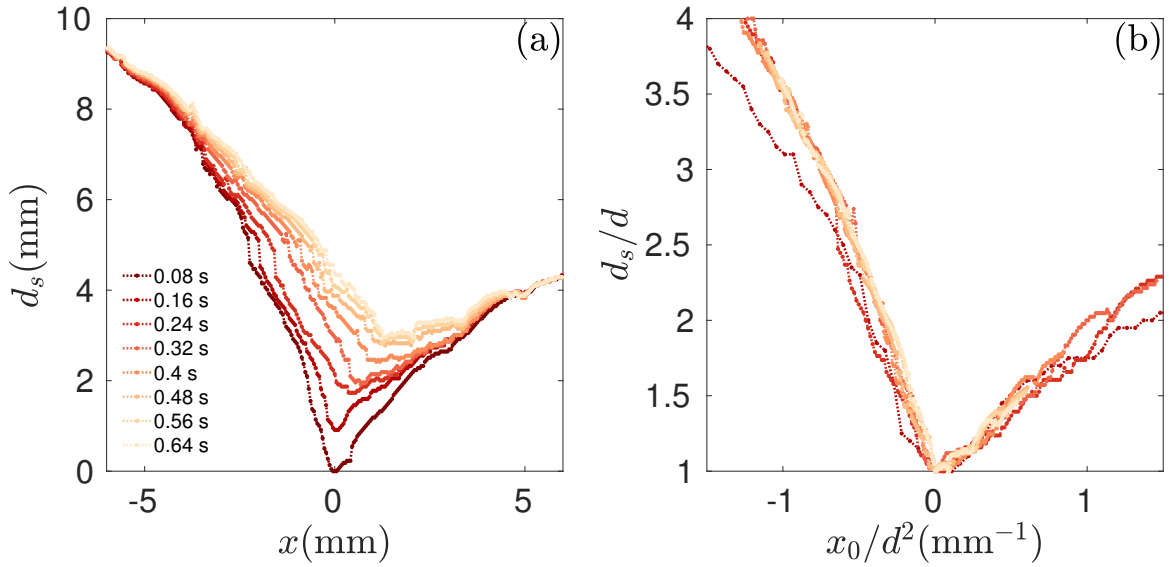

FIGURE 6.26: Experimental evolution of the fracture profile on the x-y plane following the coalescence of two fractures, where the left fracture (A) is larger than the right fracture (B) as in Fig. 6.25 (db6). (a) Raw data; (b) Rescaled data.

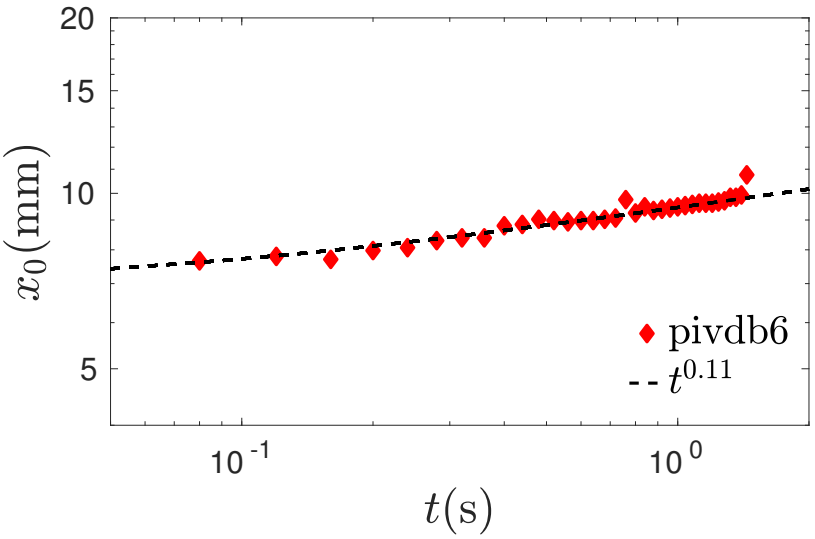

FIGURE 6.27: Moving position of the bridge tip x_0 in the horizontal x-direction after asymmetric coalescence (pivdb6).

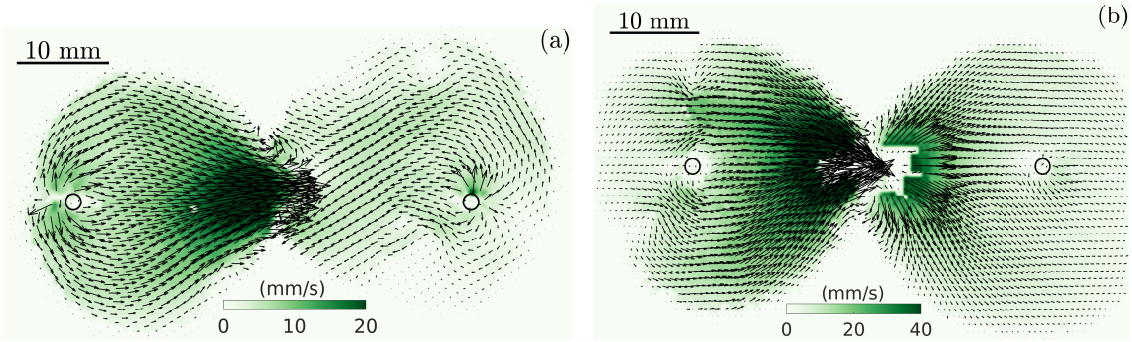

FIGURE 6.28: Velocity fields just after coalescence, when fluid intrudes from the smaller fracture into the larger: (a) $t = 0.036$ s (pivdb13); (b) $t = 0.117$ s (pivdb9).

6.6.1 Velocity fields

Asymmetric coalescence also causes a large change in the flow field of two coalescing fractures. Before coalescence the fluid in the smaller fracture will have a higher velocity near the inner tip than that of the bigger fracture, because the distance from the injection source is shorter. Therefore, when the fractures initially touch and fluid from both interact, the faster moving fluid is observed to intrude into the larger fracture in a shock-like manner, as seen in Fig. 6.28. In Fig. 6.28(b) we can see that the intrusion into the bigger fracture is large enough to reverse the direction of all the velocity vectors in the bigger fracture away from the point of coalescence.

We plot the horizontal velocity component u_x, along the line $y = 0$ connecting the injection points for experiment pivdb9 after coalescence in Fig. 6.29. As in the symmetric case, we can see a substantial increase in velocity near the point of coalescence when the fractures meet, compared to the velocity at the injection sources. The peaks of the velocity profiles around $x = 0$ could not be obtained, because the camera shutter speed (1/200 s) was not high enough to capture the movement of the particles in this region. In Fig. 6.29(a) it is observed that the velocity profiles between the sources increase in both wavelength and measured amplitude until $t \approx 0.117$ s, with all velocity vectors in the bigger fracture left of the source at $x = 0.02$ reversed from their original direction, as noted before. After this critical time, the wavelength and amplitude of this profile then reduces (Fig. 6.29(b)) until the steady state profile seen in the symmetric case (Fig. 6.23(d)) is established.

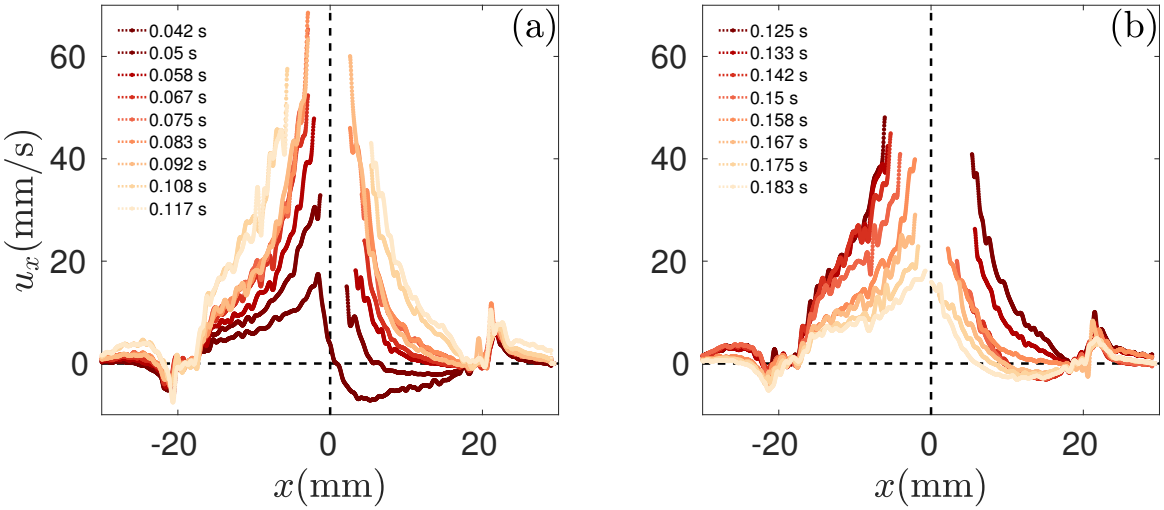

FIGURE 6.29: Internal fracturing fluid velocity u_x along the x-axis connecting the injection sources, for experiment pivdb9.

6.7 Non-coalescing fractures

Non-coalescing experiments occur frequently when the individual fractures are not properly aligned. An example of this phenomenon in both side and front elevation for two experiments can be seen in Fig. 6.30. This misalignment occurs due to small variations in the orientation of the fractures after initiation. In Fig. 6.30(a) it is apparent that the right fracture is oriented at a small angle to the horizontal. When the inner tips move closer together, they begin to interact and the tip shape is distorted (Fig. 6.30(b)). Growth in the tip region is observed to be concentrated in the z-direction of the inner tip away from the other fracture. This leaves a small pocket of highly stressed medium between the fracture tips. However, propagation in the direction of the other fracture ceases once a small overlap is established as in Fig. 6.30(b). This type of overlap is observed to occur when the sum of the orientations, that occur in opposing directions away from the horizontal, has the value $\theta \gtrsim 2.4°$.

After this small overlap develops, the fractures behave similarly to the coalesced case, with growth taking place solely along the y-direction where they overlap. In Figs. 6.30(c) and 6.30(d) the overlap can be seen in the front elevation view from the distortion of light near the tips. Furthermore, it is clear that coalescence does not take place when propagation continues along the overlap/bridge region, as the interface observed between the fractures is never smoothed out, unlike in the symmetric

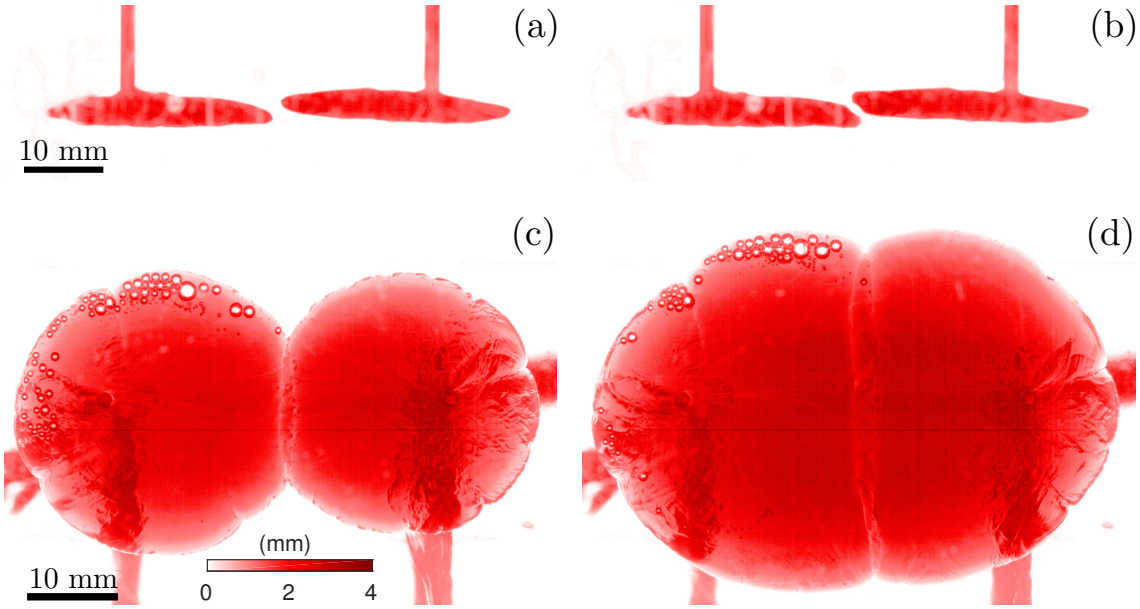

FIGURE 6.30: Side and front elevation images of non-coalescing experiments db30 and db23, respectively. (a) $t = 7.6$ s and (b) $t = 8.1$ s (db30). (c) $t = 9.5$ s and (d) $t = 13.1$ s (db23).

case (Fig. 6.11). An example of the difference between coalescing and non-coalescing fractures can be seen in side elevation view in Fig. 6.31.

In some cases, initially non-coalescing fractures were observed to interact after an overlap was present. This either took the form of a localised fluid intrusion between the fractures at some point in the overlap region along the y-direction, or at late times when the shape of the fractures together was approximately circular, they joined at the outer edges of the overlap region and propagated on the same plane. Examples of such experiments are shown in § A.2 of Appendix A.

6.7.1 Growth of the overlap region

Since the overlap region is observed to grow in the same direction as that of the bridge formed from coalescence, we can compare the growth of these as a function of time. In Fig. 6.32(a), the time evolution of half the extent of the overlap for numerous non-coalescing experiments, denoted by pentagram markers, is plotted. Alongside these measurements, bridge values of two sample coalescing experiments are also shown, denoted by the circular markers with black outlines. From this plot it is evident that the growth of the overlap region also exhibits a power law dependence on time, which

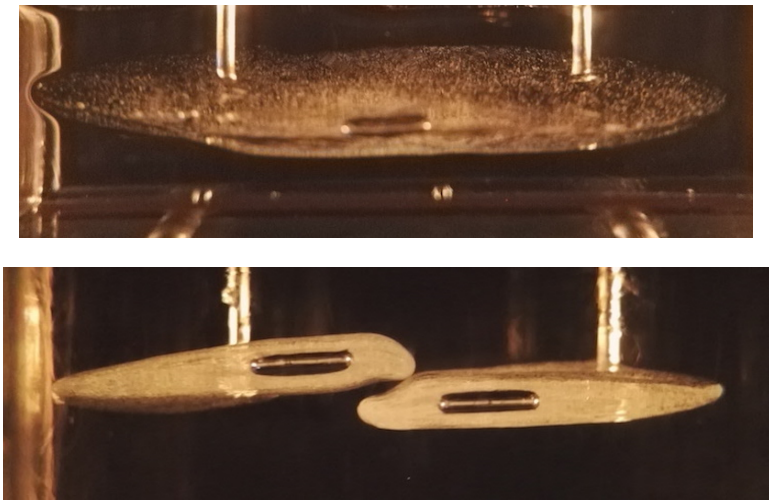

FIGURE 6.31: Comparison of side view images from coalescing and non-coalescing fractures.

has an exponent that is close to that of the bridge behaviour. Therefore, we rescale the data as before, using (6.22) to produce Fig. 6.32(b). At first this appears to provide a reasonable collapse of the data, with the data clustering together, albeit not exceptionally at early times. On closer inspection however, from fitting the rescaled data for the non-coalescing experiments when $d \lesssim R_0$ as in Fig. 6.16, we observe some variation. The best fit power law line has the same form as (6.33), with a dimensionless pre-factor of $\beta_3 = 0.68 \pm 0.08$ and exponent $\alpha_3 = 0.4 \pm 0.03$. This time exponent is notably higher than that of the bridge growth ($t^{2/7}$), and corresponds to the growth expected from a radial fracture propagating in the toughness regime ($t^{2/5}$, Table 2.1). The difference between the observed fits for both of these scenarios is demonstrated in Fig. 6.32(b). The collapse using the toughness bridge scaling is therefore perhaps not that surprising, when one considers that a similar dependence on Q, E and K is present in both expressions.

6.8 Ridge patterns

After each experiment the internal fracture surfaces were analysed as in Chapter 4. Once again, this revealed the formation of step-line surface patterns whose spacing is partly dependent on the particular gel properties, examples of which are seen in Fig. 6.33. However, the coalescence of fractures can cause an additional feature to appear on the surfaces. A ridge was usually formed along the direction of growth after

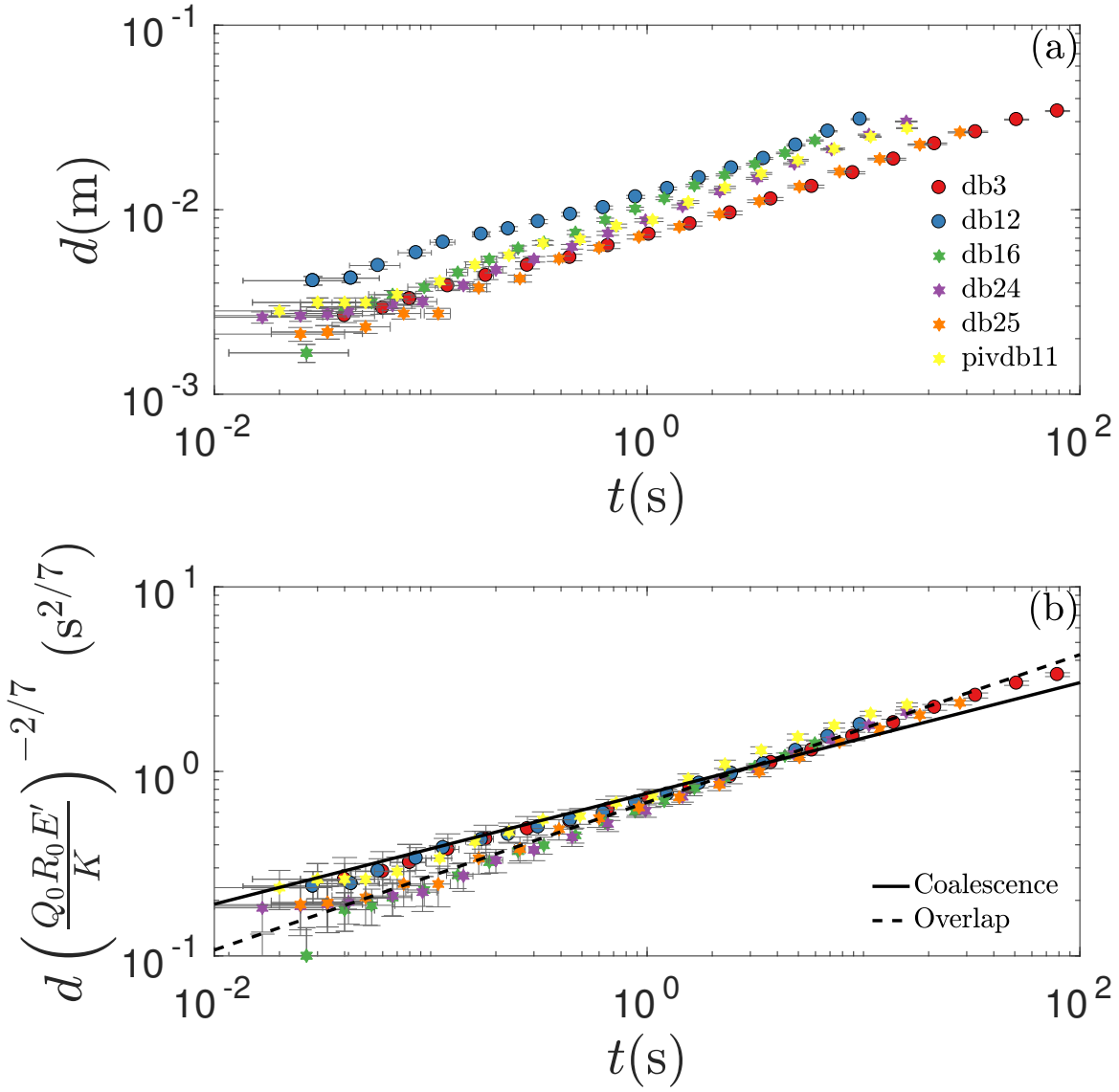

FIGURE 6.32: Experimental measurements of the half bridge length d for non-coalescing fractures as a function of time: (a) raw data of d; (b) rescaled data of d according to (6.22). Non-coalescing and coalescing experiments are denoted by the hexagram and black outlined circle markers, respectively. The dashed and solid lines represent the best fits to the rescaled data of the non-coalescing and coalescing experiments, respectively.

coalescence. It is believed this ridge forms due to imperfect alignment of the inner fracture tips at the moment of coalescence. This misalignment is small enough so that the fractures still coalesce and do not overlap, unlike as described in § 6.7.

In Fig. 6.33(a) the ridge is seen to follow an approximately straight line, perpendicular to a line connecting the injection sources. This surface corresponds to the symmetric coalescence experiment seen in the attenuation images of Fig. 6.11. Thus, the ridge is created at the point of coalescence and forms with the growth of the bridge. The ridge then eventually stops in the region where $d \gtrsim R_0$. This may be due to the fact that beyond this critical distance, propagation is no longer taking place between the fracture edges present pre-coalescence that are on slightly different planes, but is now fracturing an area of the hydrogel where the misalignment is no longer relevant. Similar ridges formed as a result of symmetric coalescence can be seen in Figs. 6.33(c) and 6.33(d).

For the case of asymmetric coalescence, an example of the post-experiment fracture surface is presented in Fig. 6.33(b). This corresponds to the experiment in Fig. 6.25 (db6) that was analysed in § 6.6. It is evident from these images that the curved ridge observed follows the horizontal displacement of the bridge towards the smaller fracture. The ridge also approximately ends where growth no longer occurred in the region between the fracture edges pre-coalescence.

In Fig. 6.34(a) the resultant surface of an experiment with two fractures of different sizes is seen, where the right fracture is initiated first, and is hence larger. Initially, the fractures approached each other and did not coalesce. Propagation was then seen to follow the curved ridge shape that separates the edges of both fractures. However, at an intermediate time after the overlap of the inner tips, fluid was observed to intrude from the smaller fracture into the larger near the point of initial overlap, marked by the two dark regions in the centre of the image. Thus, the fractures eventually interacted but were only connected through these regions, and the ridge shown marks the separation that existed between them.

In Fig. 6.34(b) the ridge of a symmetric non-coalescing experiment is shown. This corresponds to the side elevation images Figs. 6.30(a) and 6.30(a), where the fractures never touch, and the ridge separates the fractures along the y-axis at the point of initial overlap.

Other initially non-coalescing fractures that interact at late times, where a fluid interface develops at the outer edges of the ridge region along the y-axis, exhibit a ridge on the surface until this point.

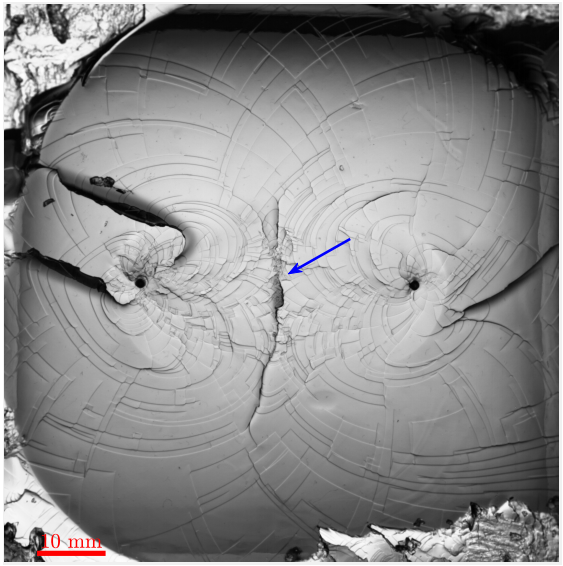

(a) 10 - 2.5% (db3)

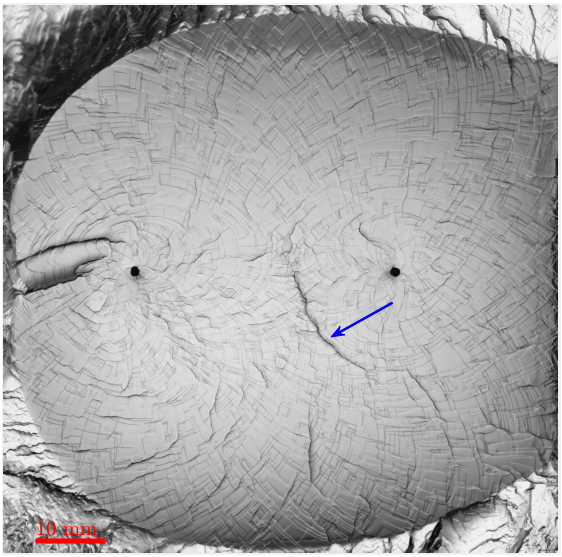

(b) 10 - 4% (db6)

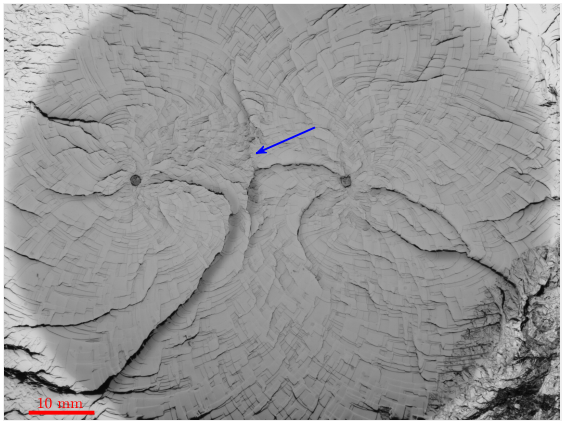

(c) 10 - 4% (db21)

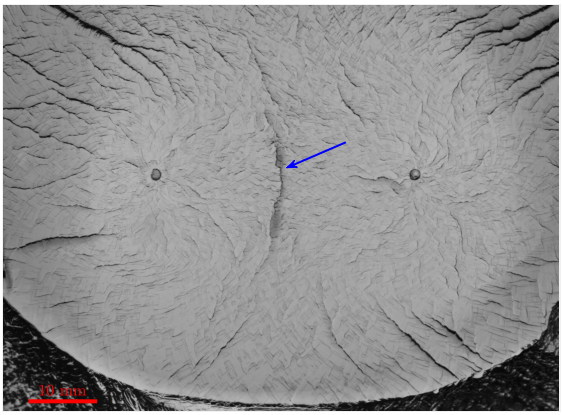

(d) 13.3 - 6% (db22)

FIGURE 6.33: Step-line patterns created due to the coalescence of two coplanar radial fluid-driven fractures. The ridge formed in each image is marked with a blue arrow.

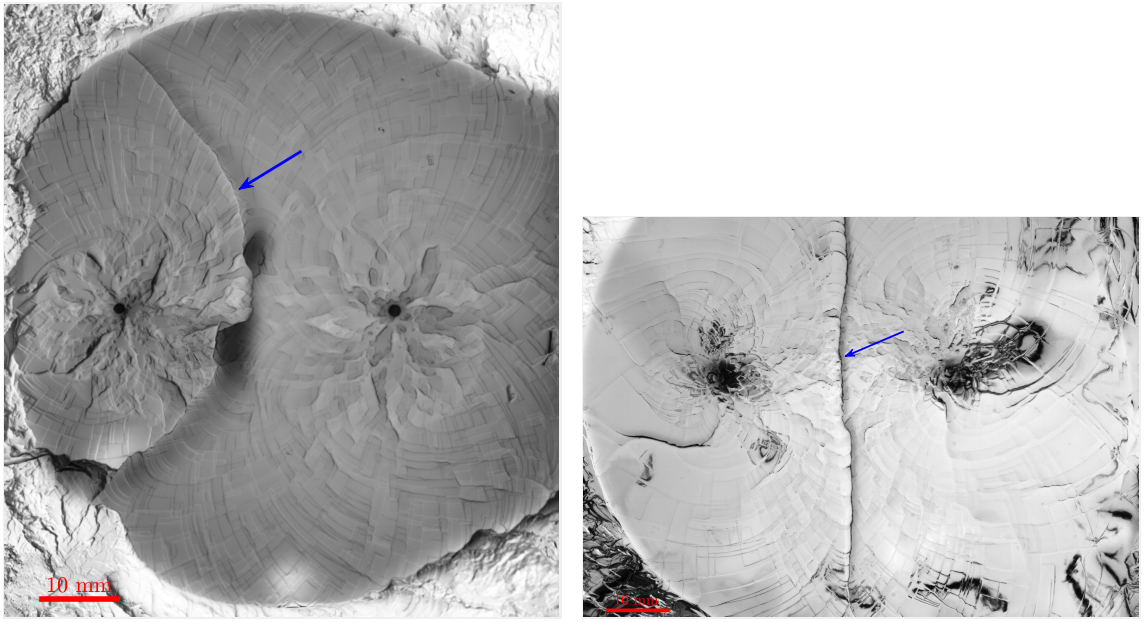

(a) 10 - 4% (db2)

(b) 10 - 2.5% (db30)

FIGURE 6.34: Step-line patterns created due to: (a) Asymmetric interaction and (b) non-coalescence. The ridge formed in each image is marked with a blue arrow.

6.9 Conclusions

In this chapter, we have introduced dual-fracturing experiments which permit the propagation and coalescence of two coplanar fractures. We first analysed the stress state and SIFs that result from the presence of two fluid cavities within a medium, which can have a significant effect on the direction of growth. Following this, we investigated propagation of the two fractures, pre-coalescence. The radial and aperture measurements were rescaled in the toughness-dominated regime, in a similar way to the single case, by accounting for the drift of the fracture centre. Once more, the experiments provided good agreement with the theory. We also observed the shifting of growth from the outer to inner tips of the fractures due to the SIF values. Additionally, we examined the separation distance between the fractures and how the variation in SIFs and offset times affected its reduction.

Once the inner tips become sufficiently close, they interact and coalesce, forming a narrow bridge between the fractures. The initial stages of this coalescence cause rapid growth in the height of this bridge, and the possible existence of an elastic wave. Thus, the bridge height is equilibrated with that of the bulk value in the fractures. All growth is then observed to occur in the narrow bridge connecting the fractures. Scaling laws

were constructed for the growth of this bridge using a two-dimensional approximation and a volume conservation approach. This provided power law relations for length, height and pressure as a function of time of the bridge in two regimes, where viscosity or toughness are the dominant energy dissipation mechanisms. A transition timescale $t_{\mathcal{MK}}$ between the regimes was also constructed. The toughness regime case was then verified with experimental measurements, and PIV techniques were implemented to verify the main assumption that the flux into the bridge region is approximately equal to the constant injection rate $2Q_0$. The PIV measurements provide more insights into the dynamics of coalescence, particularly the presence of large velocities in the bridge region corresponding to early time rapid growth and the subsequent formation of a stagnation point near the centre of the bridge. Perhaps most importantly, analysis of the profile shapes in both the x-y and y-z planes suggest the existence of universality in the bridge formation process. Lastly, at late stages of coalescence when growth spreads to the entire envelope, a timescale at which growth will transition back to the single fracture behaviour was created.

A variation of the original experiment involves the coalescence of two fractures of unequal size. We note that this asymmetric coalescence also exhibits a local universal behaviour of the x-y profile around the bridge. The absence of symmetry introduces a horizontal displacement of the bridge, and asymmetric coalescence can cause a substantial shock-like intrusion of fluid into the larger fracture.

Another extension of the dual-fracturing problem arises when the fractures are misaligned, by an angle $\gtrsim 2.4°$, thus inhibiting coalescence. As the inner tips approach each other, they can become distorted and curved, forming an overlap that leaves a small pocket of medium between the fractures. When the stress state of the gel is still comparable to that of the coalesced case, growth develops along the overlap in the y-direction as before. Thus, although coalescence does not occur, the behaviour of the two cases are comparable, because ultimately the stress state and material toughness are dominating the dynamics. We observe that the growth of the overlap region has a larger power law time-dependence than that of the coalesced bridge, which is comparable to the growth of an isolated radial fracture.

We finally comment on the topography of the internal fracture surfaces that exhibit step-line patterns. However, with two fractures present, a ridge is observed to form when they interact, with the direction and length of this ridge dependent on whether they coalesce symmetrically, asymmetrically or overlap.

The work in this chapter provides a first effort to probe the dynamic formation of a fracture network and the interaction of propagating fractures with one another. This type of behaviour is crucial in understanding the complex mechanisms involved in real-world applications, where branching of fractures occurs and multiple natural fractures may exist in the medium, which can ultimately lead to coalescence or overlapping of fractures.

Chapter 7

Conclusions

7.1 Review and implications

In this thesis we have studied multiple aspects of fluid-driven fractures in an elastic medium.

Throughout Chapters 3 and 4 we described the novel experimental setup and methods that were involved in implementing the fracturing experiments. From this we showed that polyacrylamide hydrogel is an excellent medium in which to study fluid-driven fractures, due to its wide variety of material parameters, complete transparency and versatility. These gels provide a very useful analogue for fluid-driven fracturing studies from which accurate measurements can be easily obtained as well as a wide variety of material properties. The experimental methods presented here provide a good basis for further studies to build upon and explore more complex fracturing events similar to real-world problems. Moreover, we found that the fracture surface of the hydrogel exhibits fractal spiral step-line patterns, whose spacing depends on gel concentration and fracture velocity. The fractal dimension values for these patterns were calculated and may allow comparisons with future geological field observations.

In Chapter 5 we examined the results of experiments with an isolated penny-shaped fluid-driven fracture. Using both attenuation and PIV methods, measurements of fracture radius, aperture and fluid velocity provided significant amounts of data with which to validate existing theoretical scalings. Time-dependent scalings of radius and aperture growth, as well as fracture tip asymptotes in viscosity and toughness-dominated regimes were verified. However, a discrepancy between experimental results and theory was identified for the radial viscous scaling pre-factor. These scalings are crucial in order to identify regimes of propagation and estimate the importance of parameters

Parameter	Range
Q (m^3/s)	0.01-0.08
E (GPa)	7-40
ν	0.15-0.4
μ (Pa·s)	0.001-1
K_{IC} (MPa $m^{1/2}$)	0.5-2

TABLE 7.1: Typical hydraulic fracturing parameters (Savitski & Detournay, 2002).

in particular scenarios. Therefore, the experimental exploration and verification of scaling laws is an essential part of accurately modelling fracture propagation. Since the injection timescales involved in a hydraulic fracturing operation can last several days, it is imperative that the correct regime of propagation is predicted in order to provide a good estimate for fracture extent, which can vary significantly between regimes over large timescales. Using typical hydraulic fracturing parameters, as given in Table 7.1, the transition timescale t_{mk} can range from 10^{-3} - 10^{16} s. Thus taking average values, most industrial operations will propagate in the viscous regime and propagate significantly further than toughness-dominated fractures even though the power law dependence is similar due to the large timescales involved. Furthermore, the PIV measurements discovered the existence of two distinct types of flow within a fracture. Radial axisymmetric flow was observed in the viscosity regime as expected, but more disordered flow with circulation was discovered in some toughness-dominated experiments. This will have implications for the transport of proppants throughout a fracture system and may affect the performance of an industrial operation, as the flow can circulate within fractures. Estimates for the Reynolds numbers in these operations varies widely depending on fluid viscosity and assumptions about the fracture shape and aperture (Dontsov, 2016; Zolfaghari *et al.*, 2017), with turbulent flow sometimes predicted near the inlet of a wide fracture and laminar flow developing closer to the tip region. However, laminar flow is expected in most operations, particularly away from the source and in fracture networks, which can have spacings of $\mathcal{O}(0.1$ m) and height/width aspect ratios of 1000:1 (Bazant *et al.*, 2014; Gale *et al.*, 2007).

Finally, in Chapter 6 we introduced a dual-fracturing experiment designed to study the propagation and coalescence of two coplanar fluid-driven fractures. As mentioned at the start of this thesis, fluid-driven fracturing operations are expected to form fracture networks. Within these networks, fractures interact with one another and interactions may have a considerable impact on the network evolution and final structure. By

analysing the complete time evolution of two idealised penny-shaped fractures we have gained new insights into how they interact with one another and how attraction may occur between them. Initially, when both fractures propagate, preferential growth is established in the direction of the other fracture, due to the evolving stress state in the medium. Accounting for drift of the fracture centre, radial and aperture behaviour is described well by theoretical scalings for isolated growth. If fracture tips coincide on the same plane, coalescence will occur and a bridge forms near the point of initial contact where growth is localised. Then a rapid growth in height and large increase of flow into this region occurs initially to equilibrate the bridge height with the bulk values in the original fractures. Time-dependent scalings for the growth of the bridge were developed, which identified two regimes of growth, viscosity and toughness-dominated, and a transition timescale between them. Experimental measurements then verified toughness scalings for bridge extent and aperture. Moreover, the profiles created around the merging point during coalescence exhibit a local universal behaviour until late times when growth transitions back to single fracture behaviour. In this chapter we also briefly analysed the case of asymmetric coalescence where the absence of symmetry induces a horizontal displacement of the bridge and fluid intrusions from the smaller to larger fracture exhibit shock-like behaviour. We have also shown that if the fractures are slightly misaligned, as may be more common in real-world scenarios, the tip shape can become distorted and a small overlap will occur with growth localising along this region similar to coalescing fractures, however the growth rate is different and comparable to a single fracture. This observation is very important and suggests that slight misalignment will considerably impact how inter-connected a fracture network may be. Other aspects of coplanar fracturing that we experimentally observed were partial coalescence after initial misalignment of the fracture tips and ridges formed on the hydrogel surface at the position where fractures coalesced where alignment was dependent on the type of interaction.

The results of Chapter 6 may be used to predict the behaviour and future fracture extents in the coplanar configuration. Additionally, the results contained here may inform numerical simulations that model fracture merging events, and verification of numerical methods may be done by comparison with the experimental and theoretical results presented. If we assume the spacing between fractures in industrial applications can vary between 0.1 m for a dense fracture network and 150 m for long single fractures, the transition time $t_{\mathcal{MK}}$ can range from 10^{-3} - 10^{12} s. Therefore, similar to the single fracture case it might be expected that the growth of the bridge section of most

coalescing events will be viscously dominated. However, for other scenarios that occur on smaller scales, such as in cells and tissues, coalescence may be toughness-dominated.

7.2 Future work

There are many avenues for future research, for which this thesis has already laid significant ground work.

Further theoretical work: This thesis has uncovered many surprising experimental results that are not fully explained by theoretical models. These include the spiral step-line patterns observed on the fracture surface, circulation of fluid within toughness-dominated fractures, a different viscosity-dominated scaling pre-factor, asymmetric coalescence and the interaction between non-coalescing radial fractures. Further theoretical work to model these experimentally observed phenomena would provide significant new insights in this area.

Stratified and heterogeneous media: Stratified or gradient gels may be synthesised relatively simply using the standard double-bucket filling method. This would enable experimental exploration of layered formations which are common in the subsurface. Also, growth of fractures into a layer with higher *in-situ* stresses could be investigated. Furthermore, structures can be set within a gel to simulate heterogeneous barriers that fractures cannot propagate through.

Interactions with natural fractures: Natural fracture systems could be created by synthesising a number of gels separately with different moulds, and then using an adhesive with a lower fracture energy to attach them together. This would accurately capture the behaviour along rock joints within formations, where fracture energy values are reduced.

Experimental measurements: Index-matched particles can be distributed uniformly throughout a hydrogel matrix. Using laser scanning, the displacement of these particles can be measured. Hence, the stress around a propagating fracture can be obtained. Light polarisers could also be used to take advantage of the photoelastic properties of the gel, in order to determine stress values.

Permeable media: Fluid-driven fractures propagating in a permeable medium is another important case that has been less experimentally studied. In this situation fluid leak-off and poroelasticity affect fracture propagation and orientation.

Complex fracturing fluids, slurries and variable injection rates: Fluid in many natural and industrial processes is not Newtonian. Thus, complex fluids should be used in order to accurately document these fractures. In addition, when proppants are added, the resulting slurry that forms has different rheological properties from the original fluid. This changing rheological behaviour and the transport of proppants throughout a fracture system are areas in need of more research. Finally, variable injection rates is another topic of immense interest. An injection scheme may be devised to increase well production and/or reduce water consumption. This may also describe natural fluid-driven fractures more accurately, where there can be a limited fluid volume and injection flux can vary.

References

Abramowitz, M. & Stegun, I. A. (1964). *Handbook of Mathematical Functionsv with Formulas, Graphs, and Mathematical Tables*. Courier Corporation.

Adachi, J., Siebrits, E., Peirce, A., & Desroches, J. (2007). Computer simulation of hydraulic fractures. *International Journal of Rock Mechanics and Mining Sciences*, 44(5):739–757.

Alpern, J. S., Marone, C. J., Elsworth, D., Belmonte, A., & Connelly, P. (2012). Exploring the physicochemical processes that govern hydraulic fracture through laboratory experiments. In *46th US Rock Mechanics/Geomechanics Symposium*.

Antoniou, A., Bastawros, A., & Biner, B. (2007). Experimental observations of deformation behavior of bulk metallic glasses during wedge-like cylindrical indentation. *Journal of materials research*, 22(02):514–524.

Arroyo, M. & Trepat, X. (2017). Hydraulic fracturing in cells and tissues: fracking meets cell biology. *Current Opinion in Cell Biology*, 44:1–6.

Au, S. K. A., Soga, K., Jafari, M. R., Bolton, M. D., & Komiya, K. (2003). Factors affecting long-term efficiency of compensation grouting in clays. *Journal of Geotechnical and Geoenvironmental Engineering*, 129:254–262.

Barenblatt, G. I. (1962). The mathematical theory of equilibrium cracks in brittle fracture. *Advances in Applied Mechanics*, 7:55–129.

Batchelor, G. K. (1967). *An Introduction to Fluid Dynamics*. Cambridge University Press, Cambridge, UK.

Baumberger, T., Caroli, C., & Martina, D. (2006). Solvent control of crack dynamics in a reversible hydrogel. *Nature materials*, 5(7):552–555.

Bazant, Z. P., Salviato, M., Chau, V. T., Visnawathan, H., & Zubelewicz, A. (2014). Why fracking works. *Journal of Applied Mechanics*, 81(10):101010.

Boudou, T., Ohayon, J., Picart, C., & Tracqui, P. (2006). An extended relationship for the characterization of Young's modulus and Poisson's ratio of tunable polyacrylamide gels. *Biorheology*, 43(6):721–728.

Bunger, A. P. (2005). *Near-surface hydraulic fracture*. PhD thesis, University of Minnesota.

Bunger, A. P. (2006). A photometry method for measuring the opening of fluid-filled fractures. *Measurement Science and Technology*, 17(12):3237.

Bunger, A. P. & Detournay, E. (2007). Early-time solution for a radial hydraulic fracture. *Journal of Engineering Mechanics*, 133(5):534–540.

Bunger, A. P. & Detournay, E. (2008). Experimental validation of the tip asymptotics for a fluid-driven crack. *Journal of the Mechanics and Physics of Solids*, 56(11):3101–3115.

Bunger, A. P., Detournay, E., & Jeffrey, R. G. (2005). Crack tip behavior in near-surface fluid-driven fracture experiments. *Comptes Rendus Mécanique*, 333(4):299–304.

Bunger, A. P., Gordeliy, E., & Detournay, E. (2013). Comparison between laboratory experiments and coupled simulations of saucer-shaped hydraulic fractures in homogeneous brittle-elastic solids. *Journal of the Mechanics and Physics of Solids*, 61:1636–1654.

Bunger, A. P., Jeffrey, R. G., & Detournay, E. (2004). Toughness-dominated near-surface hydraulic fracture experiments. *Gulf Rocks, The 6th North America Rock Mechanics Symposium*.

Casares, L., Vincent, R., Zalvidea, D., Campillo, N., Navajas, D., Arroyo, M., & Trepat, X. (2015). Hydraulic fracture during epithelial stretching. *Nature Materials*, 14:343–351.

Chau, V. T., Bazant, Z. P., & Su, Y. (2016). Growth model for large branched three-dimensional hydraulic crack system in gas or oil shale. *Philosophical Transactions of the Royal Society A: Mathematical, Physical and Engineering Sciences*, 374(2078).

Christoffersen, P., Bougamont, M., Hubbard, A., Doyle, S. H., Grigsby, S., & Pettersson, R. (2018). Cascading lake drainage on the Greenland ice sheet triggered by tensile shock and fracture. *Nature Communications*, 9(1):1064.

Dalziel, S. B. (2006). Digiflow user guide. *DL Research Partners, Version*, 1.

De Maleprade, H., Clanet, C., & Quéré, D. (2016). Spreading of bubbles after contacting the lower side of an aerophilic slide immersed in water. *Physical Review Letters*, 117(9):1–5.

Denisin, A. K. & Pruitt, B. L. (2016). Tuning the range of polyacrylamide gel stiffness for mechanobiology applications. *ACS Applied Materials and Interfaces*, 8(34):21893–21902.

Detournay, E. (2016). Mechanics of hydraulic fractures. *Annual Review of Fluid Mechanics*, 48:311–339.

Detournay, E. & Garagash, D. I. (2003). The near-tip region of a fluid-driven fracture propagating in a permeable elastic solid. *Journal of Fluid Mechanics*, 494:1–32.

Dontsov, E. V. (2016). Tip region of a hydraulic fracture driven by a laminar-to-turbulent fluid flow. *Journal of Fluid Mechanics*, 797:R2.

Economides, M. J. & Nolte, K. G. (2000). *Reservoir stimulation*, volume 18. Wiley Chichester.

Gale, J. F., Laubach, S. E., Olson, J. E., Eichhubl, P., & Fall, A. (2014). Natural fractures in shale: A review and new observations. *AAPG Bulletin*, 98(11):2165–2216.

Gale, J. F., Reed, R. M., & Holder, J. (2007). Natural fractures in the Barnett Shale and their importance for hydraulic fracture treatments. *AAPG Bulletin*, 91:603–622.

Garagash, D., Detournay, E., & Adachi, J. (2011). Multiscale tip asymptotics in hydraulic fracture. *Journal of Fluid Mechanics*, 669:260–297.

Garagash, D. I. & Detournay, E. (2000). The tip region of a fluid-driven fracture in an elastic medium. *Journal of Applied Mechanics*, 67(1):183–192.

Garagash, D. I. & Detournay, E. (2005). Plane-strain propagation of a fluid-driven fracture: Small toughness solution. *Journal of Applied Mechanics*, 72(6):916–928.

Geertsma, J. & De Klerk, F. (1969). A rapid method of predicting width and extent of hydraulically induced fractures. *Journal of Petroleum Technology*, 21(12):1–571.

Goldman, T., Harpaz, R., Bouchbinder, E., & Fineberg, J. (2012). Intrinsic nonlinear scale governs oscillations in rapid fracture. *Physical Review Letters*, 108(10):104303.

Gordeliy, E. & Peirce, A. (2013). Coupling schemes for modeling hydraulic fracture propagation using the XFEM. *Computer Methods in Applied Mechanics and Engineering*, 253:305–322.

Griffith, A. A. (1921). The phenomena of rupture and flow in solids. *Philosophical Transactions of the Royal Society A: Mathematical, Physical and Engineering Sciences*, 221:163–198.

Haimson, B. & Fairhurst, C. (1969). In-situ stress determination at great depth by means of hydraulic fracturing. In *The 11th U.S. Symposium on Rock Mechanics*.

Harris, D. I., Mair, R. J., Burland, J. B., & Standing, J. (1999). Compensation grouting to control tilt of Big Ben Clock Tower. *Proceedings of the International Symposium on Geotechnical Aspects of Underground Construction in Soft Ground*, (1):225–232.

Hernández-Sánchez, J. F., Lubbers, L. A., Eddi, A., & Snoeijer, J. H. (2012). Symmetric and asymmetric coalescence of drops on a substrate. *Physical Review Letters*, 109(18):1–5.

Hertz, H. (1881). On the contact of elastic solids. *Journal für die reine und angewandte Mathematik*, 92:156–171.

Hubbert, M. K. & Willis, D. G. (1957). Mechanics of hydraulic fracturing. *Journal for Petroleum Technology*, 9(6):153–166.

Huppert, H. E. & Neufeld, J. A. (2014). The fluid mechanics of carbon dioxide sequestration. *Annual Review of Fluid Mechanics*, 46:255–272.

Irwin, G. (1957). Analysis of stresses and strains near the end of a crack traversing a plate. *Journal of Applied Mechanics*, 24:361–364.

Jeong, H.-Y., Li, X.-W., Yee, A. F., & Pan, J. (1994). Slip lines in front of a round notch tip in a pressure-sensitive material. *Mechanics of materials*, 19(1):29–38.

Johnson, A. W. & Harley, B. (2011). *Mechanobiology of cell-cell and cell-matrix interactions*. Springer Science & Business Media.

Kanninen, M. F. & Popelar, C. L. (1985). *Advanced Fracture Mechanics*. Oxford University Press, Oxford, UK.

Kavanagh, J. L., Boutelier, D., & Cruden, A. R. (2015). The mechanics of sill inception, propagation and growth: Experimental evidence for rapid reduction in magmatic overpressure. *Earth and Planetary Science Letters*, 421:117–128.

Kavanagh, J. L., Burns, A. J., Hilmi Hazim, S., Wood, E. P., Martin, S. A., Hignett, S., & Dennis, D. J. (2018). Challenging dyke ascent models using novel laboratory experiments: Implications for reinterpreting evidence of magma ascent and volcanism. *Journal of Volcanology and Geothermal Research*, 354:87–101.

Kavanagh, J. L., Menand, T., & Daniels, K. A. (2013). Gelatine as a crustal analogue: Determining elastic properties for modelling magmatic intrusions. *Tectonophysics*, 582:101–111.

Kavanagh, J. L., Menand, T., & Sparks, R. S. J. (2006). An experimental investigation of sill formation and propagation in layered elastic media. *Earth and Planetary Science Letters*, 245(3-4):799–813.

Khristianovic, S. A. & Zheltov, Y. P. (1955). Formation of vertical fractures by means of highly viscous liquid. *Proceeding of the 4th World Petroleum Congress*, 5:579–586.

Lai, C. Y., Zheng, Z., Dressaire, E., & Stone, H. A. (2016). Fluid-driven cracks in an elastic matrix in the toughness-dominated limit. *Philosophical Transactions of the Royal Society of London A: Mathematical, Physical and Engineering Sciences*, 374(2078).

Lai, C. Y., Zheng, Z., Dressaire, E., Wexler, J. S., & Stone, H. A. (2015). Experimental study on penny-shaped fluid-driven cracks in an elastic matrix. *Proceedings of the Royal Society A: Mathematical, Physical and Engineering Science*, 471(2182).

Lecampion, B. & Desroches, J. (2015). Simultaneous initiation and growth of multiple radial hydraulic fractures from a horizontal wellbore. *Journal of the Mechanics and Physics of Solids*, 82:235–258.

Lecampion, B., Desroches, J., Jeffrey, R. G., & Bunger, A. P. (2017). Experiments versus theory for the initiation and propagation of radial hydraulic fractures in low-permeability materials. *Journal of Geophysical Research: Solid Earth*, 122:1239–1263.

Legarth, B., Huenges, E., & Zimmermann, G. (2005). Hydraulic fracturing in a sedimentary geothermal reservoir: Results and implications. *International Journal of Rock Mechanics and Mining Sciences*, 42:1028–1041.

Lister, J. R. & Kerr, R. C. (1991). Fluid-mechanical models of crack propagation and their application to magma transport in dykes. *Journal of Geophysical Research: Solid Earth*, 96(B6):10049–10077.

Livne, A., Ben-David, O., & Fineberg, J. (2007). Oscillations in rapid fracture. *Physical review letters*, 98(12):124301.

Livne, A., Cohen, G., Ben-David, O., & Fineberg, J. (2004). Universal aspects of dynamic fracture in brittle materials. *Experimental Chaos*, 742:122–131.

Livne, A., Cohen, G., & Fineberg, J. (2005). Universality and hysteretic dynamics in rapid fracture. *Physical Review Letters*, 94(22):224301.

Lucantonio, A., Noselli, G., Trepat, X., Desimone, A., & Arroyo, M. (2015). Hydraulic fracture and toughening of a brittle layer bonded to a hydrogel. *Physical Review Letters*, 115:188105.

MacKay, J. L. & Kumar, S. (2013). Measuring the elastic properties of living cells with atomic force microscopy indentation. *Methods in Molecular Biology*, 931:313–329.

Mair, R., Bickle, M., Goodman, D., Koppelman, B., Roberts, J., Selley, R., Shipton, Z., Thomas, H., Walker, A., Woods, E., & Younger, P. (2012). Shale gas extraction in the UK : a review of hydraulic fracturing. *Royal Academy of Engineering*.

Mair, R. & Hight, D. (1994). Compensation grouting. *World Tunnelling and Subsurface Excavation*, 7(8).

Marshall, G. P., Coutts, L. H., & Williams, J. G. (1974). Temperature effects in the fracture of PMMA. *Journal of Materials Science*, 9:1409–1419.

Menand, T., Daniels, K. A., & Benghiat, P. (2010). Dyke propagation and sill formation in a compressive tectonic environment. *Journal of Geophysical Research: Solid Earth*, 115(B8).

Menand, T. & Tait, S. R. (2002). The propagation of a buoyant liquid-filled fissure from a source under constant pressure: An experimental approach. *Journal of Geophysical Research: Solid Earth*, 107(B11).

Mikelić, A., Wheeler, M. F., & Wick, T. (2015). A phase-field method for propagating fluid-filled fractures coupled to a surrounding porous medium. *Multiscale Modeling & Simulation*, 13:367–398.

Murphy, H. D., Tester, J. W., Grigsby, C. O., & Potter, R. M. (1981). Energy extraction from fractured geothermal reservoirs in low-permeability crystalline rock. *Journal of Geophysical Research: Solid Earth*, 86(B8):7145–7158.

Narayan, R. L., Tandaiya, P., Narasimhan, R., & Ramamurty, U. (2014). Wallner lines, crack velocity and mechanisms of crack nucleation and growth in a brittle bulk metallic glass. *Acta Materialia*, 80:407–420.

Nordgren, R. (1972). Propagation of a vertical hydraulic fracture. *Society of Petroleum Engineers Journal*, 12(4):306–314.

O'Keeffe, N. J. & Linden, P. F. (2017). Hydrogel as a medium for fluid-driven fracture study. *Experimental Mechanics*, 57(9):1483–1493.

O'Keeffe, N. J., Zheng, Z., Huppert, H. E., & Linden, P. F. (2018). Symmetric coalescence of two hydraulic fractures. *Proceedings of the National Academy of Sciences*, 115(41):10228–10232.

O'Keeffe, N. J., Huppert, H. E., & Linden, P. F. (2018). Experimental exploration of fluid-driven cracks in brittle hydrogels. *Journal of Fluid Mechanics*, 844:435–458.

Perkins, T. K. & Kern, L. R. (1961). Widths of hydraulic fractures. *Journal of Petroleum Technology*, 13(9):937–949.

Poliakov, A. N. B., Herrmann, H. J., Podladchikov, Y. Y., & Roux, S. (1994). Fractal plastic shear bands. *Fractals*, 2(4):567–581.

Reinhart-King, C. A., Dembo, M., & Hammer, D. A. (2003). Endothelial cell traction forces on RGD-derivatized polyacrylamide substrata. *Langmuir*, 19(5):1573–1579.

Rice, J. R. (1968). Mathematical analysis in the mechanics of fracture. *Fracture: an advanced treatise*, 2:191–311.

Ristenpart, W. D., McCalla, P. M., Roy, R. V., & Stone, H. A. (2006). Coalescence of spreading droplets on a wettable substrate. *Physical review letters*, 97(6):064501.

Rudnicki, J. W. (2000). Geomechanics. *International journal of solids and structures*, 37(1):349–358.

Rutqvist, J., Tsang, C. F., & Stephansson, O. (2000). Uncertainty in the maximum principal stress estimated from hydraulic fracturing measurements due to the presence of the induced fracture. *International Journal of Rock Mechanics and Mining Sciences*, 37:107–120.

Salimzadeh, S., Usui, T., Paluszny, A., & Zimmerman, R. W. (2017). Finite element simulations of interactions between multiple hydraulic fractures in a poroelastic rock. *International Journal of Rock Mechanics and Mining Sciences*, 99:9–20.

Sarkar, N. & Chaudhuri, B. B. (1994). An efficient differential box-counting approach to compute fractal dimension of image. *IEEE Transactions on systems, man, and cybernetics*, 24(1):115–120.

Savitski, A. A. & Detournay, E. (2002). Propagation of a penny-shaped fluid-driven fracture in an impermeable rock: asymptotic solutions. *International Journal of Solids and Structures*, 39(26):6311–6337.

Sharon, E., Cohen, G., & Fineberg, J. (2002). Crack front waves and the dynamics of a rapidly moving crack. *Physical Review Letters*, 88(8):85503.

Sneddon, I. N. (1946). The distribution of stress in the neighbourhood of a crack in an elastic solid. *Proceedings of the Royal Society of London A: Mathematical, Physical and Engineering Sciences*, 187(1009):229–260.

Sneddon, I. N. (1951). *Fourier Transforms*. McGraw-Hill.

Sneddon, I. N. & Lowengrub, M. (1969). Crack problems in the classical theory of elasticity,. *Wiley*.

Spence, D. A. & Sharp, P. (1985). Self-similar solutions for elastohydrodynamic cavity flow. *Proceedings of the Royal Society of London. A. Mathematical and Physical Sciences*, 400(1819):289–313.

Storm, C., Pastore, J. J., MacKintosh, F. C., Lubensky, T. C., & Janmey, P. A. (2005). Nonlinear elasticity in biological gels. *Nature*, 435(7039):191–194.

Takada, A. (1990). Experimental study on propagation of liquid-filled crack in gelatin: Shape and velocity in hydrostatic stress condition. *Journal of Geophysical Research: Solid Earth*, 95(B6):8471–8481.

Tanaka, Y., Fukao, K., & Miyamoto, Y. (2000). Fracture energy of gels. *The European Physical Journal E*, 3(4):395–401.

Tanaka, Y., Fukao, K., Miyamoto, Y., Nakazawa, H., & Sekimoto, K. (1996). Regular patterns on fracture surfaces of polymer gels. *Journal of the Physical Society of Japan*, 65(8):2349–2352.

Tsai, V. C. & Rice, J. R. (2010). A model for turbulent hydraulic fracture and application to crack propagation at glacier beds. *Journal of Geophysical Research: Earth Surface*, 115(F3):F03007.

Wallner, H. (1939). Linienstrukturen an bruchflächen. *Zeitschrift für Physik*, 114(5-6):368–378.

Westergaard, H. M. (1939). Bearing pressures and cracks. *Journal of Applied Mechanics*, 6:A49–A53.

White, M. l. (1960). The permeability of an acrylamide polymer gel. *The Journal of Physical Chemistry*, 764(5):1949–1951.

Willmore, T. J. (1949). The distribution of stress in the neighbourhood of a crack. *Quarterly Journal of Mechanics and Applied Mathematics*, 2:53–63.

Xi, X. K., Zhao, D. Q., Pan, M. X., Wang, W. H., Wu, Y., & Lewandowski, J. J. (2006). Periodic corrugation on dynamic fracture surface in brittle bulk metallic glass. *Applied physics letters*, 89(18):181911.

Xiao, Z. M., Lim, M. K., & Liew, K. M. (1994). Stress intensity factors for two coplanar penny-shaped cracks under uniaxial tension. *International Journal of Engineering Science*, 32:303–311.

Yokobori, T. Y. M., Ichikawa, M., & Ohashi, M. (1965). Interaction between elastic cracks, dislocation cracks and slip bands. In *ICF1, Japan*.

Zhang, J., Daubert, C. R., & Foegeding, E. A. (2005). Characterization of polyacrylamide gels as an elastic model for food gels. *Rheologica acta*, 44(6):622–630.

Zolfaghari, N., Meyer, C. R., & Bunger, A. P. (2017). Blade-shaped hydraulic fracture driven by a turbulent fluid in an impermeable rock. *Journal of Engineering Mechanics*, 143(11):04017130.

Appendix A

Supplementary experimental plots

A.1 Coalescence

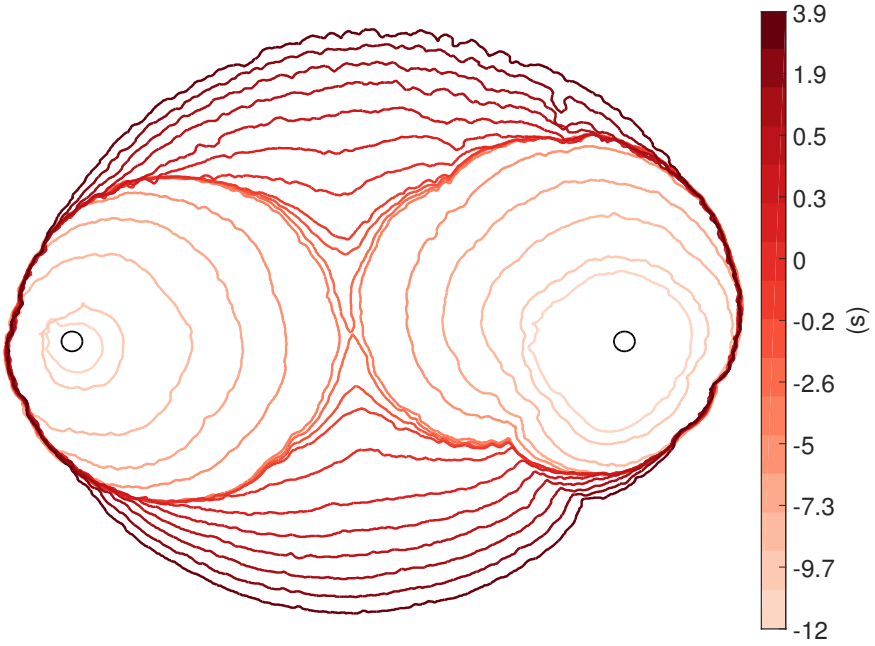

FIGURE A.1: Composite image of overlain fracture edges on the x-y plane (pivdb13). The colourbar corresponds to the time of each fracture edge.

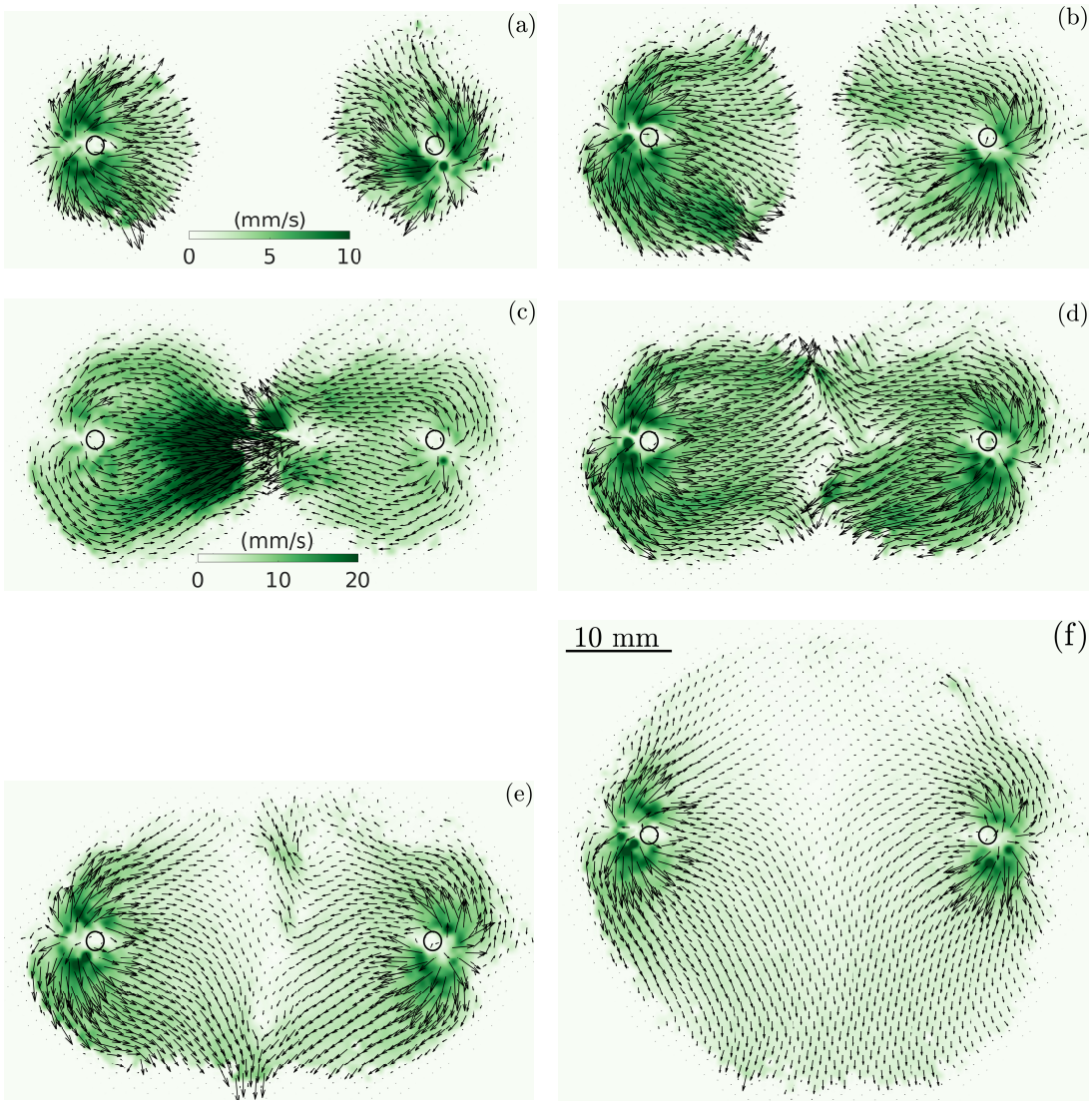

FIGURE A.2: PIV measurements for the time evolution of two coplanar fractures (pivdb15). The time for each image is (a) $t = -2.5$ s; (b) $t = -0.7$ s; (c) $t = 0$ s; (d) $t = 0.3$ s; (e) $t = 1.9$ s; and (f) $t = 7.1$ s. The colour bar represents velocity magnitude and values in (c) are twice that in the other images.

A.2 Partial coalescence

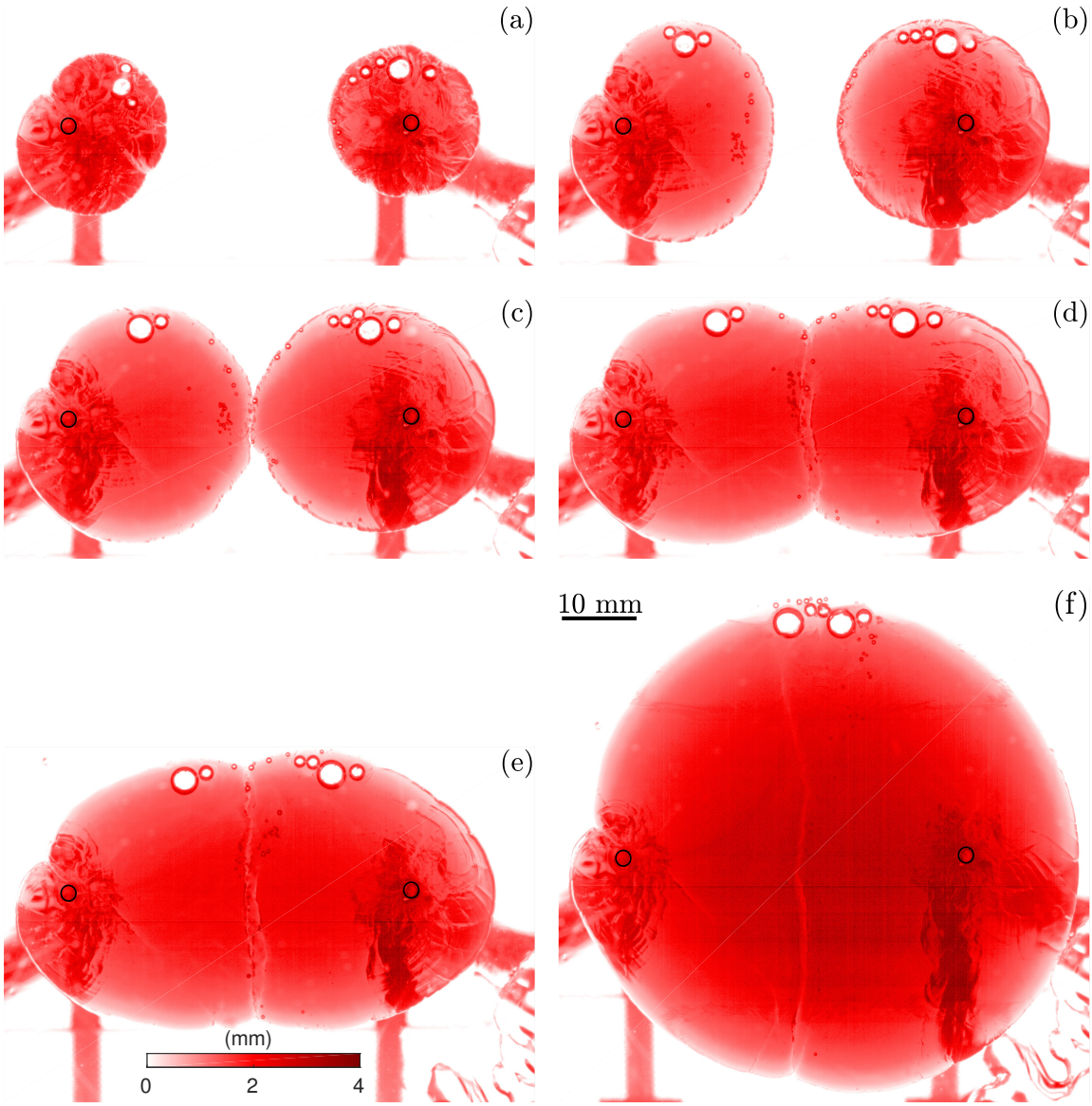

FIGURE A.3: Light attenuation measurements for the time evolution of two coplanar fractures (db24). The time for each image is (a) $t = 3.2$ s; (b) $t = 5.9$ s; (c) $t = 7.1$ s; (d) $t = 8.3$ s; (e) $t = 9.5$ s; and (f) $t = 17.5$ s. The fractures initially overlap in (c), but then partly coalesce in (d), with a small fluid interface between them forming near the top of the bridge.

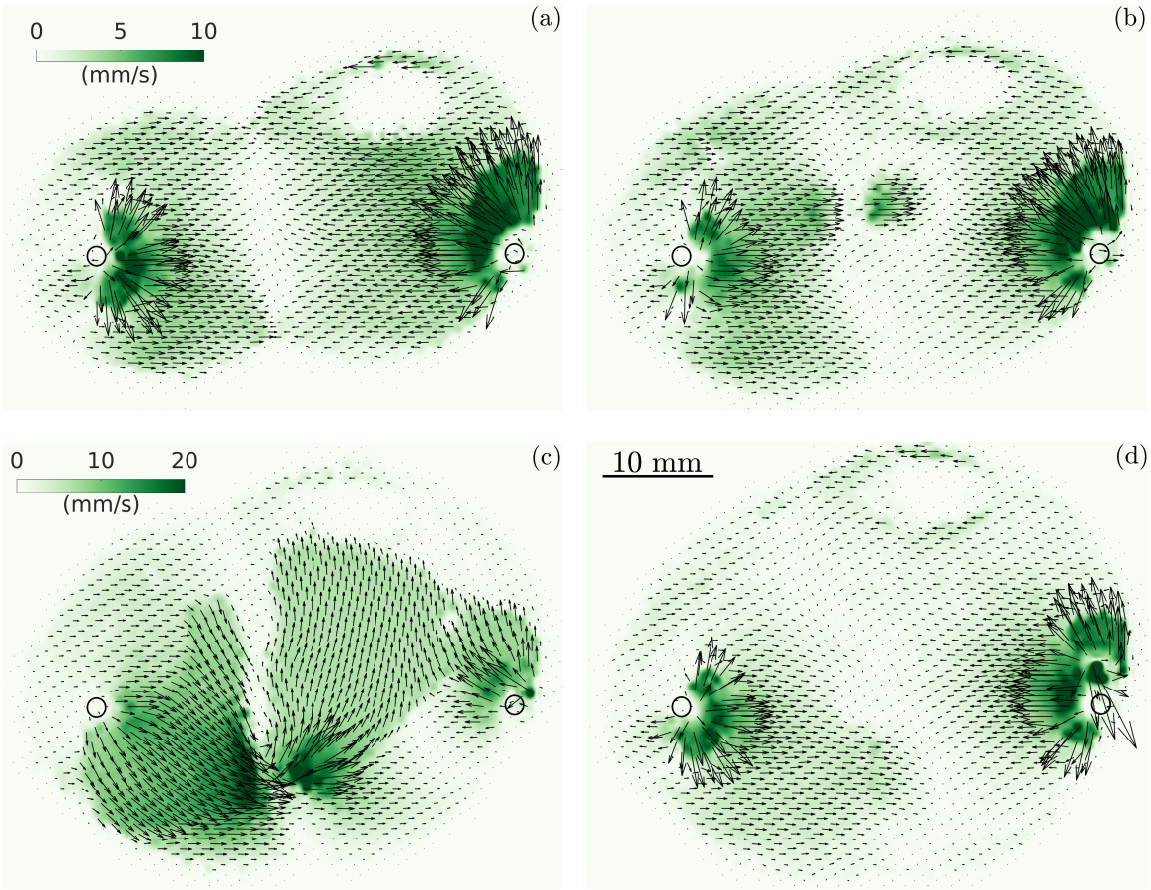

FIGURE A.4: PIV measurements for the partial coalescence of two coplanar fractures (pivdb11). The time for each image is (a) $t = 5.5$ s; (b) $t = 6.5$ s; (c) $t = 7.7$ s; and (d) $t = 8.5$ s. The colourbar represents velocity magnitude and values in (c) are twice that in the other images. The fractures initially overlap at $t = 4.7$ s, but then partly coalesce, with a fluid interface between them forming at specific points along the overlap in (b) and (c).